Design of an ultra-low-power communication system for leadless pacemaker synchronization

Mirko Maldari

INSTITUT POLYTECHNIQUE DE PARIS

NNT : 2020IPPAT018

Thèse de doctorat

Design of an ultra-low-power communication system for leadless pacemaker synchronization

Thèse de doctorat de l'Institut Polytechnique de Paris
préparée à Télécom Paris - C2S

École doctorale n°626 École doctorale Institut Polytechnique de Paris (ED IP Paris)
Spécialité de doctorat : Information, communications, électronique

Thèse présentée et soutenue à Palaiseau, le 29/05/2020, par

MIRKO MALDARI

Composition du Jury :

Sandro Carrara Professeur, EPFL (STI IMT ICLAB)	Président
Nöelle Lewis Professeur, Université de Bordeaux (IMS - Laboratoire de l'Intégration du Matériau au Système)	Rapporteur
Pierre-Yves Joubert Professeur, Université Paris Sud (C2N CNRS, Université Paris Saclay)	Rapporteur
Philippe Ritter Cardiologue, CHU de Bordeaux	Examinateur
Youcef Haddab Docteur-Ingénieur, Microport CRM (COE-ELEC)	Examinateur
Patricia Desgreys Professeur, Télécom Paris (C2S)	Directeur de thèse
Chadi Jabbour Maître de Conference, Télécom Paris (C2S)	Co-directeur de thèse

Ad Adele, Ewa e Nicola

Acknowledgements

Questo lavoro non é soltanto frutto di tre splendidi anni di ricerca, ma il risultato dell'apprendimento di una vita intera. Perciò, ringrazio, innanzitutto, la mia famiglia per avermi trasmesso la consapevolezza che non ci sono limiti irrangiungibili qualora il desiderio è accompagnato dalla giusta dose di determinazione e impegno.

Un remerciement spécial va à Lise (heureusement, il n'y a pas que les decouvertes scientifiques dans la vie !) pour avoir partagé les dernieres années avec moi.

Je tiens à rémercier tous les supeviseurs de mon projet de thèse: Chadi, Karima, Patricia, et Youcef. J'ai eu la chance d'être encadré par vous pour votre competences et qualitées humaines.

Merci à tous mes collegues chez Microport pour les bons moments passés ensemble. Une mention spéciale à Theoa, Stephane, Marc, Mous, Ashu, Giulia et Luca pour le support; à Delphine et Rafa pour avoir collaboré à la réussite du projet.

I thank all the people involved in the ITN program. This project, indeed, was far beyond my expectations, thanks to the incredible people I met in this journey.

Comment ne pas remercier Leslie, pour les magnifiques années de collocations. Tu as rendu extremement simple et agréable partager la vie de tous les jours (bon, à exception de quelques points de suture et de *France Inter* pour faire semblant d'écouter les infos le matin).

Finally, I would like to thank all my friends. The past moments spent with you make me retrace my life and the present moments make it valuable.

Titre : Conception d'un système de communication pour des pacemakers sans fils avec gestion de puissance

Mots clés : In-Body Communication, IBC, HBC, LCP, Leadless pacemakers, Ultra-low-power design

Résumé : L'objectif de nos études était de proposer des solutions optimisées pour la communication entre pacemakers sans sondes (LCP en Anglais) afin de permettre la synchronisation de la thérapie entre dispositifs implantés dans des chambres cardiaques différentes. L'Intra-Body Communication (IBC) est considérée comme une solution prometteuse. Il s'agit d'une communication qui utilise les tissue biologiques comme moyen de transmission. Les atténuations des canaux de communication ont été caractérisés en utilisant un model de thorax vérifié grâce à des essais in vivo. Un récepteur à très faible consommation a été conçu en technologie CMOS avec une sensibilité qui respecte les niveaux des signaux issus de la caractérisation du canal intra-cardiaque. Afin de minimiser la consommation du récepteur et, en conséquence, réduire l'impact du circuit en termes de longévité du dispositif, une stratégie innovante de communication a été proposée. Les résultats de recherche démontrent la faisabilité d'une synchronisation entre LCPs fondée sur la télémétrie, ouvrant la voie à la réalisation de systèmes multi-dispositifs pour améliorer la qualité du traitement de patients qui souffrent de bradycardie. Ce travail fait partie du projet WiBEC, un projet multidisciplinaire qui vise à concevoir des technologies sans fils pour des dispositifs implantables.

Title : Communication system design for leadless pacemaker synchronization with power management

Keywords : In-Body Communication, IBC, HBC, LCP, Leadless pacemakers, Ultra-low-power design

Abstract : Our research focused on power optimized solutions for the communication between Leadless Cardiac Pacemakers (LCP) to allow a synchronized therapy among devices implanted in different cardiac chambers. A promising solution is the Intra-Body Communication (IBC), which uses biological tissues as transmission medium. The attenuation of the communication channels were characterized using an accurate torso model that has been verified by means of in-vivo experiments. An ultra-low power receiver has been designed in CMOS technology according to the sensitivity requirement coming from the intra-cardiac channel characterization. Moreover, a novel communication strategy has been proposed to minimize the power consumption of the receiver reducing the impact in terms of device longevity. The research results show the feasibility of a telemetry driven synchronization of LCPs, paving the way toward multiple-leadless pacemaker systems that might improve the quality of treatment of the bradycardia patients. This work was part of the WiBEC project. It is a multi-disciplinary project aiming to develop the wireless technologies for novel implantable devices.

WiBEC - Wireless in-Body Environment

A Horizon 2020 Innovative Training Network

Description : WiBEC (Wireless In-Body Environment) is an Innovative Training Network for 16 young researchers, who will be recruited and trained in coordinated manner by Academia, Industry, and Medical Centres. WIBEC's main objective is to provide high quality and innovative doctoral training to develop the wireless technologies for novel implantable devices that will contribute to the improvement in quality and efficacy of healthcare. Two devices will be used as a focus for the individual researcher's projects; cardiovascular implants and ingestible capsules to investigate gastro intestinal problems. These devices will enable medical professionals to have timely clinical information at the point of care. The medical motivation is to increase survival rates and improvement of health outcomes with easy and fast diagnosis and treatment. The goal for homecare services is to improve quality of life and independence for patients by enabling ambient assisted living (AAL) at home. In this particular ETN, inter-sectorial and multi-discipline work is essential, as the topic requires cooperation between medical and engineering institutions and industry. Thus, the WIBEC consortim is composed of 3 Universities, 2 hospitals, and 3 companies located in different countries in Europe.

Institut Polytechnique de Paris
91120 Palaiseau, France

Résumé en français

Introduction

Chaque année, plus d'un million de stimulateurs cardiaques (pacemaker en anglais) sont implantés dans le monde afin de traiter les patients qui souffrent de bradycardie. Un pacemaker classique est constitué d'un boitier sous-cutané, qui intègre l'électronique du dispositif et des sondes qui permettent de rejoindre par voie trans-veineuse le cœur du patient. Les pacemakers peuvent utiliser jusqu'à trois sondes en fonction des besoins pour mieux traiter la pathologie du patient. Grâce aux avancées technologiques, notamment l'augmentation de la densité des batteries et la miniaturisation des circuits, il est possible d'intégrer toutes les fonctionnalités du pacemaker dans des petites capsules, en préservant une longévité du dispositif de plus de dix ans. Ce genre de dispositif, qui fusionne le boitier et la sonde du pacemaker classique est connu comme stimulateur cardiaque sans sonde, ou plus communément appelé en anglais leadless cardiac pacemaker (LCP). Le LCP est un dispositif implantable qui est fixé directement aux chambres cardiaques en utilisant un cathéter trans-veineux. D'un point de vu clinique, le LCP est plus attractif que les stimulateurs cardiaques classiques pour des raisons de sécurité, mais ses fonctionnalités sont encore limitées. Actuellement, le LCP peut stimuler seulement le ventricule droit, ce qui lui permet d'être seulement une alternative au pacemaker mono-chambre. Hélas, une thérapie de stimulation cardiaque mono-chambre intéresse une population très limitée de patients qui souffrent de bradycardies. Donc, il y a un grand potentiel curatif avec la création d'un système de stimulation multi-chambre sans sondes. Il s'agit d'un système multi-nodale de LCPs qui communiquent entre eux pour synchroniser la stimulation entre chaque nœud. Les types de communication classiquement utilisés pour les dispositifs implantables, tel que le RF et la communication inductive, sont des solutions sous-optimales en termes de taille et de consommation de puissance. Des études récentes, ont démontré la faisabilité d'une stimulation multi-nodale synchronisée grâce à la communication Intracorporelle. La communication Intracorporelle, ou

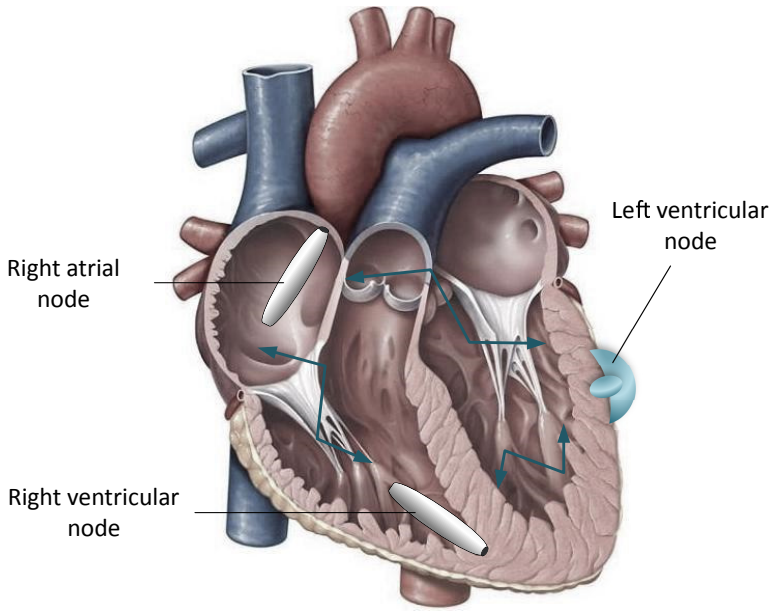

Système multi-noeuds de pacemakers sans sondes.

Intra Body Communication (IBC) en anglais, est une alternative prometteuse. Il s'agit d'une communication en champ proche basée sur la transmission Ohmique à travers les tissues biologiques. Notamment, un couple d'électrodes est utilisé pour émettre un champ électrique qui se propage à travers le corps humain afin d'être recueilli par un deuxième couple d'électrodes. Les avantages de la communication IBC sont : une très faible consommation de puissance vu qu'elle ne nécessite pas de radiation, qui est un phénomène à haute fréquence et basse efficacité au niveau de l'émetteur ; une réduction de la taille du dispositif grâce à l'élimination des antennes ou des selfs utilisées pour les communications RF classiques ; Une cyber-sécurité physique vu qu'elle nécessite un contact direct avec le corps du patient pour récupérer les informations. Les recherches antérieures à ce travail de thèse étaient des études préliminaires, qui négligeaient des aspects technologiques fondamentaux tels que la consommation d'énergie du module de télémétrie. L'objective de cette thèse était donc de poser les bases pour la synchronisation d'un système leadless multi-nodale, en optimisant la consommation de puissance du circuit de communication. La contribution scientifique de ce travail se diversifie en trois secteurs différents : la caractérisation des canaux IBC, la conception de circuit, et les protocoles de gestion du système de communication pour optimiser la consommation.

Caractérisation des canaux IBC

La propagation des signaux IBC dépends de plusieurs facteurs, qui rendent compliquée une généralisation analytique des niveaux d'atténuation. Donc, il était nécessaire d'estimer

Modèle CAO du torse complet (gauche) et coupe du modèle en passant par les ventricules (droite), où il est possible distinguer parmi les tissues du modèle : le tissue connectif, les muscles, les os, les cartilages, les poumons, le fois et le coeur

l'atténuation des canaux pour cette application, afin d'extraire la spécification en sensibilité du récepteur. Pour cela, nous avons développé un modèle de simulation numérique d'un torse humain, grâce auquel nous avons estimé l'atténuation de la tension des signaux IBC sur un large domaine fréquentiel [40kHz-20MHz]. Le modèle que nous avons développé se base sur un modèle humain validé par IT'IS Foundation Zurich : Duke de la population virtuelle (ViP2.0), qui représente un modèle d'homme de 34 ans récupéré par imagerie médicale (CT scan) avec une résolution égale à 0,5 mm. Le module NURBS de Simpleware Software Solution a été utilisé pour construire un modèle géométrique comprenant des organes, des muscles, des os, des tissus mous et des cartilages à partir d'informations spatiales de Duke. Le modèle géométrique a été importé dans COMSOL Multiphysics 5.3 où il a été amélioré pour ressembler avec précision aux caractéristiques physiologiques telles que la taille et le volume des chambres. Le modèle résultant distingue le sang et les tissus cardiaques car ils ont des propriétés électriques différentes. Nous avons focalisé nos études sur les canaux principaux pour le fonctionnement d'un système multi-nodale de pacemakers sans fils :

- Le canal intracardiaque, pour la communication entre les nœuds dans le ventricule droit (RV) et l'oreillette droite (RA) ;
- Le canal inter-ventriculaire, pour la communication entre le nœud du ventricule droit et la surface épicardique du ventricule gauche ;
- Le canal trans-thoracique, pour la communication des dispositifs implantables avec la surface de la peau du patient.

Les résultats de simulation montrent que le canal trans-thoracique subit les atténuations les plus faibles, grâce à la possibilité de placer de manière optimale les électrodes de surface. Les niveaux d'atténuation varient par rapport à la fréquence entre 37.4dB et 41.5

dB pour la capsule dans le RV, entre 45 et 50 dB pour une capsule dans le RA. Grace à cette étude nous avons identifié le meilleur placement des électrodes de surface pour minimiser les niveaux d'atténuation. Une première électrode doit être placé sur la ligne médio-claviculaire du cinquième espace intercostal, une deuxième électrode à l'extrémité médiane du quatrième espace intercostal. Le canal trans-thoracique est essentiel pour la programmation du dispositif et pour récupérer les données pendant le suivi du patient. Toutefois, les consultations de suivi sont des évènements rares comparés aux autres activités d'un tel système de dispositifs implantables ; donc, cette communication n'impacte pas le budget de consommation moyenne du stimulateur cardiaque.

Le canal inter-ventriculaire a été défini entre la capsule dans le RV et des sondes ponctuelles placées sur la surface du ventricule gauche (LV). Les meilleurs résultats sont obtenus pour les sondes à courte distance de la capsule RV. L'atténuation du canal inter-ventriculaire a des valeurs entre 45dB et 80dB selon la longueur du canal et la fréquence. Toutefois l'écart d'atténuation entre les sondes proches et les plus distantes diminue avec la fréquence. Cela est dû à l'augmentation de la conductivité des tissus biologiques avec l'augmentation de la fréquence. Les canaux les plus longs ont un bénéfice majeur à l'augmentation de la conductivité. Le canal inter-ventriculaire sert à mettre en communication un stimulateur intracardiaque dans le ventricule droit et un stimulateur épicardique placé sur la surface externe du ventricule gauche.

L'orientation des capsules joue un rôle important pour les atténuations des signaux IBC, les meilleurs résultats se manifestent avec une orientation parallèle. Cependant, le placement des stimulateurs cardiaques doit prioriser l'optimalisation de la thérapie, qui varie avec la population des patients. Pour cette raison, le canal intracardiaque a été estimé à la fois pour le meilleur et le pire cas. Le canal intracardiaque a des atténuations entre 72dB et 55dB, selon l'orientation et la fréquence. Le canal intracardiaque a des valeurs d'atténuations inférieures dans la plage des MHz grâce à la plus grande conductivité des tissus.

Pour vérifier les résultats de simulation nous avons mis en place un système de mesure flottant pour éviter des erreurs systémiques dû aux boucles de terre. Pour interfacer les instruments de mesure avec les tissus biologiques, nous avons utilisé des prototypes de capsules de pacemaker sans sondes. Notamment la capsule d'émission a été connectée à un générateur de tension sur batterie (DSO8060) et une capsule de réception a été connectée à un oscilloscope sur batterie (Fluke 190-110). Afin de détecter les signaux nous avons intégré un amplificateur de tension à l'intérieur de la capsule de réception. L'amplificateur a été prototypé avec des COTS afin d'obtenir un large produit gain-bande et un faible bruit. Le gain de l'amplificateur a été réglé à 36dB avec une bande passante entre 20kHz et 60MHz.

Afin de vérifier le système de mesure, nous avons fait des essais préliminaires in-vitro grâce à une technique de notre réalisation basée sur une solution saline de NaCl, où la concentration a été réglée pour suivre la conductivité des tissus cardiaques dans la plage fréquentielle d'intérêt. Les mesures in-vitro ont été reproduites sur COMSOL

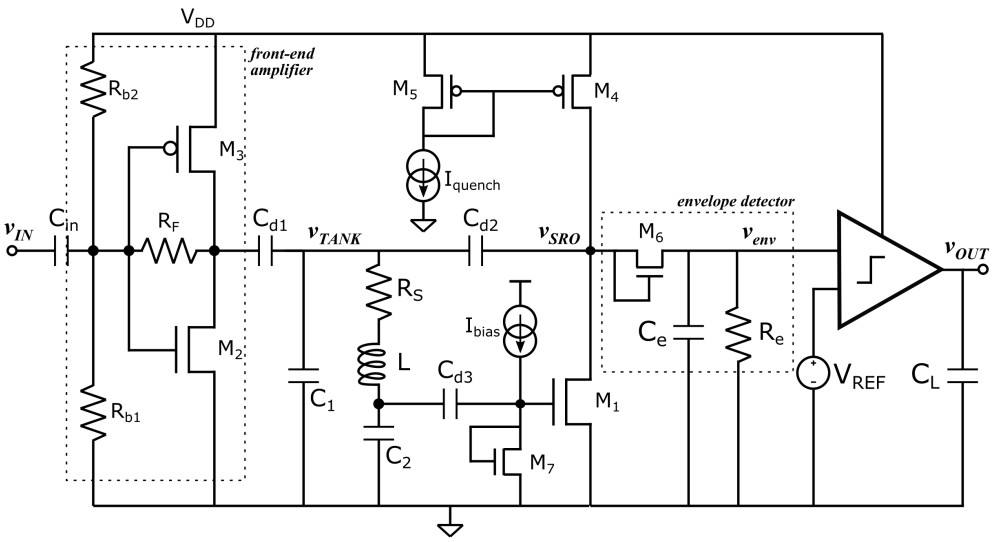

Schéma du récepteur IBC proposé en ce travail de thèse.

Multiphysics afin d'avoir une méthode de comparaison. Les résultats ont démontré une différence maximale entre simulation et mesures de 3dB qui est améliorée de 15 dB par rapport aux autres méthodologies de l'état de l'art. Cette étude a permis d'évaluer la fiabilité du système de mesure que nous avons prototypé. Les mesures in-vitro ne représentaient pas un modèle complexe comme le cœur. Dans un scénario de cas réel, les signaux peuvent bénéficier des effets de bord qui découleront de la forme du cœur et des différentes propriétés du tissu de contact de chaque paire d'électrodes.

Pour le canal inter-ventriculaire nous avons imprimé en 3D un prototype de capsule épicardique, où deux électrodes ont été placés à une distance de 1.4cm. La capsule épicardique a été utilisée comme émetteur pour la communication vers une capsule de réception dans le RV.

Les hôpitaux sont des environnements bruyants ; ainsi, les signaux acquis nécessitent d'être filtrés pour ne conserver que la fréquence du signal utile. MATLAB 2014 a été utilisé afin de concevoir des filtres très étroits autour de chaque fréquence d'intérêt.

Pour les essais in-vivo nous avons choisi le cochon vu que c'est l'animal qui a le cœur le plus proche anatomiquement de celui de l'être humain. Grâce aux mesures in-vivo, nous avons vérifié les niveaux d'atténuation dans une large bande fréquentielle [40kHz-20MHz] pour le pire et le meilleur cas d'orientation du canal intracardiaque et pour le canal interventriculaire.

Système de télemetrie

La caractérisation des niveaux d'atténuation était une étape essentielle pour la conception d'un système de communication optimisé vis à vis de la consommation. Nous avons

spécifié les contraintes du système de communication intracardiaque. Nous avons fait une analysé quantitative afin d'évaluer les spécifications d'un émetteur-récepteur pour la synchronisation des stimulateurs cardiaques sans sondes. La spécification la plus contraignante concerne les niveaux d'émission afin d'éviter des interférences avec les signaux physiologiques de l'activité neuronale. Selon l'ICNIRP, plus la fréquence est élevée, plus le risque de perturber la conduction du système nerveux est faible. Pour cela, nous avons choisi une fréquence porteuse dans le domaine des MHz. Cependant, la consommation de puissance des circuits intégrés augmente avec la fréquence. Étant donné que l'objectif principal est d'optimiser la consommation d'énergie de l'émetteur-récepteur, la complexité de la modulation doit être maintenue aussi faible que possible pour assouplir les exigences de performance de l'émetteur-récepteur. On-Off Keying (OOK) et Frequency-Shift Keying (FSK) sont des schémas de modulation viables pour la conception de récepteurs à très faible puissance. La modulation FSK, en général, nécessite plus de puissance côté récepteur par rapport aux signaux modulés OOK en raison de la nécessité d'une référence de fréquence interne pour démoduler les signaux entrants. Les récepteurs FSK ont généralement des débits binaires plus élevés que les récepteurs OOK. Cependant, la synchronisation LCP ne nécessite pas de communications à haut débit. Considérant que la contrainte de latence est respectée, le message d'événement cardiaque se réduit à une information binaire permettant au module de communication de travailler avec une démodulation mono bit. Ainsi, nous avons préféré la technique de modulation OOK à la FSK afin de réduire la complexité et la consommation de puissance du module de télémétrie.

Une étude de l'état de l'art des récepteurs OOK à très faible consommation a mis en évidence deux types d'architecture de récepteur : les récepteurs quasi-passifs et les récepteurs super-régénératifs (SRR). Les récepteurs quasi-passifs sont basés sur des techniques de redressement du signal communément utilisées pour le transfert d'énergie sans fil. Cette méthode est adaptée pour atteindre les valeurs de consommation d'énergie inférieure au micro Watt. D'ailleurs, Les récepteurs quasi-passifs ont généralement une faible sensibilité en raison de l'activation de la tension de seuil de diode, et nécessitent des technologies CMOS de petite taille pour minimiser les pertes. L'architecture Super-Régénérative est une approche élégante pour minimiser la consommation d'énergie tout en augmentant la sensibilité des récepteurs OOK. Ce type de récepteur nous convient car il peut obtenir des gains extrêmement élevés en minimisant les blocs à haute fréquence. En effet, il est possible d'obtenir une amplification RF extrêmement élevée et un filtrage à bande étroite avec une consommation de courant limitée grâce à l'architecture SRR. Le cœur du SRR est un oscillateur dont l'amplificateur a un gain dépendant du temps. Au-dessus d'une valeur de gain critique, l'oscillateur est capable de satisfaire le premier critère de Barkhausen, qui est nécessaire pour induire l'instabilité. Un signal de commande pilote l'évolution temporelle du gain pour contrebalancer périodiquement la dispersion de l'oscillateur. En conséquence, le système alterne des périodes instables, où il instaure des oscillations, et des périodes d'amortissement, où le signal de commande

éteint les oscillations. Le circuit de résonnance est couplé avec le signal d'entrée. Ainsi, la réponse de l'oscillateur varie en fonction de l'amplitude et de la fréquence du signal d'entrée. Le deuxième dispositif actif requis par le SRR est l'amplificateur de transconductance à faible bruit (LNTA) à l'avant du récepteur. Le LNTA a une double fonction : il injecte dans le réservoir de l'oscillateur une quantité de courant proportionnelle à l'amplitude du signal d'entrée, et il isole l'interface d'entrée des oscillations provenant du SRO en réduisant la fuite qui provoquerait des émissions involontaires.

Comparaison des performances du répcepteur avec l'état de l'art

Parameter	**Our work**	**Cho2016**
Technology	180 nm	65 nm
Supply voltage	1 V	0.8 V
Frequency	4 MHz	13.56 MHz
Latency	250 µs	10 µs
Modulation	OOK	OOK
Data rate	2 kbps	100 kbps
BER	$< 10^{-4}$	10^{-5}
60 dB-Interference Rejection	$f_0 \pm 200\ kHz$	$f_0 \pm 6\ MHz$
Sensitivity	10 µV	1 µV
Power consumption	18.25µW	42.5µW

Nous avons conçu un SRR en technologie CMOS 0.18µm. Les résultats de simulation montrent un design robuste envers le bruit, obtenant un BER inférieur à 0.01%, avec une sensibilité de -100dBv. Le principal atout de notre conception est la consommation d'énergie active, qui est inférieure à la moitié de la puissance d'un circuit équivalent de l'état de l'art (voir le tableau), qui présentait des performances de débit et de sensibilité supérieurs à notre carrier des charges. Il convient de souligner que la sensibilité maximale du récepteur est toujours inférieure d'un ordre de grandeur par rapport à l'amplitude d'entrée du cas le plus défavorable. Quantitativement parlant, le récepteur consomme environ 18 µW. La conception du récepteur a été adaptée pour la synchronisation de deux LCP. Cependant, la consommation de puissance du circuit ne permet pas à un dispositif tel que le LCP d'écouter en continu. Le récepteur consomme 18µW qui est un ordre de grandeur plus élevé que le budget de puissance du LCP. Donc, la phase finale de ce travail de thèse a visé à optimiser le temps d'écoute du récepteur pour réduire son impact sur la longévité du dispositif.

Stratègie de communication

La capsule implantée dans le RV nécessite les informations de synchronisation de l'activité auriculaire (onde P) pour synchroniser artificiellement l'activité ventriculaire. Le protocole de communication est piloté par la capsule RA, qui envoie une impulsion de syn-

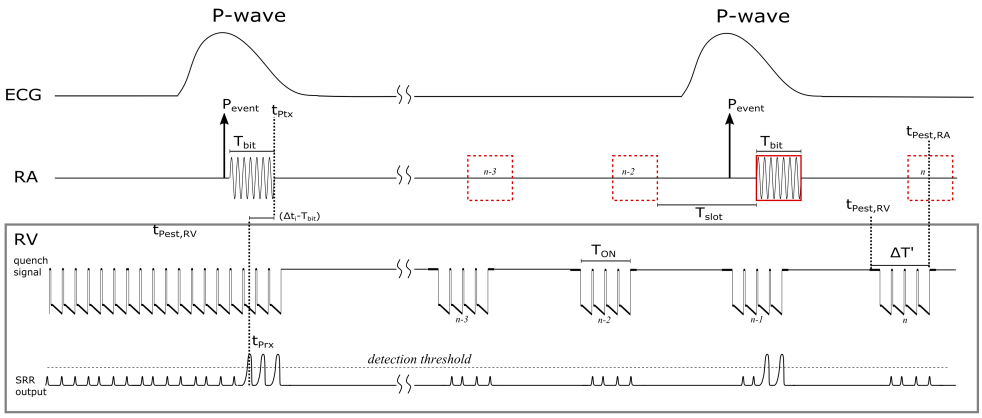

Représentation graphique de la stratégie de communication pour la synchronisation atrio-ventriculaire de pacemakers sans sondes.

chronisation au RV dès que la détection de l'onde P se produit (Pevent). Pour réduire la consommation électrique moyenne du module de communication, nous proposons une fenêtre d'écoute adaptative qui exploite la propriété de périodicité des événements P-wave. En effet, la fréquence cardiaque physiologique n'accélère pas de plus de [25-35]% d'un battement à l'autre. Pour réduire encore la consommation d'énergie, on peut dégrader la latence de la transmission d'informations jusqu'à 10 ms ce qui est du même ordre de résolution de l'échocardiographie. Nous proposons de découper la période physiologique où l'onde P peut se produire en sous-blocs périodiques où la communication peut être activée. Le nombre de créneaux n est donné comme le premier nombre entier provenant du rapport entre la fenêtre temporelle physiologique de l'onde P et une seule période de sous-bloc. Par exemple, si l'on considère avoir une fréquence cardiaque de 60 bpm, la période physiologique totale est égale à 250 ms. Ensuite, régler Tsleep = 9 ms et TON = 1 ms, conduit à n = 25, réduisant le temps d'écoute global à 25 ms. Lorsque la capsule RA détecte l'onde P, elle utilise le premier emplacement d'émission possible de la fenêtre TX pour envoyer l'impulsion de synchronisation vers la capsule RV. Pour assurer une transmission correcte de l'impulsion de synchronisation, les capsules doivent avoir la même référence de temps, en alignant les périodes d'émission et de réception. La première impulsion de synchronisation est utilisée pour initialiser la stratégie de communication. Après l'initialisation, les impulsions de synchronisation sont utilisées pour coupler la capsule RV à l'activité auriculaire. Pendant le premier cycle cardiaque, la capsule RV n'a aucune idée de si et quand l'impulsion de synchronisation peut se produire. Ainsi, le récepteur est actif tout le temps de manière continue. Dès que la capsule RV détecte la première impulsion de synchronisation, elle stocke la valeur de son temporisateur de référence. En considérant une impulsion de synchronisation d'une durée Tbit = 500 µs, la fenêtre RX nécessite des sous-blocs avec TON = 750 µs pour s'assurer que l'impulsion de synchronisation couvre totalement au moins un cycle d'extinction du

SRR.

Nous avons proposé un algorithme piloté par la détection de l'activité atriale (onde P de l'ECG) qui peut réduire drastiquement la consommation du récepteur. Selon des études cliniques, l'onde P physiologique a une accélération maximale du 25% entre chaque battement. L'algorithme estime l'intervalle entre deux ondes P afin de définir des sous-blocs de communication dans la période physiologique où l'onde-P se manifeste. Nous avons proposé une stratégie de communication qui permet de réduire le temps d'écoute au 2%. Cela nous permet d'avoir un récepteur capable de synchroniser deux capsules à chaque battement en consommant seulement 340nW en moyenne. Cette puissance additionnelle peut être compensé sur 10 ans en augmentant la batterie du dispositif de seulement 30mAh.

Conclusions

Ce travail a conduit à la première solution optimisée en puissance pour la synchronisation LCP basée sur la communication.

Ce travail regroupe des études très différentes qui ont été essentielles pour la conception d'un système IBC pour des applications de stimulateurs sans fil : caractérisation des canaux, circuit ultra basse puissance, stratégie de synchronisation. Par la suite, nous identifions les futurs travaux à effectuer pour finaliser et optimiser nos propositions de solutions. La caractérisation des canaux a été adaptée sur un prototype de capsule d'une longueur de 33 mm et d'un diamètre de 6,4 mm. D'autres simulations devraient être effectuées pour quantifier l'effet de la longueur de la capsule en termes d'atténuation du canal. Une telle étude peut conduire à un dimensionnement LCP optimal comme compromis entre faibles pertes de communication et contraintes mécaniques. Dans cette étude, pour transmettre les signaux IBC, nous avons utilisé les mêmes électrodes que celles conçues pour l'administration de la thérapie, afin de réduire la complexité de la conception LCP. Cependant, il est possible qu'une atténuation légèrement plus basse puisse être atteinte en optimisant la taille des électrodes. De plus, avec des électrodes plus grosses viennent des densités de courant plus faibles, relâchant la contrainte de la tension d'émission. Cette considération est essentielle chaque fois que les émetteurs-récepteurs IBC doivent fonctionner avec des fréquences porteuses limitées car les consignes de sécurité sont plus strictes aux basses fréquences. En outre, d'autres expériences in vivo devraient être réalisées pour mieux caractériser le bruit de l'environnement et les interférences, conduisant à une prédiction plus précise du BER. Par ailleurs, la même approche de caractérisation des canaux peut être adoptée pour d'autres applications implantables adaptant le modèle au dimensionnement et au positionnement particuliers des transducteurs. Dans ce travail, un récepteur ultra basse puissance respectant toutes les spécifications de notre étude de cas a été présenté. Les variations liées au processus doivent être neutralisées, en concevant un système de calibration pour le récepteur. Des simulations post-implantation doivent être effectuées pour valider les résultats avant

l'intégration du circuit. Ensuite, le circuit doit être testé à l'aide de signaux externes pour valider nos résultats. Ces tests préliminaires ont pour but de valider les performances du récepteur super-régénératif en fonction du signal d'amortissement proposé. Une fois qu'une opération correcte de l'architecture suggérée sera vérifiée, une version complète de l'émetteur-récepteur doit être conçue. En particulier, un générateur de courant stable est nécessaire pour générer le signal d'amortissement de l'oscillateur et un circuit d'émission à haut rendement doit être conçu. La stratégie suggérée dans ce travail peut réduire considérablement la consommation d'énergie pour la synchronisation des systèmes multi-nodales de stimulateurs sans sondes. Les systèmes LCP multi-nœuds ont été choisis comme principale plateforme applicative de nos études. Cependant, la stratégie de synchronisation pourrait être adoptée par n'importe quel couple de dispositifs, y compris le LCP implanté dans le RV et un autre dispositif capable de détecter l'onde P comme les dispositifs sous-cutanés (c'est-à-dire les enregistreurs de boucle, sous-cutané-ICD). Pour valider la stratégie, je propose de synthétiser le matériel et les signaux de contrôle de la technique proposée dans un FPGA. Ensuite, des expériences in vivo doivent être effectuées pour évaluer à quel point le système est proche d'une parfaite synchronisation auriculo-ventriculaire.

Ce travail a démontré la faisabilité d'une synchronisation basée sur la communication pour le stimulateur cardiaque sans fil (LCP) via la communication galvanique intracorporelle (IBC). Le système a été analysé à partir de la caractérisation des canaux amenant à la'établissement des spécifications de l'émetteur-récepteur. Ces spécifications ont été utilisées pour concevoir un récepteur ultra-faible puissance en technologie CMOS 0,18 µm pour analyser le bilan de puissance requis par ce type de solutions. Le bilan de puissance du récepteur a été nettement amélioré grâce à une stratégie de communication adaptable conduisant à un protocole de synchronisation économe en énergie. Les résultats de ces travaux ont abouti à la soumission de trois brevets à l'institut français des brevets :

- M.Maldari. Système médical implantable pour mesurer un paramètre physiologique, PA122168FR, 2019.
- M.Maldari. Système pour réaliser une mesure d'impédance cardiographie, PA126089FR, 2019.
- M.Maldari. Procédé et système de communication entre plusieurs dispositifs médicaux implantables, PA127465FR, 2020.

En ce qui concerne la diffusion de ces travaux, un article de conférence internationale et un article de revue ont été publiés à ce jour :

- M. Maldari, K. Amara, I. Rattalino, C. Jabbour, and P. Desgreys. *Human Body Communication channel characterization for leadless cardiac pacemakers*, 25th IEEE International Conference on Electronic Circuits (ICECS), 2018.

- M. Maldari, M. Albatat, J. Bergsland, Y. Haddab, C. Jabbour, and P. Desgreys. *Wide frequency characterization of intra-body communication for leadless pacemakers*, IEEE Transaction on Biomedical Engineering, 2020.

Un autre article de revue est en cours de soumission suite à la selection de ce travail par *URSI-France* parmi les meilleurs quatres thèses en Radio-science du 2021. De plus, deux œuvres sans actes ont été présentées :

- M. Maldari. *Human Body Communication for leadless pacemaker applications*, International Micro-electronics Assembly and Packaging Society (iMAPS) Lyon, 2017.

- Mirko Maldari, Karima Amara, Chadi Jabbour, Patricia Desgreys. *Human Body Communication channel modeling for leadless cardiac pacemaker applications*, GDR SOC2 Paris, 2018.

Contents

List of Figures

List of Tables

Nomenclature

ADC Analog Digital Converter, page 54

AV atrioventricular, page 8

AVB Atrioventricular Block, page 12

AVS Atrioventricular Synchronization, page 17

AWGN Additive White Gaussian Noise, page 65

BER Bit Error Rate, page 64

BS Body Surface, page 31

CEM Computational Electromagnetic Modeling, page 21

CHF Congestive Heart Failure, page 18

CMOS Complementary Metal-Oxide Semiconductor, page 61

CMRR Common Mode Rejection Ratio, page 48

CRM Cardiac Rhythm Management, page 14

CRT Cardiac Resynchronization Therapy, page 16

ECG electrocardiogram, page 11

EGM Electrogram, page 111

FEM Finite Element Method, page 25

FIR Finite Impulse Response, page 48

FPGA Field Programmable Gate Array, page 126

FSK Frequency-Shift Keying, page 63

FSM Finite State Machine, page 121

HF high-frequency, page 62

IBC Intra Body Communication, page 20

ICD Implantable Cardioverter Defibrillator, page 15

ICNIRP International Commission on Non-Ionizing Radiation Protection, page 62

INPI Institut National de la Propriété Industrielle, page 127

ITN Innovatie training network, page 3

LCP Leadless Cardiac Pacemaker, page 16

LNA Low Noise Amplifier, page 67

LNTA Low Noise Transconductance Amplifier, page 68

LV Left Ventricle, page 18

LV Left Ventricle, page 53

MSB Most Significant Bit, page 119

OOK On-Off Keying, page 63

PAC Premature Atrial Contraction, page 12

PVC Premature Ventricular Contraction, page 12

RA Right Atrium, page 29

RAA Right Atrial Appendage, page 7

RV Right Ventricle, page 29

SA sinoatrial, page 8

SAR Specific Absorption Rate, page 62

SRR Super Regenerative Receiver, page 67

1 Introduction

A Statistical study revealed that more than 2% of the adult population suffer from Cardiac arrhythmias [4]. Cardiac arrhythmias are heart rhythm abnormalities caused by malfunctions of the conductive system of the heart such as premature contractions, bradycardia, supraventricular tachycardia, and ventricular tachycardia.
Bradycardia is a slow and/or irregular rhythm that is not sufficient to pump enough oxygenated blood to the rest of the body. Bradyarrhythmia can manifest as atrial activity arrest, inability to increase heartbeat rate during exercise (chronotropic incompetence) or atrioventricular conduction blocks.
Cardiac Pacemakers are used to treat bradycardia patients, whenever the symptoms persist to drug administration. Pacemaker devices must sense spontaneous heartbeat and pace by electric stimulation whenever the heartbeat rate is considered too slow.
Conventional pacemakers consist of a subcutaneous control unit and intravenously implanted intra-cardiac leads.
The leads are the weakest links in present systems since they can dislodge, cause infection, thrombosis [5], endo-carditis [6], mechanical damage, and pneumothorax. [7, 8]. The yearly rate of lead-related complications is approximately 1.6% [9]. With more than four million implanted CRMDs worldwide, around 65 000 lead-related complications occur every year. Malfunctioning or infected leads often require extraction, which is not a simple procedure, requiring surgery and transesophageal echocardiographic monitoring.
Improved electronics and smaller batteries have made leadless pacemakers possible. Leadless Cardiac Pacemakers (LCP) are self-contained devices consisting of sensors, a current injector, a telemetry module, and an integrated battery unit [10]. They are designed to be implanted inside the right ventricle through a transvenous catheter [11].
From a clinical point of view, current LCPs may be superior from a safety perspective, but their functionality is limited. At present, they only pace the right ventricle (VVI pacing) and can only be used as an alternative for ventricular single-chamber pacemakers which are only used for a fraction of the pacemaker patients.
Single chamber pacemakers are rarely used since they do not maintain AV synchronicity,

leading to increased risk of stroke and heart failure, which is substantially reduced with dual-chamber pacemakers or cardiac resynchronization therapy (CRT) [12].
There is, therefore, a large potential for further innovation to create devices that provide multi-chamber leadless pacing [13]. A multi-nodal LCP system requires a communication network between all the nodes implanted in multiple chambers.

Standard wireless communication approaches for implants, such as radiofrequency and inductive coupling are suboptimal solutions because they require: 1) dedicated components (antennas and coils), increasing the size of the implant; 2) high power consumption, reducing battery lifetime, which is a critical issue in permanent implants.
A promising alternative solution is galvanic Intra-Body Communication (IBC), which is a near field communication method based on Ohmic transmission through body tissues. In IBC, an electrode pair is used to build up an electric field that propagates through the human body reaching a second electrode pair used to receive the signal [14].
The advantages of IBC are: 1) ultra-low power requirement; 2) no additional antenna is required since the pacing electrodes may be used to generate the electric field for the communication; 3) minimal risk of eavesdropping since direct contact with the body is strictly required to form a channel [15].

Since the introduction of IBC communication by Zimmerman in 1996 [16], several studies have considered the human body as a communication channel. Most of those studies are focused on body-surface communications [17, 18, 19], leading IEEE to include it as a physical layer in IEEE802.15.6 standard for Wireless Body Area Networks (WBAN) under the name of Human Body Communication (HBC).
A Recent study characterized galvanic IBC for intra-cardiac communication in the frequency range of 1 kHz to 1 MHz [20], where in vivo and ex vivo measurements were performed using electrodes injected through the heart wall that is not a real representation of actual LCP systems. Moreover, the measurement system was not completely isolated from the ground, limiting the reliability of the attenuation values of the channel according to measurement setup studies performed in [21]. Inter-electrode and channel length distances were limited to 15 mm and 60 mm. Surprisingly, there was no significant difference among measurements with channel lengths bigger than 50 mm [22], likely due to ground coupling issues. The same authors showed the advantage of frequencies higher than 1 MHz in further work [23] pointing out the need for a broader characterization of the intra-cardiac channel. Therefore, to build efficient IBC transceivers for LCP applications, a more accurate and broader characterization of communication channels is needed.
The firsts attempts of multi-node pacing using physically separate devices proved the clinical feasibility of both dual chamber and CRT-P leadless pacing [22, 20]. The authors suggested a telemetry-based synchronization of LCPs, using the IBC. However, this solution was verified using off-the-shelf components, without assessing the power

optimization of the circuitry.

This doctoral thesis was carried out as a part of the WiBEC (Wireless in-Body Environment Communication) project, which was an Innovative Training Network (ITN) funded by the European Commission. The WIBEC project aimed to develop wireless technologies for novel implantable devices, contributing to the improvement in quality and efficacy of healthcare [24].

1.1 Objectives of this work

The objective of this doctoral thesis is to lay the foundations for the synchronization of multi-node LCP systems, assessing the power optimization of the communication circuitry. Indeed, this work consists of a system study to find out a power-optimized solution for the communication module.
In particular, the Intra-Body Communication was chosen as preferred kind of telemetry for three main reasons: size optimization (i.e. no antenna or any other additional transducer is required), emitted power efficiency (i.e. no radiation), and data security (i.e. contact with the patient is strictly required).
The scientific contribution of this work relies on three different field: IBC channel characterization, ultra-low-power circuit design, and protocols for power-efficient atrioventricular synchronization.

1.2 Manuscript outline

The manuscript is organized as follow:

- chapter 2 gives some background knowledge about the context of this work, pointing out its clinical relevance;
- chapter 3 reports the preliminary studies we performed about the channel characterization for LCP applications, consisting of numerical simulations, measurement system prototyping, and in vivo verification;
- chapter 4 points out the transceiver requirement based on the estimated loss of the preliminary studies and describe the process that led us to design an ultra-low-power receiver for LCP synchronization purposes;
- chapter 5 deals with a communication strategy to further reduce the power consumption of the receiver;
- finally, in chapter 6, we summarize the key findings of this research and conclude pointing out the future work leading to the LCP prototype for a multi-node pacing system.

2

Context of the work

This chapter aims to give a background to understand the clinical relevance of the objectives of this work.
The Leadless pacemaker is an implant device intended to be fixed at the endocardium of bradycardia patients. Thus, the environment of the object of study is the heart and, more generally, the rib cage, whose anatomy is roughly described in the first section of this chapter.
A clinical background about the normal electrophysiology of the heart is given in section 2.2, followed by the pathological conditions caused by the dysfunction of the heart conduction system.
Further, we introduce Cardiac Rhythm Management (CRM) devices, used to counteract drug resistant pathologies. In section 2.3, the LCP is introduced, explaining its clinical advantages over conventional pacemakers and its current limits. Contrarily to conventional pacemakers, LCPs can only pace a single location in the heart, arising the necessity of multi-node LCP systems, that are described in subsection 2.3.2. Multi-node LCP systems require reliable solutions to synchronize every single device.
The Intra-Body Communication (IBC) is a convenient technology, described in section 2.4, which seems tailored to LCP applications.

2.1 Anatomy

This section aims to describe the environment of the communication. The anatomy description of the rib cage and the heart are based on a worldwide known atlas of anatomy, ideated and illustrated by *F.H.Netter* [25].

2.1.1 The rib cage

The thorax is the superior part of the trunk, whose shape resembles a cylinder or a truncated cone. The thoracic cavity is separated from the abdominal cavity by the

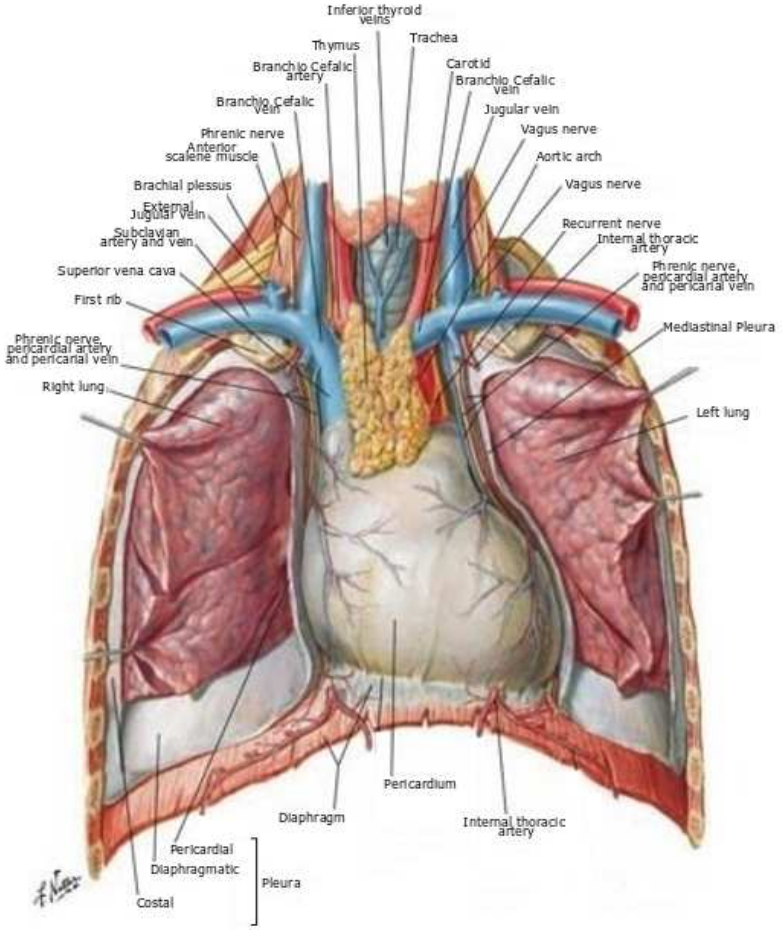

Figure 2.1: Anatomy of the thoracic cage

diaphragm, which has a dome shape and is constituted by tendons with peripheral muscles. At the top, the thorax ends with an opened structure that includes the sternum, the first ribs, and the first thoracic vertebra. The back of the thorax is delimited by twelve thoracic vertebrae and by the posterior part of the ribs. The front is delimited by the sternum, the costal cartilages, and the anterior part of the ribs. Sideways, it is delimited by the ribs, where intercostal muscles close the space between adjacent ribs. The sternum is at the midline in a superficial location. The sternum articulates with the clavicles and the first seven pairs of ribs. The ribs make the great part of the thoracic skeleton. There are twelve ribs for each side of the trunk. The ribs are thin and elastic bones whose posterior part articulates with thoracic vertebrae, whereas the anterior part terminates with the costal cartilages. The first seven pairs join with the sternum through their cartilages, whereas the 8^{th}, the 9^{th} and the 10^{th} pairs join with themselves. The 11^{th} and the 12^{th} pairs are smaller and terminate with the cartilages

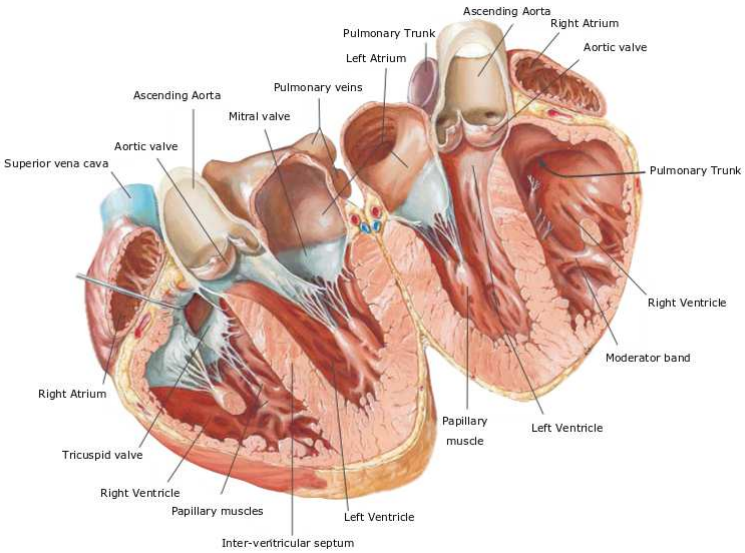

Figure 2.2: Anatomy of heart chambers

free end. Several muscles of the neck originate at the top of the rib cage, where we can also find blood vessels such as the external jugular vein. At the bottom of the neck, we can find the pharynx, the esophagus, the trachea, the thyroid gland, and muscles. Here, covered by connective tissue, there is the common carotid artery, the internal jugular vein, and the vagus nerve. The lungs, covered by the pleura, occupy most of the thoracic cavity. The trachea descends from the neck and splits in the main bronchi. The right lung is slightly bigger than the left lung to leave space to the heart. The heart and parts of the great vessels are contained by the pericardial cavity that has a conic form whose base is at the right posterior part, whereas the apex is at the left anterior part.

2.1.2 The Heart

Inside the pericardial cavity, we find the heart that is a hollow organ divided into four chambers. The heart is hung to the great vessels from the base. The chambers are functionally linked per pair. The cardiac septum separates each pair, which consists of one atrium and one ventricle. The right chambers are separated thorough the coronary sulcus, where the right coronary artery lies. The ventricles are separated by the inter-ventricular sulcus, where we can find the interventricular branch of the left coronary artery. At the top, the pulmonary trunk originates from the right ventricle. The vena cava pass through the right atrium from side to side. The part of the vena cava on the top of the right atrium is called superior vena cava, whereas the part on the bottom is called inferior vena cava. The superior vena cava is separated from the right atrium

appendage through the terminal sulcus. The right pulmonary veins join the right part of the left atrium, whereas the left pulmonary veins join the left atrium from the left. The branches of the pulmonary trunk lie on the surface of the left atrium. Hither, they join both the left and the right lungs. In the coronary sulcus between the left atrium and the left ventricle, we can find the coronary sinus. Here, the cardiac veins converge, collecting the blood from the heart muscle.

2.1.2.1 The right atrium

The right atrium can be divided into a smooth posterior wall where it joins with the venae cavae, and a trabecular wall, which represents the embryonal right atrium. Those two parts are separated by the crista terminalis, which internally corresponds to the terminal sulcus. Several pectinate muscles originate from the terminal sulcus covering the free wall of the right atrium. Between the pectinate muscles, the wall of the atrium is very thin. At the superior part of the right ventricle, we find the right atrial appendage (RAA), which is a triangular purse filled with pectinate muscles. For its shape and location, the RAA is utilized as an easy access for surgical interventions. At the posteromedial part of the right atrium, we find the interatrial septum, where we find the fossa ovalis, which is a slight depression that can be used to pass a lead in the left atrium. In the middle of the frontal part, we can find the tricuspid valve, which gives access to the right ventricle.

2.1.2.2 The right ventricle

The right ventricle chamber can be divided into an influx part, where we find the tricuspid valve and an efflux part where we find the pulmonary trunk. The efflux part is considerably smoother compared to the influx part, which is covered by trabeculae. Papillar muscles join the cuspids of the tricuspid valve through the chordae tendineae. The pulmonary trunk originates from the top of the right ventricle; further, it splits in the pulmonary arteries.

2.1.2.3 The left atrium

The left atrium is characterized by a smooth wall, which is thicker than the right atrium wall. From both sides, the left atrium gives access to the heart for the blood coming from the pulmonary veins. At the anterior part, we find the left atrium appendage that contains small pectinate muscles.

2.1.2.4 The left ventricle

The left ventricle has an elliptic shape with a truncated superior part. Here, we find the mitral valve and the aortic valve. The left ventricle valves are close to each other and are separated only by a fibrous septum. The average thickness of the left ventricle

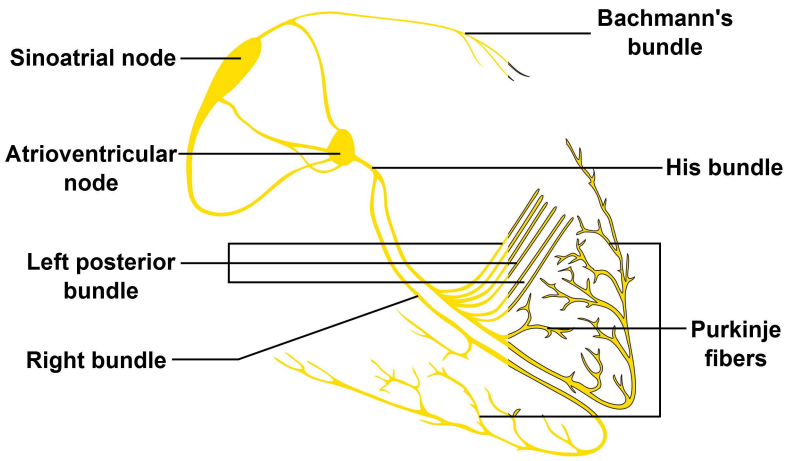

Figure 2.3: Electric conduction system of the heart.

wall is usually three times bigger than the right ventricle one. In the left ventricle, we can find trabeculae carnae, especially toward the apex of the heart. A small part of the interventricular septum, placed under the cuspids of the aortic valve, is made of a thin membrane. The rest of the interventricular septum is made of muscles.

2.1.2.5 The conduction system

The conduction system is made of specific heart cells that are histologically different than the rest of the heart muscle [26]. Those cells do not participate in muscle contraction, but rather they generate and propagate electric pulses that are responsible for the heartbeat. The conduction system, depicted in Figure 2.3, is constituted by the sino-atrial node, the AV node, the common AV bundle, the His bundle, the right and the left branches of the common AV bundle, and the peripheral branches of Purkinje. Additionally, there is also another group of atrial fibers that are considered to be part of the conduction system. They are the Bachmann's bundle and the internodal tracts of the right atrium. The sino-atrial node is placed in the right atrium at the junction with the superior vena cava corresponding on the epicardial surface to the crista terminalis. Several branches originate from the sinoatrial (SA) node to connect the atrioventricular (AV) node.
The AV node is placed on the floor of the right atrium to the left of the coronary sinus orifice. The common AV bundle takes origin from the bottom part of the AV node and descend the membranous part of the septum. At the junction between the membranous part and the muscular part of the septum, the common AV bundle splits into two branches that descend the septum from both sides. The left branch immediately splits into several branches distributed on the whole surface of the left ventricle. At the peripheral part, both the left and the right branches split up, forming the Purkinje fibers. Those fibers spread over the ventricular walls. The Bachmann's bundle is responsible for the conduction in the left atrium, and it takes origin from one of the branches of the

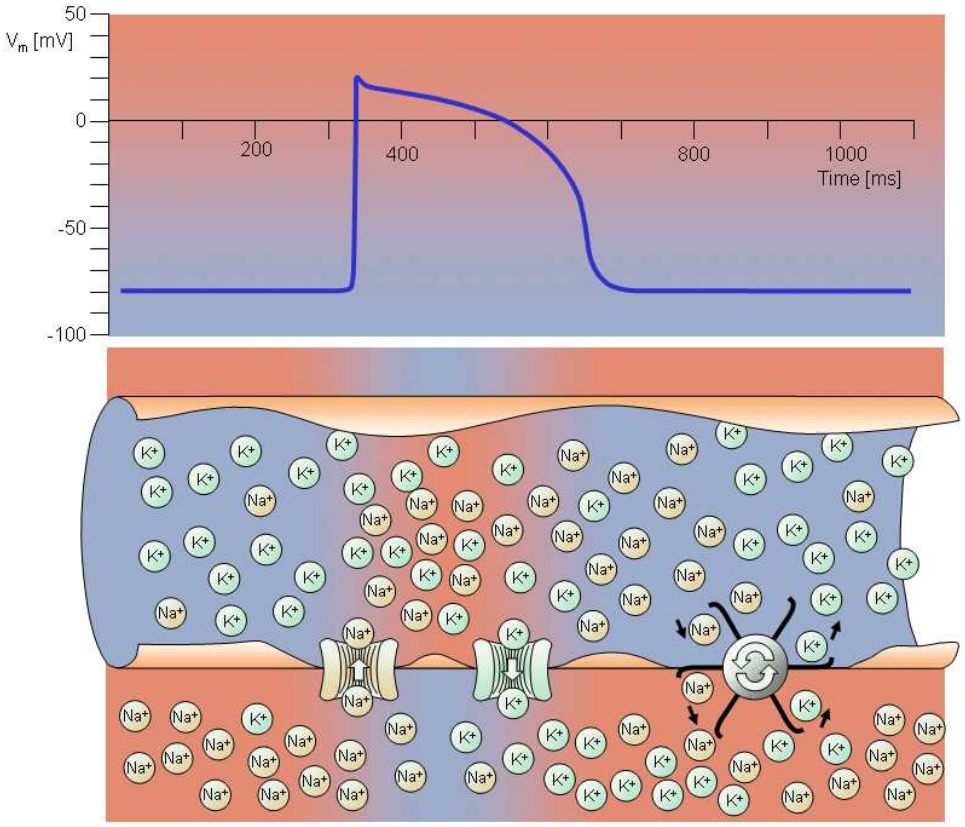

Figure 2.4: Action Potential of myocardium cells [1]

internodal tracts.

2.2 Electrophysiology

In healthy hearts, the contraction is driven by an electrical impulse that has its origin in a group of cells called pacemaker cells. The impulse propagates in a coordinated way using the conduction system and arrives in all the heart fibers inducing the contraction. The electrical activities of cells can be measured through their membrane potential that is defined as the voltage difference between the inner and the outer surfaces of the cell membrane.

The voltage drop across the membrane is generated by the difference in ionic concentration between the intracellular fluid and the extra-cellular fluid. The main ionic concentrations regulating the membrane potential are the Sodium (Na^+) and Potassium (K^+) ions. The concentration of K^+ of the intracellular fluid is 30 times greater than the concentration of the extra-cellular fluid. In contrast, the concentration of Na^+ is 30 times lower than the concentration of the extra-cellular fluid [25].

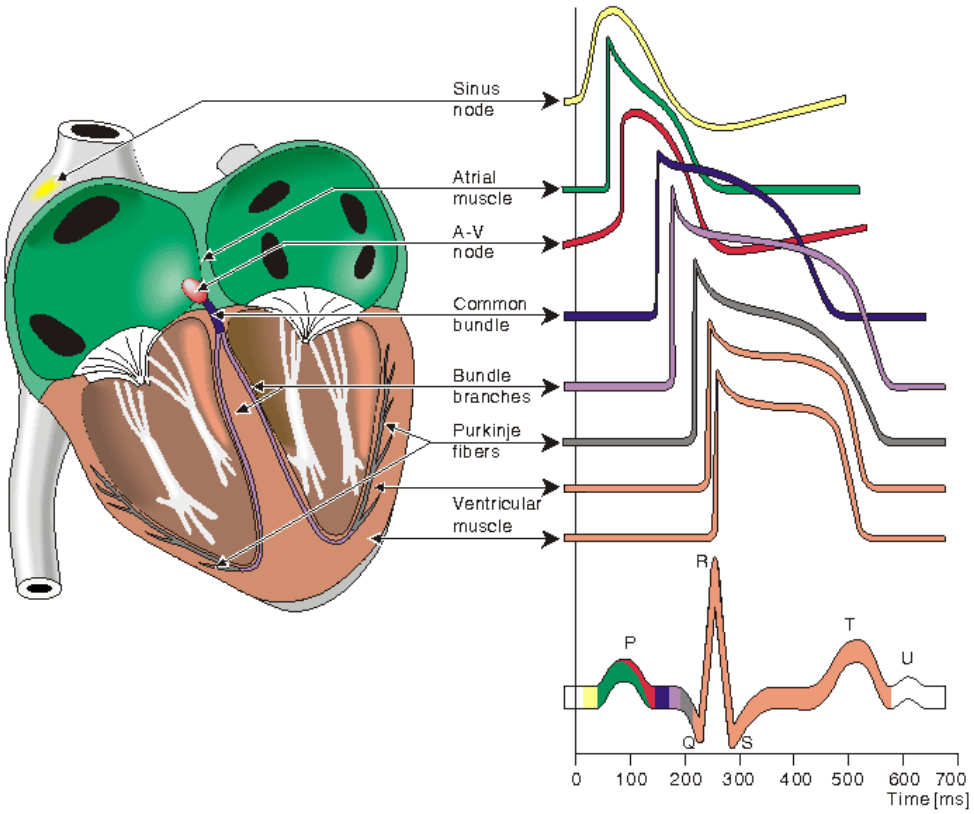

Figure 2.5: Electrophysiology of the heart through the conduction system [1]

At rest, the membrane is more permeable to the Potassium compared to the Sodium and is polarized to the rest value of -90 mV.
The electrical pulse coming from pacemaker cells initiates the action potential, which is defined as a rapid modification of the membrane potential compared to the rest value, as shown in Figure 2.4. In the first phase, the electric pulse modifies the permeability of the membrane allowing Sodium ions to flow into the cell rapidly. This inrush of positive charges induces the inversion of the polarization of the membrane, reaching a peak value of about 20-30 mV. After this quick movement of charges, the membrane permeability to K^+ decreases, reaching an almost null membrane potential that is kept for an amount of time (circa 300 ms). This period is called the *absolute refractory period* during which muscle cells keep contracting.
After this phase, the potassium permeability of the membrane is reestablished, and K^+ are expelled out of the cell. This causes the so-called repolarization of the cell. The repolarization of the cell consists of a fast decreasing of the membrane potential reaching the rest value of -90 mV.
An active cellular system, known as the *pump*, provide to expel the excessive sodium

ions and to reintegrate the Potassium ions to reestablish the rest ion concentrations. The propagation of the electric impulse is due to the electrical diffusion of ionic currents that triggers the action potential of adjacent cells. For this reason, the activity contiguously propagates from its origin to all the excitable fibers of the heart.

So far, we have described the action potential and the events that regulate its phenomenology. This is valid for all cardiac fibers composing the heart tissue. However, the action potential of the fibers composing the conduction system presents particular characteristics. Pacemakers cells have different electrical properties compared to standard myocardium muscle cells. Indeed, the resting potential of pacemaker cells is about -60mV. In such a condition, the pacemaker cells are easily and regularly depolarized. This event triggers the propagation of the electrical impulse by contiguity to the rest of the myocardium [10].
In normal circumstances, the depolarization impulse is generated by the pacemaker cells of the sino-atrial node. The depolarization rate is modulated by the autonomic nervous system that can make SA node accelerate (sympathetic system) or decelerate (parasympathetic system). The activation wavefront originating from SA node spreads over three preferential pathways (interatrial tracts) within the right atrium, and toward the left atrium through the Bachmann's simultaneously activating both atria. The activation wavefront reaches the AV node whose main task is to synchronize atrial and ventricular contractions. The autonomic nervous system also modulates the AV node, either facilitating (sympathetic system) or slowing down (parasympathetic system) the conduction. The His Bundle fascicles propagates the activation wavefront toward both ventricles. In Figure 2.5, the action potentials of the different heart fibers are represented in the time domain.
The overall electrical activity of the heart is commonly monitored through electrocardiograms (ECG). As we can see from the colored trace of the ECG in Figure 2.5, the sino-atrial activity is not detected by the ECG. The first detected event, called P-wave, represents the electrical activity of the depolarization of atrial muscular fibers. The propagation of the electrical impulse arrives at the AV node when the P-wave reaches its maximum value. The propagation of the impulse through the His bundle is slow and represents the PR interval. The QRS-complex represents the action potential of the muscular fibers of the ventricles. On the other hand, the ST-interval corresponds to the absolute refractory period of ventricles, where the T-wave is the representation of the repolarization of the ventricles. Finally, The U-wave corresponds to the repolarization of the specific tissue in the septum.

Here, we have described the electrical activity of healthy hearts. In the next section, we will introduce how electrical disorders of the heart activity can cause cardiac dysfunctions.

2.2.1 Cardiac Rhythm Disorders

Cardiovascular diseases are the principal cause of mortality in Europe, causing about 42% of deaths [27]. This work focuses on particular cardiac diseases, known as arrhythmias, which are heart rhythm disorders caused by dysfunctions of the conduction system. There are four main kinds of arrhythmias: premature contractions, bradycardia, supraventricular tachycardia, and ventricular tachycardia.

2.2.1.1 Premature contractions

Premature contractions are caused by ectopic depolarizations of the cardiac cells, i.e. cells not located in the SA node. A premature contraction can originate from either the atria or the ventricles. Thus, they are classified into premature atrial contractions (PAC) and premature ventricular contractions (PVC).
The depolarization impulse of PACs reaches the AV node, which transmits it to the ventricles as for normal sinus rhythm. Thus, PACs are often asymptomatic and, in most cases, do not need treatments [2].
On the other hand, PVCs alterates the normal conduction of the depolarization impulse. Indeed, during PVCs the ventricles contract before the atria, resulting in a inefficient pumping of the blood. Moreover, PVCs impair the interventricular depolarization, inducing contraction dyssynchrony. However, sporadic PVC events can be tolerated; whereas frequent PVCs can cause heart failure to occur [28].

2.2.1.2 Bradycardia

Bradycardia is a slow (less than 60bpm) and/or irregular rhythm that is not sufficient to pump enough oxygenated blood to the rest of the body. The origin of bradyarrhythmias is usually related to dysfunctions of the SA node or the AV node [29]. Sinus dysfunctions can manifest as [10]:

- the arrest of the atrial activity (see Figure 2.6), where the AV node takes the lead over the management of the heartbeat, resulting in a lower heartbeat (e.g. 40 bpm);
- chronotropic incompetence, when the SA node cannot respond to exercise with heartbeat rate acceleration.

AV node dysfunctions are known as atrioventricular blocks (AVB), which are divided into three degrees according to the severity of the dysfunction. The *first degree* is characterized by long PR intervals. The *second degree* is further divided into two types:

- The *type I* is characterized by a progressively lengthening of the PR interval over consecutive cardiac cycles, until the ventricle miss to contract for a cardiac cycle;
- In the *type II*, ventricles miss P wave association for one or several consecutive cardiac cycles (see Figure 2.7).

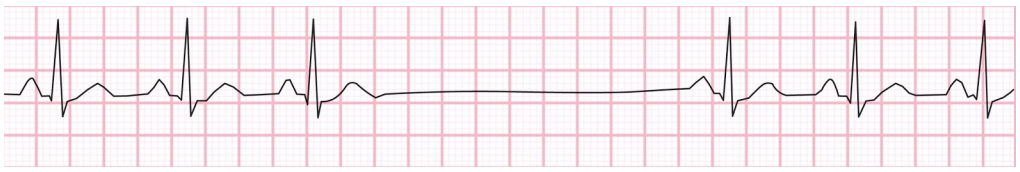

Figure 2.6: Sinus arrest event [2]

Figure 2.7: AV block of type II

In *third degree* AVB, the conductive channel between the atrium and the ventricles is completely interrupted. In this case, the ventricle contraction occurs at a lower rate than the atrial contraction and is driven by the pacemaker cells situated in the distal part of the His bundle branch.

2.2.1.3 Supraventricular tachycardia

Supraventricular tachycardia are abnormally fast heartbeat rates, originating either in the atria or in the AV node. The most common kind of Supraventricular tachyarrhythmias are: atrial tachycardia, and atrial fibrillation.
Atrial tachycardia is a fast (i.e. above 150bpm) and regular supraventricular rhythm, to which corresponds a normal conduction in the ventricle. Thus, supraventricular tachyarrhythmia events are typically tolerated.
The atrial fibrillation (AFib) is the most diagnosticated heart rhythm disorders [30]. It is an extremely fast atrial activity (i.e. above 300bpm) resulting in uncoordinated contractions of the atrium (see Figure 2.8). AFib is partially transmitted to the AV node, generating an irregular contraction rate of the ventricles. Two different AFib disorders can be distinguished according to the persistence: paroxysmal, persistent and chronical. Paroxysmal AFib occurs occasionally and usually stop spontaneously. Episodes can last a few seconds, hours or a few days before reestablishing normal sinus rhythm. Research

Figure 2.8: Atrial fibrillation event

studies have shown that around 40% people with AFib have paroxysmal AFib [31]. Persistent AFib is defined as an AFib episode that lasts more than one week, requiring medical treatments to be stopped. Chronic AFib is defined as AFib event lasting for many years. It is common that patients suffering from Paroxysmal AFib gradually develop chronic AFib [32]. Indeed, statistical researches have shown that 9 to 30% of all cases of paroxysmal AFib progress into more chronic cases after 1 year.

2.2.1.4 Ventricular tachycardia

Tachycardia is manifest in the opposite way of bradycardia: the heart beats too fast and, in some cases, irregularly. The tachycardia beat rate varies from more than 100bpm up to 400bpm. In such a condition, the heart is not able to work efficiently and can fall to Ventricular Fibrillation when only 10% of the blood is ejected from ventricles due to uncoordinated contraction. It is an extremely dangerous disease that can lead to Sudden Cardiac Death.

2.2.1.5 Congestive Heart Failure (CHF)

Congestive Heart Failure occurs when the heart is not able to respond to the oxygen demand of the body due to an inefficient and or weak contractions of the ventricles. CHF can be thought as the inefficiency of the heart ventricles to regulate the blood flow, due to ventricular dyssynchrony.

2.2.2 Cardiac Rhythm Management devices

Arrhythmia disorders are first treated with medications and, in some cases, with surgical operations. For some critical cases, medications are not sufficient to counteract heart dysfunctions. To overcome drug immune arrhythmias, it is a standard procedure to implant Cardiac Rhythm Management (CRM) devices. There are as many medical devices as there are kinds of arrhythmia.

2.2.2.1 Pacemakers

Cardiac Pacemakers are used to treat bradycardia patients. Pacemaker devices must sense spontaneous heartbeat and pace by electric stimulation whenever the heartbeat rate is too slow.
Conventional pacemakers consists of a hermetically sealed Titanium can, containing electronic components and a battery. The can is subcutaneously implanted in the chest below the collarbone. One or more leads are used to reach the heart chambers from the can. The leads are used to release electric stimuli and to sense local depolarization of the heart tissue.The number of the leads varies according to the severity degree of the heart dysfunction. Pacemaker with a single lead can be used to sense and pace a single location of the heart and are known as *Single Chamber Pacemakers*. These

Pacing	Sensing	Mode of function
V (ventricle)	V (ventricle)	I (Inhibited)
A (atrium)	A (atrium)	T (Triggered)
D (dual)	D (dual)	D (both)
O (neither)	O (neither)	O (neither)

Table 2.1: Pacemaker international nomenclature

devices use to pace the heart at the end of an escape interval that is restarted during every cardiac cycle. Pacemakers integrates electrogram (EGM) sensor to monitor the local electrical activity of the tissue. Pacemakers can have a dual reaction to physiologic cardiac event. They can be programmed to inhibit or trigger the artificial stimulation whenever a cardiac event is detected.
Nowadays, single chamber pacemakers are usually used only for patient suffering of AVB with chronic atrial arrhythmia. In most of the cases, it is preferred to treat bradycardia patients with *Dual Chamber Pacemakers*, where two leads are used to reach respectively the RA and the RV. Pacemakers can integrate pacing algorithms allowing rate responsive stimuli, improving the cardiac output especially during exercise.
Pacemakers are classified according an international code consisting of at least three over five letters that are resumed in Table 2.1. The first two letters indicate respectively the pacing and the sensing chamber, which can be the ventricle (V), the atrium (A), or both (D); the third letter indicates the response type to a detected ECG event, which can trigger (T) or inhibit (I) a stimulation pulse; the forth and the fifth letters stand for particular functionalities such as rate responsiveness, and anti-tachycardia pacing.

2.2.2.1.1 Atrioventricular synchronization

An important achievement that Dual chamber pacemakers introduced in the treatment of bradycardia patient is the possibility to optimize the AV synchronization (AVS), improving the quality of life of the patient. Indeed, dual chamber pacemakers can sense both the RA and the RV activity. Thus, they can adapt the stimulation optimizing the hemodynamic status on a beat-to-beat basis.
As a result, the AVS establishes cooperation between atrial systole (i.e. blood ejection through the AV valves) and ventricular diastole (i.e. ventricular filling), improving the cardiac output [10].

2.2.2.2 Implantable Cardioverter Defibrillator

Tachycardia dysfunctions are treated employing Implantable Cardioverter Defibrillator (ICD) devices. The ICD continuously monitors the heart and delivers high energy shocks whenever tachycardia is detected to stop the harmful tendency of the heartbeat rate.

As well as Pacemaker devices, ICDs are subcutaneous devices and use a lead to deliver proper therapies.

2.2.2.3 Cardiac Resynchronization Therapy (CRT) device

For what concerns congestive heart failure, physicians recommend to implant Cardiac Resynchronization Therapy (CRT) devices. CRT devices send small electrical pulses to different chambers, improving heart contractility and pumping efficiency of the heart. Two leads are placed inside the right atrium and the right ventricle, while a third lead is placed on the epicardial surface of the left ventricle. CRT devices can be either pacemaker based (CRT-P devices) or defibrillator based (CRT-D devices). If a patient is at risk of Tachycardia events, a CRT-D will be used; otherwise a CRT-P device can be used for heart chamber synchronization.

2.3 Leadless Pacemakers

Recent studies confirm that lead extraction is still the most risky procedure among all heart rhythm disorder management procedures. Patient undergoing lead extraction have a mortality rate of 1.9% due to the complexity of the procedure itself and for infections that leads could arise [33]. Moreover, frictions between two or more leads in Cephalic or Subclavian Veins can arise microdislodgements, altering the correct functioning of the device. Sometimes, leads can cause complications as cardiac perforations due to a local pressure on the heart tissue that depends on both the stiffness of the lead and the size of the contact surface with the heart.
Nowadays, thanks to electronics downscaling, it is possible to integrate all pacemaker functionalities in small capsules that are directly implanted in heart chambers. Those capsules are anchored at the heart tissue through transvenous catheters and deliver therapies by means of electrodes without the need for leads. This kind of devices are known as Leadless Cardiac Pacemakers (LCP).
The first clinical attempt with a LCP prototype was performed by William Spickler in 1970 [34]. Spickler's prototype showed the feasibility of the LCP concept through canine pre-clinical experiments. Spickler's intracardiac stimulation concept has become a reality thanks to battery improvements, but the mechanism of the delivery tool and the size of modern capsules are very similar to its primitive prototype [35].
Recent studies have shown that LCP have lower complication rates compared to standard transvenous lead pacemakers [36]. One of the major benefits of LCP is the absence of a pocket and a reduction in foreign material, reducing infection incidence [37]. However, Leadless pacemakers, as standalone devices, can only be used for single chamber therapies, limiting the eligible patient population.

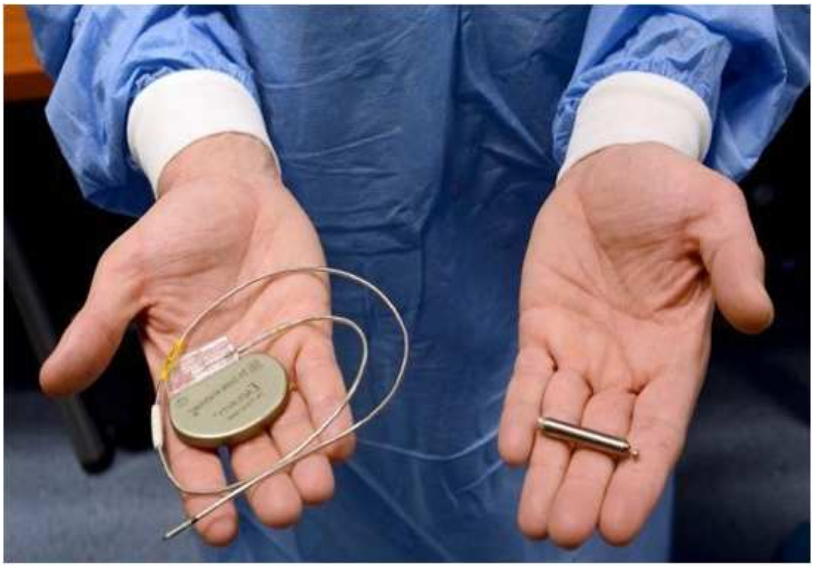

Figure 2.9: Standard Cardiac Pacemaker on the left hand side and Leadless Cardiac Pacemaker (Nanostim, St. Jude) on the right hand side.

2.3.1 Accelerometer-based atrioventricular synchronization

Leadless cardiac pacemakers are the cutting edge of the CRM technology. However, we currently have only single-chamber solutions, limiting the eligible patient population. For several years, LCPs were limited to operate as VVI-pacemakers, which can deliver the therapy only in the RV and adapted to the sensing of local cardiac activity.
Recently, *Medtronic* received FDA approval for upgrading its LCP, Micra™, to operate in VDD-mode. *Medtronic* solution relies on complex algorithms processing 3D-accelerometer signals. Indeed, it was a smart approach to upgrade the LCP functionality to an unconventional VDD-pacemaker, where the RV stimuli are synchronized with the mechanical activity of the RA instead of the P-wave. Clinical studies showed promising results, achieving atrioventricular synchronization (AVS) in 80% of cases for patient suffering of AV-block at rest[38]. However, there are still significant improvements that the scientific community should advance.
Clinical studies demonstrated that accelerometer-based solution was impacted by patients' activity. Figure 2.10 shows the percentage of AVS according to the particular maneuvers. It can be seen that AVS fails for the 40% of events during fast walk. This limit depends on two factors[38]:

- the mechanical noise artifact due to patient movement;
- the complexity to discriminate atrial activity and ventricular activity as the heart rate increases.

Moreover, undersensing issues arise for patients with low atrial contractility, for which

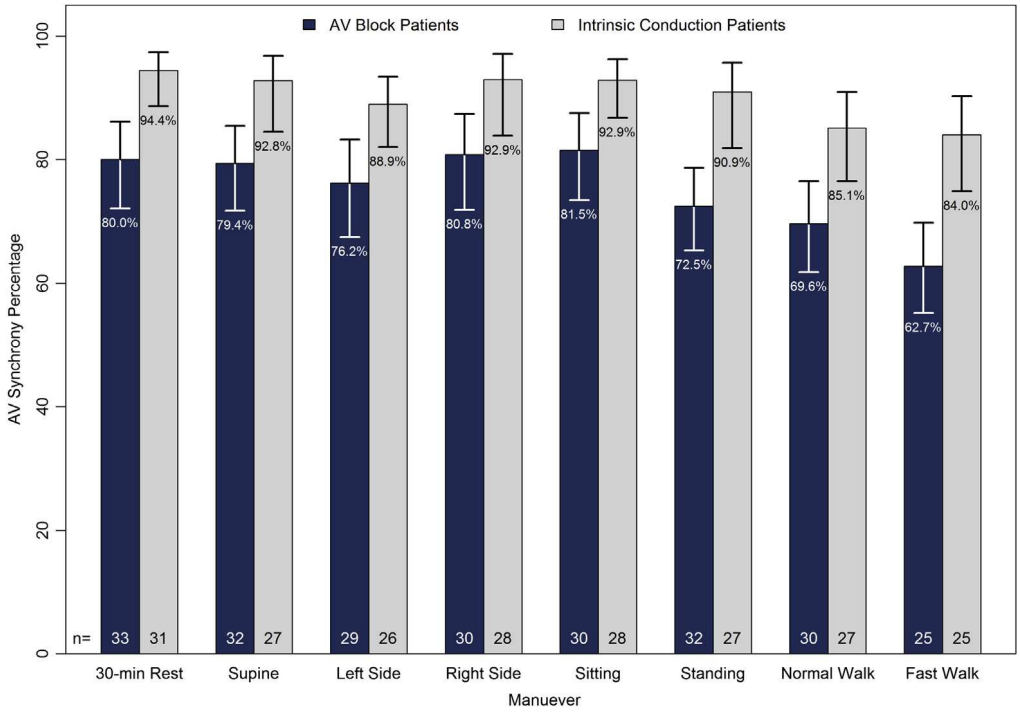

Figure 2.10: AVS percentage of Micra™ during different maneuvers.

the atrial contraction does not exceed the detection threshold of the accelerometer signal. Thus, the AVS is guaranteed for a limited patient population, during a limited amount of time (at rest).
Even though, the study demonstrated the benefit in terms of cardiac output when AVS is obtained, it is possible that missing the AVS can lead to a progressive evolution of the disease toward the congestive heart failure (CHF)[39].
To overcome the limits of the LCP, the scientific community has been spending efforts to propose multiple-chamber solutions.

2.3.2 Multi-node LCP systems

To implement all the functional modes of conventional pacemakers, two or more LCPs might be implanted in different chambers of the heart. For example, a leadless CRT-P system is represented in Figure 2.11, where two endocardial LCP are placed respectively in the RV and in the RA; whereas an epicardial LCP is placed on the external surface of the LV.
Recently, *Bereuter et al.* performed the firsts attempts of multi-node pacing using physically separate devices, proving the clinical feasibility of both dual chamber and CRT-P leadless pacing [22, 20]. In particular, the authors suggested a telemetry-based synchronization of LCPs, using a conductive communication, known in the scientific community

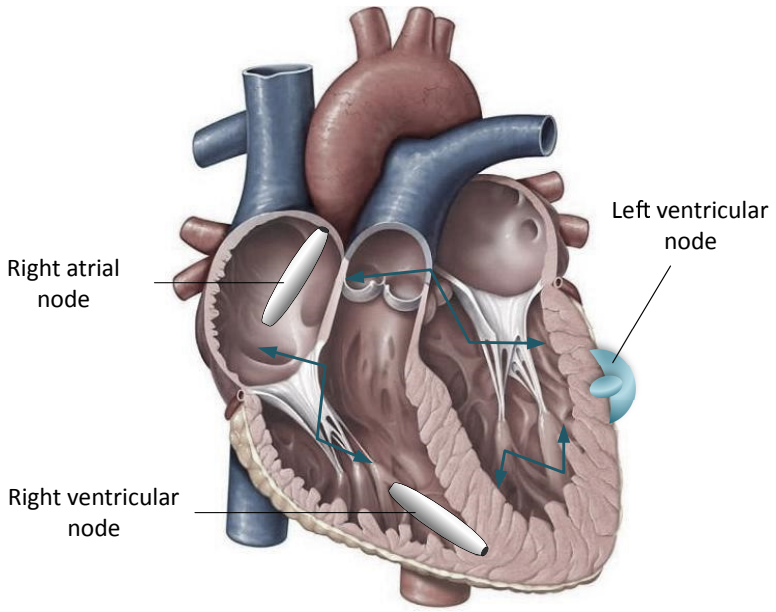

Figure 2.11: LCP network for CRT therapy. The heart figure has been modified and reprinted by permission of Pearson Education, Inc., New York, New York [3].

as Intra-Body Communication (IBC). This solution was verified using off-the-shelf components, without assessing the power optimization of the circuitry. The synchronization message was modulated through the pulse position, achieving a synchronization delay as low as 0.9 ms.
The same authors performed a preliminary characterization of the channels to estimate signal attenuation in the range [1 kHz - 1 MHz]. They showed the advantage of working in the high frequency domain, and the independency of the attenuation concerning hematocrit levels. Moreover, it was estimated that the hemodynamics (i.e. the heart movement) impacted the attenuation of less than 5 dB. The in vivo trials were performed injecting needle pairs in epicardial positions, where the emitter and the receiver pairs were almost parallel during the tests. A real-case scenario, using capsules in endocardial position is required to verify the attenuation levels, possibly increasing the spectral analysis of the attenuation. Furthermore, an exhaustive characterization including the impact of capsule orientation should be performed, to estimates the attenuation levels in the worst-case scenario.

In the following section, we focus our attention on the Intra-Body Communication, describing its main characteristics.

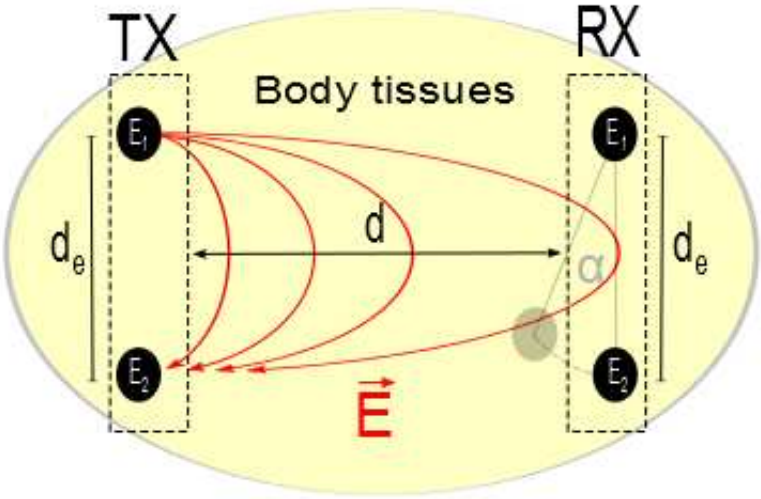

Figure 2.12: Galvanic IBC scheme

2.4 Intra Body Communication (IBC)

IBC is a relatively new ultra-low-power communication. The first attempts were performed by *Zimmerman*[16] during the 90's. IBC can be a promising solution to reduce the telemetry power budget for deep-implant device communications.
Technically speaking, IBC is a near-field communication based on Ohmic transmission through body tissues. Indeed, an electrode pair is used to build up an electric field that propagates through the human body, reaching a second electrode pair used to receive the signal.
The propagation media of IBC are the biological tissues, whose dielectrical properties depends on intra- and extra-cellular polarization mechanisms that counteract the charge diffusion. A more detailed description of the main equations predicting the electrical properties of biological tissue are described in subsection 3.1.2. By now, let us state that the electrical properties of the tissue play a key role for the IBC signal propagation.
Furthermore, there are other external factors that impact IBC signal attenuation, represented in Figure 2.12. The main variables characterizing the IBC channels are: the mutual orientation between the receiving and the emitting dipoles (α), the channel length distance (d), and the inter-electrode distance (d_e).

There are two main kinds of IBC topologies (Figure 2.13) depending on whether the electrode pairs are coupled between each other through earth ground o̊the conduction flows only through body tissues. Those two different configurations are called respectively Capacitive-IBC and Galvanic-IBC. In Capacitive-IBC, one electrode of each pair is floating. As a result, it is capacitively coupled with earth ground through the air.

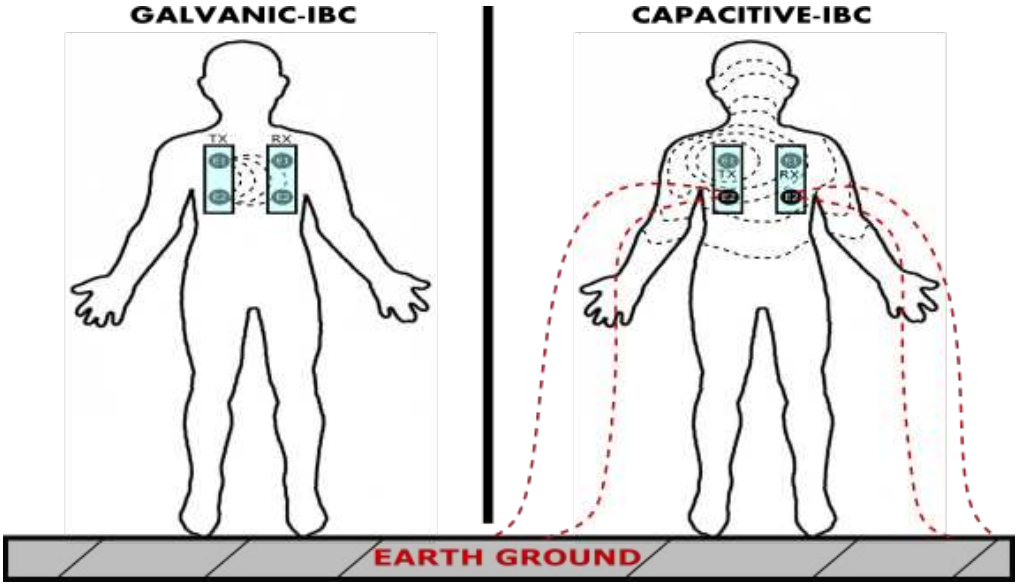

Figure 2.13: Different types of Intra-Body Communication.

For what consists Galvanic-IBC, both electrodes of each pair are in contact with body tissues keeping the communication galvanically isolated from earth ground reference, suggesting the name of this topology. Capacitive-IBC has lower attenuation levels with respect to galvanic IBC, although ground coupling makes the channel more noisy and posture dependent [40]. Both techniques have their own advantages and disadvantages depending on the application and design requirements. Capacitive-IBC is preferable for high distance body surface communications that can be used to transmit information between wearable devices. On the other hand, Galvanic-IBC is more suitable for short distance communication and whenever a robust communication against interference is required.

From the dawn of the IBC communication, several studies have been performed in order to characterize the human body as a communication channel. Two main approaches have been suggested to model IBC channel. The first is based on equivalent circuit modeling, and another is based on computational electromagnetic modeling. The Equivalent circuit modeling is a simplified solution that represents the human body by a 2-port network whose coefficient comes from the bio-impedances of the tissues. Impedances are calculated by simple geometrical assumptions, knowing the dielectrical properties of the tissues. The Computational Electromagnetic Modeling (CEM) is a computer based methodology based on numerical analysis methods.

Several analyses have been done for the IBC communication on the skin surface [17, 41], showing that the channel pathloss does depend on several parameters. However, there is still a lack of studies in terms of channel characterization for implantable devices. A first approach of IBC channel modeling for implant devices was proposed in [42] where a

boundary conditioned problem is analytically solved for IBC communication in a limb. The study shows the importance of the geometry of the model despite the fact that an approximated body model was used.

This chapter started with a rough anatomical description of the rib cage, in which most of the galvanic-IBC signals, emitted by LCPs, will be confined. The organ which is directly related to the application is the heart. Thus, we gave a background on the cardiac electrophysiology, pointing out the microscopic phenomena though the conduction system of the heart. Then, a summary of the main disorders related to the conduction system were reported, followed by the implant devices used to counteract each cardiac rhythm abnormality. A particular attention was given to the cardiac pacemaker, pointing out its main characteristics and limitations. It was shown that Leadless Cardiac Pacemakers reduce post-surgical complication rates compared to conventional pacemakers, integrating all the components in a single capsule. The Leadless pacemaker was described, focusing on the solutions to establish atrioventricular synchronization. We have seen that accelerometer-based solutions can achieve good AVS results at rest; however the performance of such a technique is highly impacted by the physical activity. Multi-node LCP systems can overcome this limit using wireless communication to synchronize the devices. The Intra-Body Communication seems the most suitable physical layer for LCP communication. Thus, the work of this study focuses on IBC technology. In the next chapter, we deal with preliminary studies related to the characterization of the communication channels. This is an essential step to design power-efficient communication modules for LCP applications.

3 IBC channel characterization

The World Medical Association agreed in the Declaration of Helsinki that animals should only be used in biomedical research when it is clear that their use is required to achieve an important outcome, and where no other feasible method is available [43].
Here, we propose a methodology to estimate IBC attenuation for leadless pacemaker applications using in silico simulations. This methodology allows fast estimations of the channel attenuation that can reduce the number of experiments required. The model was then verified with in-vivo measurements using a novel experimental setup.

3.1 Simulations

In Silico experiments have improved in the last decades thanks to the increasing of power calculation of computers. Among other things, they can be used for a preliminary estimation of the attenuation in human body. In this section, we propose a method for IBC channel characterization using an accurate torso model. First, some physical consideration are pointed out to explain the importance of having accurate models when considering IBC signals. All IBC channels involved in Leadless Cardiac Pacemakers are investigated. In particular, the attenuation results of three different channels are pointed out: Intra-cardiac channel, Inter-ventricular channel, and Trans-thoracic channel. Then, the mathematical method and the methodology are described. For the sake of completeness, we compare the results between the accurate torso model and another one that was constructed by simple geometrical shapes.

3.1.1 Geometrical considerations

The Electric Field flux enclosed in the surface Σ, generated by a continuous distribution of charges, is characterized by the charge spatial density $\rho(x, y, z)$, as stated by the Gauss'law. The Gauss'law is represented by equation (3.1), where the integral enclosed by surface Σ represents the total charge contained in the volume τ.

$$\Phi(E) = \frac{1}{\epsilon_0} \int_{\Sigma} \rho(x, y, z) d\tau. \tag{3.1}$$

The emitting dipole of IBC channel generates an Electric field whose flux obeys to Equation 3.1. Human body is an anisotropic environment where the analysis of the electric field distribution is not analytically straightforward. Thus, software based numerical computations can be used to study the Electric Field in such a complex volume. To do so, we used an accurate human torso model with a geometrical resolution of 0.5 mm that is described in detail in subsection 3.1.5.

3.1.2 Dielectric properties of human body tissues

Dielectric properties of materials have been the object of empirical studies for more than a century and several models based on the relaxation constant have been proposed so far by the scientific community. The simplest way to model dielectrics is given by the Debye formula that is shown in (3.2)

$$\epsilon^* = \epsilon_\infty + \frac{\Delta\epsilon}{1 + (j\omega\tau)} + \frac{\sigma}{j\omega\epsilon_0}, \tag{3.2}$$

where ϵ_∞ represents the permittivity value far above the relaxation frequency, ϵ_s is the static permittivity, $\Delta\epsilon = (\epsilon_\infty - \epsilon_s)$ is called dielectric strength, τ is the relaxation time and σ is the conductivity, while ϵ_0 is the permittivity of the free space. Body tissues are complex materials whose permittivities experience more than a single relaxation constant. This could arise from the superposition of several relaxation processes due to different polarization effects [44]. This behavior was firstly discovered in 1941 by two brothers called *Robert H.* and *Kenneth S. Cole* who introduced an additional factor α to Debye's equation as shown in eq.3.3. This equation, known as Cole-Cole equation, better fit the relaxation constant concerning its frequency behavior.

$$\epsilon^* = \epsilon_\infty + \frac{\Delta\epsilon}{1 + (j\omega\tau)^{1-\alpha}} + \frac{\sigma_s}{j\omega\epsilon_0}. \tag{3.3}$$

In the early nineties, *Camelia Gabriel* measured over 20 biological tissue in the frequency range between 10Hz and 20GHz. To fit the measurements, she proposed a four-term Cole-Cole equation that is shown in 3.4 [45]. This equation considers separately the different polarization effects that are experienced in biological tissues.

$$\epsilon^* = \epsilon_\infty + \sum_{n=1}^{4} \frac{\Delta\epsilon_n}{1 + (j\omega\tau)^{1-\alpha_n}} + \frac{\sigma_s}{j\omega\epsilon_0}. \tag{3.4}$$

Our study is based on *Gabriel et al.* work whose data are publicly available in several database such as the web application of the *Institute of Applied Physics* of *CNR* [46].

3.1.3 Finite Element Method

The Finite Element Method (FEM) is a numerical technique that allows solving problems of partial differential equations with an elegant approach. The FEM applies the old concept of "divide et impera" to mathematics. Indeed, the FEM is used to solve problems in complex regions, called domains, dividing it in several sub-elements, called meshes. The problem is solved independently for each mesh and then sum up each contribution to find the global solution. Mathematically speaking, the FEM relies on the method of weighted residuals and on the concept of shape function that was well interpreted by Galerkin in early fifties of the XX century.
Hereafter, some mathematical concepts are treated to let the reader have a grasp of what FEM consists in without too many details since an exhaustive description of the method is out of the scope of this manuscript, and a more detailed description can be found in the literature [47].
Let us consider the Poisson equation that analytically describes several physical phenomena such as electrodynamics. In particular, we will consider one-dimension problems, but a the generalization to 2D or 3D domains is straightforward.

$$\frac{\partial^2 \phi}{\partial x^2} = -\frac{\rho}{\epsilon}. \tag{3.5}$$

The FEM finds approximated solutions introducing an error, the residual, that is defined as the difference between the true solution and the approximated solution:

$$R(\phi, x) \equiv -\frac{\partial^2 \phi}{\partial x^2} - \frac{\rho}{\epsilon}. \tag{3.6}$$

We can now multiply the residual function by a weighting function $W(x)$ and force the integral of the overall expression to zero.

$$\int_0^L W(x) R(\phi, x) dx = 0. \tag{3.7}$$

According to Galerkin's approach, the weights are set equal to the shape functions $N_i(x)$. The problem is synthesized to a set of linear equations with the same number of equations as unknowns.

$$\int_0^L N_i(x) \left[-\frac{d^2 \phi}{dx^2} - \frac{\rho}{\epsilon} \right] dx = 0. \tag{3.8}$$

Integrating by part the second derivative term, we can reduce the complexity of the problem to an equation of order one, called weak formulation.

$$\int_0^L \frac{dN(x)}{dx} \frac{d\phi}{dx} dx - N(x) \frac{d\phi}{dx}\bigg|_0^L - \int_0^L N(x) \frac{\rho}{\epsilon} = 0. \tag{3.9}$$

The FEM relies on piece-wise polynomial approximations whose accuracy depend on the degree of the polynomials chosen as $O(h^n)$, where h is the length of the meshing element and n is the degree of the polynomial. Using the weak form of the problem allows

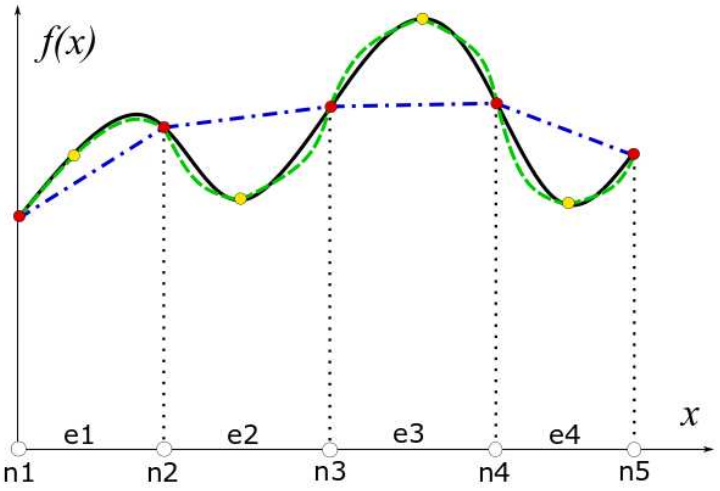

Figure 3.1: Piecewise linear versus piecewise quadratic approximation

to use linear approximation, but higher order can be applied to reach lower errors, with the cost of increasing the number of linear equation and consequently the computational effort of the solver [47].

The first decision that must be faced approaching the FEM concerns the number of nodes and the geometry of the meshing elements. For each node, there is a shape function $N(x)$ such that $N_i^{(e)}(x_i) = 1$ and $N_i(x_j) = 0$ when $i \neq j$. Using the shape functions, it is possible to represent the function $\phi(x)$ as the sum of each contribution coming from each meshing element such that

$$\phi(x) = \sum_{i=1}^{n+1} N_i^{(e)}(x)\phi_i, \tag{3.10}$$

where ϕ_i is the value of $\phi(x)$ on the node i and $N_i^{(e)}$ is the set of shape functions for the element e. This new representation of $\phi(x)$ can be used to solve the problem 3.9. The FEM proposed so far is adapted to solve steady-state problems, but it is also possible to extend the method to time variant problems. In this case $\phi(x)$ becomes $\phi(x,t)$ where t is the time variable. However, it is required to specify the initial condition $\phi_0(x)$ to find the particular solution of the problem [47]. On the other hand, shape functions are only space dependent and $\phi(x,t)$ can be represented as

$$\phi(x,t) = \sum_{i=1}^{n+1} N_i(x)\phi_i(t). \tag{3.11}$$

At each node of the mesh, a set of linear algebraic equations must be solved. The description of the numerical method to find out the approximated solution using the FEM is widely described in the literature [47] and it is out of the scope of this manuscript.

3.1.4 Quasi-static approximation

Maxwell's equations can fully describe electromagnetic phenomena such as IBC signals. However, the complexity of the set of equations would require a massive amount of time to find a convergent solution. Quasi-static set of equations provide an intermediate level between static analysis and the complete electrodynamics. Indeed, quasi-static assumptions decouple Electric field $\mathcal{E}$ and Magnetic field $\mathcal{H}$ since the velocity of the magnetic field field flux $\mathcal{B}$ does not contribute to Electric field magnitude and vice versa as can be seen from the set of equations (3.12), where the magnetic current density and magnetic charges have been neglected since we suppose that no magnetic sources are applied.

Maxwell's equations: *Quasi-Static approximation:*

$$\begin{cases} \nabla \times \mathcal{H} &= \frac{\partial \mathcal{D}}{\partial t} + \mathcal{J} \\ \nabla \times \mathcal{E} &= -\frac{\partial \mathcal{B}}{\partial t} \\ \nabla \cdot \mathcal{B} &= 0 \\ \nabla \cdot \mathcal{D} &= \rho \end{cases} \implies \begin{cases} \nabla \times \mathcal{H} &= \frac{\partial \mathcal{D}}{\partial t} + \mathcal{J} \\ \nabla \times \mathcal{E} &\approx 0 \\ \nabla \cdot \mathcal{D} &= \rho \end{cases} \tag{3.12}$$

Let us now point out the error introduced by Quasi-static assumption. To do so, we will find the contribution of the magnetic field to the electric field for the solution of the classical Maxwell's equation. Maxwell's equation are analytically solved as the solution of the inhomogeneous Helmoltz equation. In stationary domain, the electric field can be fully determined from the magnetic vector potential $\mathbf{A}$ and the scalar electric potential V as shown in the set of equations (3.13).

$$\begin{cases} \mathbf{E} = -j\omega\mathbf{A} - \nabla V \\ \mathbf{A} = \frac{\mu}{4\pi} \int_{V'} \frac{\mathbf{J_s} e^{-jk\mathbf{R}}}{\mathbf{R}} dV' \\ V = \frac{1}{4\pi(\sigma + j\omega\epsilon)} \int_{V'} \frac{\rho e^{-jk\mathbf{R}}}{\mathbf{R}} dV' \end{cases} \tag{3.13}$$

The error introduced using Quasi-Static equations comes from the magnetic contribution to $\mathbf{E}$ that can be described as 3.14 [48, 15].

$$|\frac{\omega \mathbf{A}}{\nabla V}| = |\omega^2 \mu \epsilon R_{tx}^2|, \tag{3.14}$$

where ω is the angular frequency, R_{tx} is the dipole length of the emitter in meters, μ and ϵ are respectively the magnetic permeability and the electric permittivity of the transmission medium.

It is our interest to have a wide frequency characterization of the IBC channel attenuation for Multi-node leadless pacemaker applications. In this work, we decided to set the upper frequency limit to 20 MHz to approach the IBC-band chosen by the IEEE community, which is defined as Human Body Communication (HBC) in the *IEEE802.15.6* standard [49].

Knowing that $\mu_{tissue} \approx \mu_{air}$, $\epsilon_{blood}(20\ MHz) = 154.56$ and setting the length $R_{tx} = 33mm$, that is the length of the LCP prototype used in this study, we find a relative error of almost 3%, that can be considered as an acceptable limit.

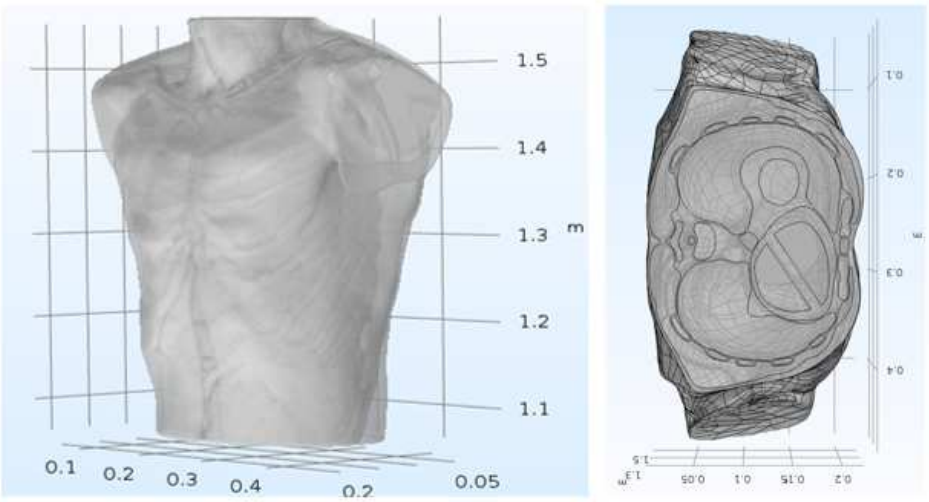

Figure 3.2: Torso CAD model imported in COMSOL environment. Cross sectional cut of the torso CAD model.

3.1.5 Simulation methodology

Numerical analyses have been often used in previous studies on body surface communications where simple geometry models can approximate body channels [17, 50, 51]. This is not the case for in-body sensor applications such as leadless cardiac pacemakers where anisotropy and geometry play a key role in the channel pathloss evaluation.
To fairly represent the distribution of the eletric field for deep-implant communication, an accurate torso model was designed. The model was used to perform electrical quasi-static simulations allowing the pathloss estimation of all the channels involved in leadless pacemaker applications. The model geometry was based on a validated human model from *IT'IS foundation Zurich*. We chose Duke of the Virtual Population (ViP2.0), which represents a 34 years old man model retrieved by CT scan images with a resolution equal 0.5 mm.
The NURBS module of *Simpleware Software Solution* was used to build a geometrical model that included organs, muscles, bones, soft tissue and cartilages from spatial information of Duke [52]. The geometrical model was imported in *COMSOL Multiphysics 5.3* where it was enhanced to accurately resemble physiological characteristics such as the size and volume of the chambers [53, 54]. The volume of each designed chamber is reported in Table 3.1. Chamber geometries were designed reproducing a down-scaled copy of the heart that was further modified thanks to local work-planes operations to introduce the spacing between each chamber.
The resulting model discriminates blood and heart tissue as they have different electrical properties. The overall geometry model is shown in Figure 3.2 (left), whereas a cross sectional image of a plane parallel to the base of the model is depicted in Fig-

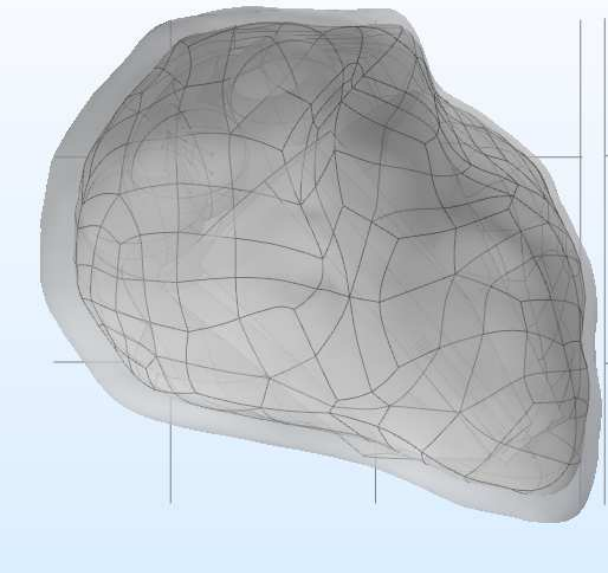

Figure 3.3: Heart CAD model modified to include the outer fat layer.

ure 3.2(right). A similar procedure was used to enhance the heart modeling to consider the epicardial fat. Fat tissue usually covers hearts with a distribution and volume that is different for each patient. For the fat effect study, we considered to have a floating heart not uniformly distributed as described in [55], where most of the fat is placed on the heart surface of right chamber side. The overal size of the model of the heart was not changed, partial volumes of the original heart tissue were used to represent fat tissue and blood.

The intra-cardiac channel is defined as the communication link between right chambers. To estimate the attenuation levels of the intra-cardiac channel, two capsules, like the one shown in Figure 3.4, were directly designed in COMSOL having similar volume of other LCP capsules that are currently on the market [36]. The total length of the capsule was 33 mm, whereas the diameter of the can was equal to 6.4 mm. Distal and proximal electrodes were chosen to maximize the inter-electrode impedance. The distal electrode was designed as a platinum disk with diameter equal to 1.5mm and total contact surface equal to 4 mm^2, whereas the proximal electrode was retrieved from the delivery pin of the capsule, that was designed as stainless steel void cylinder with contact surface and height respectively equal to 22 mm^2 and 2.5 mm.
The capsules were placed respectively in the RV and in the RA in positions commonly used for pacemaker leads. The RV capsule was fixed at the apex of the heart, whereas the RA capsule was fixed at the free wall.
Two different orientations have been simulated to take into account the minimum and the maximum angle of the mutual orientation of the capsules as shown in Figure 3.5.

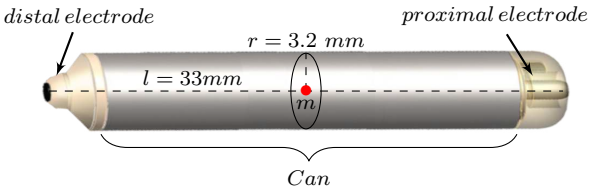

Figure 3.4: Leadless pacemaker prototype used for IBC channel studies. Distal and proximal electrodes are spaced apart 33 mm. The can of the prototype has a diameter of 6.4 mm.

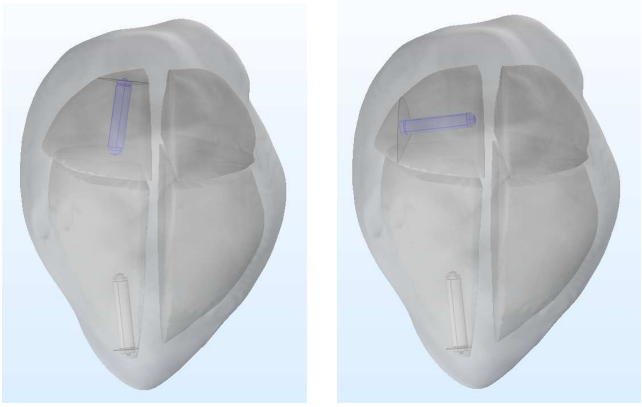

Figure 3.5: Positioning of the capsule in the right atrium showing. Parallel positioning in the left side image, whereas a perpendicular positioning is shown in right side image. The distance between the centers of the capsules is the same in both cases and equal to 9cm.

Both orientation scenarios had a channel distance of 9 cm, calculated as the distance between the median points of each capsules. The RV capsule was also used as emitter for the inter-ventricular channel.
To characterize the inter-ventricular channel, six voltage point probes were placed on the free wall of the LV epicardium as shown in Figure 3.6, indicating the voltage differences of adjacent probes. Adjacent probes are 1.5 cm apart, which is a reasonable assumption for a hypothetical bipolar epicardial pacemaker device. The RV capsule, placed at the right ventricle apex, has been used to set emitter boundary conditions for this analysis. The channel lengths were calculated between the median point of the RV capsule and median points of each adjacent probes and were equal to: 8.6 cm (P1), 7.5 cm (P2), 6.25 cm (P3), 5.2 cm (P4) and 4.2 cm (P5).
Furthermore, a real case study was performed extruding from epicardial surface of the heart two identical disk electrodes with diameter equal to 2 mm, height equal to 1 mm

Table 3.1: Heart chamber volumes of the CAD model

Chambers	**RA**	**RV**	**LA**	**LV**
Volume	53ml	96ml	41ml	100ml

and inter-electrode distance set to 1.4 cm. This real case scenario was used to reproduce similar conditions as the in vivo measurement setup.
The Torso was surrounded by a sphere of air with radius equal to 0.6 m whose outer surface was set as infinite boundary to avoid that unwanted reflections of the electric field alter simulation results.
Conductivity σ and relative permittivity ϵ_r of the biological tissues are frequency dependent [56], and have been set using parametric functions with values acquired from Gabriel's studies [45]. In the *Materials* interface of COMSOL, ten-point interpolating curves were defined in the frequency domain to model conductivity and permittivity of biological tissues, covering the whole spectrum of interest. The metallic materials and the air were taken from COMSOL libraries, whereas peek and parylene dielectric properties were set as constants. All the materials defined for the simulation model are resumed in table 3.2.

Simulations were performed using the *Electric Currents* interface of the $AC\backslash DC$ module that solves a current continuity equation problem using Finite Element Method (FEM) under quasi-static assumptions [57]. Two voltage boundary conditions were set on the distal ends of the emitting electrodes with equal absolute values and opposite polarity $V_{TXi} = \pm 1.5\text{V}$, whereas two surface boundary probes were defined at the receiving electrodes. Finally, the channel attenuation was calculated as

$$A_{dB} = -20 \times \log \frac{|V_{RX1} - V_{RX2}|}{|V_{TX1} - V_{TX2}|}. \tag{3.15}$$

Moreover, we used the *Electric Circuit* interface to analyze the input impedance effect of the receiving capsule on the overall transfer function. Indeed, boundary probes were substituted with Terminal boundary conditions to connect the input shunt resistance between the electrodes. Five different values were sparsely selected for R_{rx}: 100 Ω, 200 Ω, 1 kΩ, 10 kΩ, 100 kΩ and 1 MΩ.

The last channel considered in these preliminary studies is the trans-thoracic channel that is intended to be the communication link between the LCP and the body surface (BS). This channel provides an external programmer access to data acquired and stored in pacemakers and enables remote reprogramming of the devices to adapt the therapy to the patient needs. External programmers may use patch electrodes placed on the skin surface of the body to couple the implanted devices.
Since there are no constraint about patch positioning, this study points out minimum

Biological tissues	σ S/m	ϵ_r
Blood	$[0.7005 - 1.1407]$	$[5211.3 - 154.56]$
Bone Cortical	$[0.0206 - 0.0489]$	$[281.06 - 24.917]$
Cartilage	$[0.7005 - 1.1407]$	$[5211.3 - 154.56]$
Fat	$[0.0242 - 0.0319]$	$[215.19 - 9.71]$
Heart	$[0.1895 - 0.5599]$	$[20452 - 188.17]$
Kidney	$[0.1561 - 0.5872]$	$[13225 - 227.77]$
Liver	$[0.0690 - 0.36101]$	$[12100 - 142.17]$
Inflated Lung	$[0.1768 - 0.3999]$	$[2840.4 - 107.71]$
Muscle	$[0.3497 - 0.6427]$	$[10988 - 110.62]$
Soft tissue	$[0.388 - 0.428]$	$[1000.1 - 86.37]$
Stomach	$[0.53307 - 0.8293]$	$[3880.6 - 142.56]$
Other materials		
Air	0	1
Parylene	1.16×10^{-15}	3.15
Peek	2.17×10^{-17}	3.2
Platinum	9.36×10^{6}	1
Structural Steel	4.032×10^{6}	1
Titanium	2.6×10^{6}	1

Table 3.2: Conductivity and Permittivity values used to define the interpolating curves

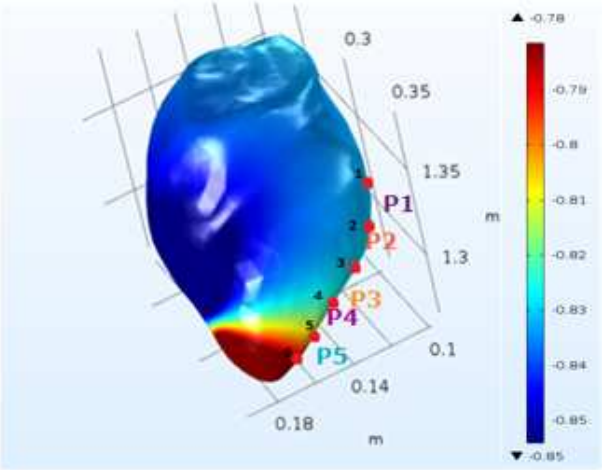

Figure 3.6: Point shaped probes placement on the left ventricle epicardial surface of the heart model. A coloured shade of the epicardium show the potential distribution of IBC signals when emitted from the RV capsule at frequency equal to 40kHz.

and maximum potential values achieved on the whole-body surface. To do so, we defined two boundary probes, selecting the entire external body surface, with probe type set respectively to *Maximum* and *Minimum*. Electrode interface impedance has not been considered in the model since its effect would be negligible at the frequencies object of this study [58].

The whole model geometry has been meshed with a custom tetrahedral meshing whose minimum element size was set to $50\mu m$ in order to adapt mesh sizes to local complexity of the model. The outer layer of the air sphere was meshed using the swept-meshing technique to accurately and efficiently mesh infinite boundary domains. The total number of mesh elements was circa 8.3 millions achieving a good average skewness quality equal to 0.653.

The frequency range of interest was set between 40 kHz and 20 MHz. The lower bound of the frequency range was selected to insure a margin with respect to electrophysiological signals, whereas the upper bound was set at the limit of the model according to quasi-static assumptions, discussed in the previous subsection.
Electrode-electrolyte interface impedance was considered negligible since we were interested in a relatively high frequencies [59]. The relative tolerance of the solution was set less or equal than 0.001. To achieve such a low relative tolerance value, a second order polynomial approximation was sufficient. As a result, the simulations lasted for 1 hour and 28 minutes using a standard workstation equipped with 32GB of RAM and .

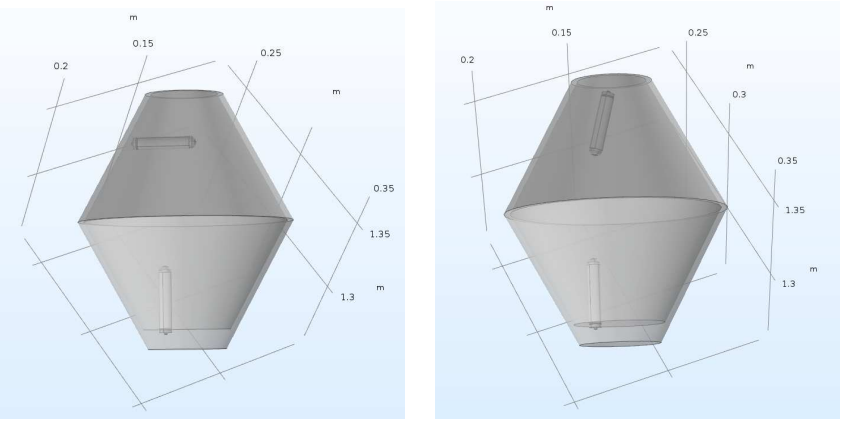

Figure 3.7: Positioning of the capsule in the right atrium showing. Parallel positioning in the left side image, whereas a perpendicular positioning is shown in right side image. The distance between the centers of the capsules is the same in both cases and equal to 9cm.

3.1.5.1 Simple geometry model

For the sake of comparison, a simple model was also constructed starting from the model proposed in [18] that is a multi-layer cylindrical model of the torso. A simple geometry heart, shown in Figure 3.7, was integrated to the original model.
It was designed as two identical double-layer truncated cones sharing the biggest circular base. The radii of the circular surfaces of the cone were respectively set to 20 mm and 55 mm to have similar size and volume with respect to the heart of the model proposed by this work. The layers of the cones were spaced apart by 3 mm to discriminate blood and heart tissue.
It is worth stating that both emitting and receiving capsules were exactly at the same position as they were placed in the accurate model. The length of the LV dipole was fixed to 1.4 cm for both the accurate model and the simple geometry one. The distance between the RV capsule and the LV dipole was set to d=5.5 cm, whereas the simplified model had a distance of d'=5.1 cm achieving a relative difference

$$\delta_d = \frac{d - d'}{d} \approx 7.3\%. \tag{3.16}$$

Electrical properties and boundary conditions were set as previously described for the accurate torso model.

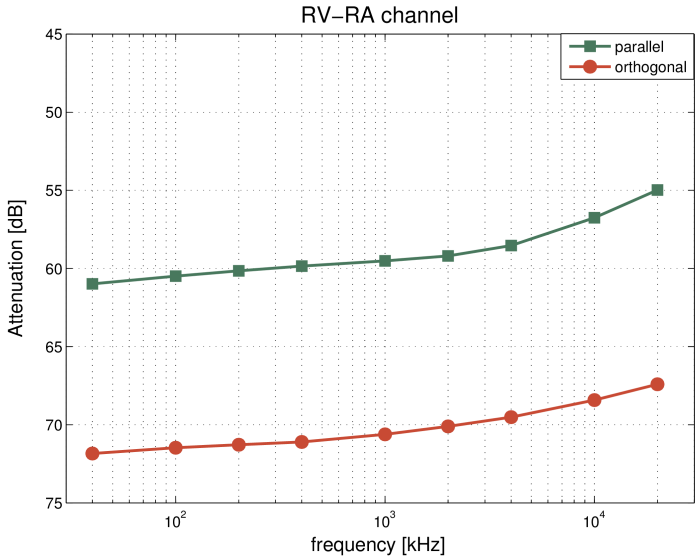

Figure 3.8: Attenuation levels of the intra-cardiac channel (RVRA) for best case (green line) and worst-case (red line) positioning of RA capsule

3.1.6 Simulation results

3.1.6.1 Intra-cardiac channel

It is well known that mutual orientation between emitter and receiver is very effective in galvanic intra-body communication [60]. However, RA capsule positioning must account for actual therapy delivery that vary among patients. Hence, it is important to characterize both best- and worst-case positioning of RA capsule.
In the best-case scenario, the electric field lines are aligned with the receiver capsule, as can be seen in Figure 3.9(right) that yields a higher differential voltage across the receiving dipole. For the same reason, the worst-case scenario would arise when capsules are orthogonal to each other Figure 3.9(left).

Intra-cardiac simulation results are shown in Figure 3.8, where the difference between worst-case and best case is ∼11 dB. In both scenarios, the attenuation decreases by ∼5 dB from 40 kHz to 20 MHz.
Mutual orientation between capsules plays an important role in the signal attenuation of galvanic IBC signals. Nevertheless, capsule synchronization must be ensured in any case. Worst and best-case conditions were identified for the intra-cardiac channel. The attenuation variability and the worst-case path loss value can be respectively used to set the minimum input dynamic range and the sensitivity of the receiver. In this way, it would be possible to demodulate data either ways.

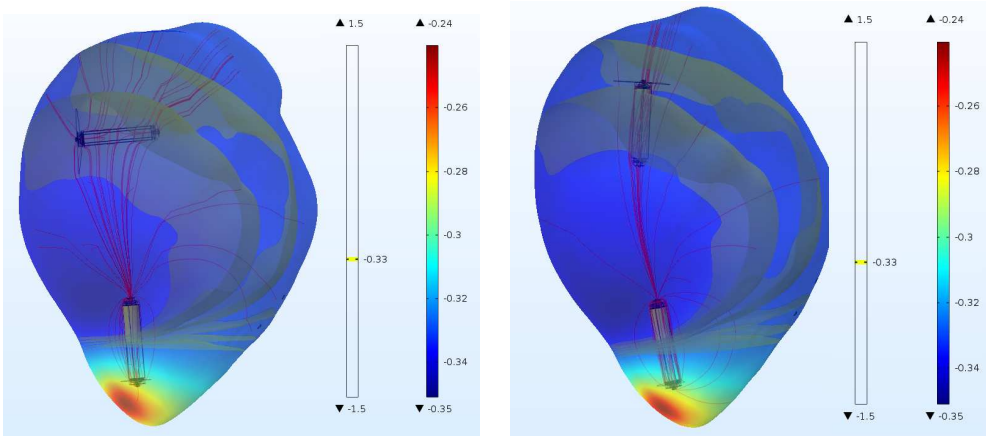

Figure 3.9: Positions of the RA capsule for the best-case (right) and worst-case (left). Electric field lines are represented in red, whereas isopotential surfaces are represented in green. 5 isopotential surfaces are plotted, where each subsequent isosurface differs of 2mV from the previous one

3.1.6.1.1 Fat Tissue effect

Fat tissue usually covers hearts with a distribution and volume that is different for every patient. In this study, we consider a floating heart not uniformly distributed that is described in [55], where most of the fat is placed on the heart surface of right chamber side. Simulation results are shown in Figure 3.10 where attenuation levels are lowered of almost 4dB for the whole range of study. The reason is that the conductivity of the fat is almost ten times lower than the conductivity of the heart tissue. Indeed, the fat tissue forms an isolation layer for the intra-cardiac channel increasing the voltage level experienced across the receiving capsule.
To reduce model complexity and consider a worst-case scenario, the fat tissue layer was ousted from the simulation model.

3.1.6.1.2 Intra-cardiac channel directivity

Human body is inhomogeneous, anisotropic and asymmetric. Nevertheless, since COMSOL models the channels using linear and passive elements, the reciprocity should be respected in case the same capsule is used for the emitter and the receiver [61]. In other words, the voltage drop across the capsule in the RA due to the voltage generated in the RV should be equal to the voltage drop across the capsule in the RV due to the voltage imposed in the RA. To verify that levels are comparable inverting the signal propagation, two additional simulations were performed.
The results are shown in Figure 3.12, results are very similar due to the fact that capsule are of the same size resulting in similar impedance across the electrodes due to the tissue. A small difference of less than 3 dB caused probably by simulation error

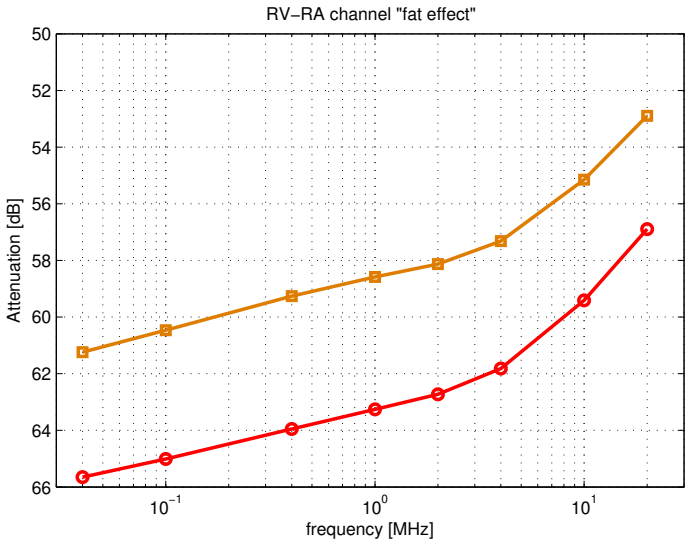

Figure 3.10: Fat effect on intra-cardiac channel for IBC

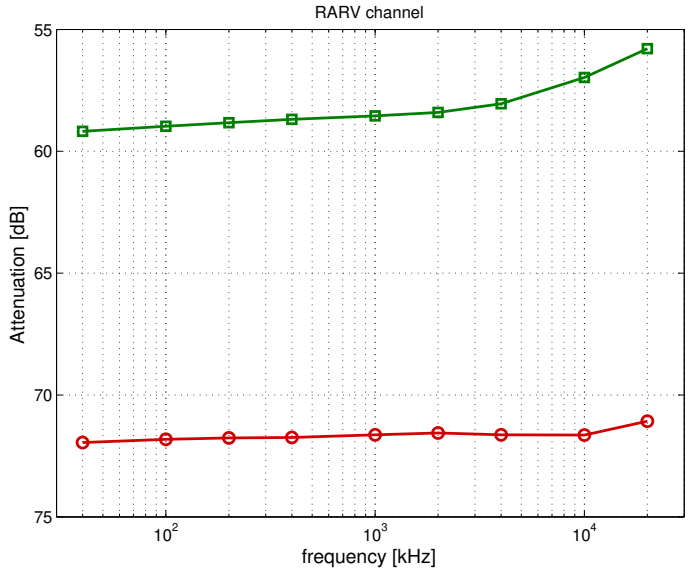

Figure 3.11: Attenuation levels of the intra-cardiac channel (RARV) for best case (green line) and worst-case (red line) positioning of RA capsule

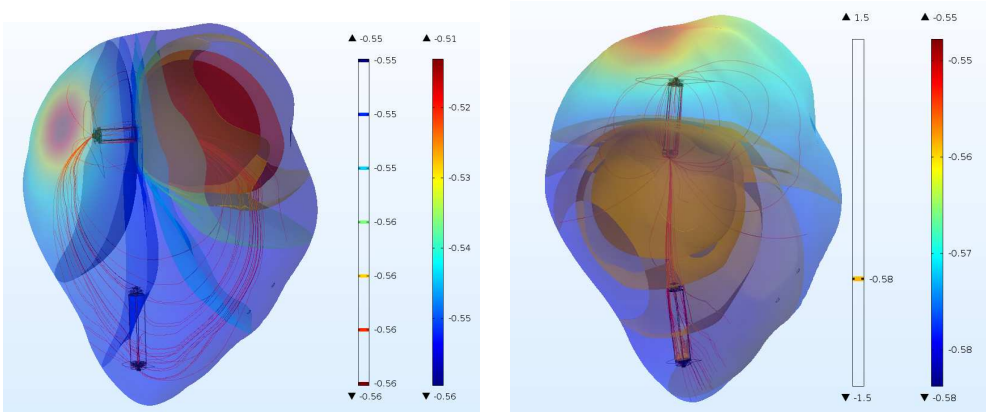

Figure 3.12: Positions of the RA capsule for the best-case (right) and worst-case (left). Electric field lines are represented in red. 5 isopotential surfaces are plotted, where each subsequent isosurface differs of 2mV from the previous one

was obtained compared to the previous case. Thanks to this result, we can easily use the same circuitry for either way of the communication lowering the complexity of the system design.

3.1.6.2 Inter-Ventricular channel

The inter-ventricular channel can be used for leadless CRT systems, where the stimulation in the RV and in the LV must be synchronized to increase the ejection fraction of the heart. The results of inter-ventricular channel attenuation are plotted in Figure 3.13. The best results are achieved when the probes are placed closer to the apex because the distance to the emitter capsule is shorter. However, the position of the LV device must be chosen to maximize the ejection fraction of the heart [62, 63, 64] and depends on various patient factors [65].
Inter-Ventricular channels show lower attenuation levels at high frequencies since the conductivity of body tissues increases with frequency [45] that makes currents better propagate at higher distances. In a more orthodox way, we can say that the amplitude of electric waves follows an exponential decay with respect to distance, whose intensity depends on the conductivity of the medium. Since the conductivity of the biological tissue increases with frequency, a lower relative attenuation is experienced at high frequencies. Long distance probes have a higher relative benefit of working at high frequencies compared to short distance ones, where the gap between best case (20 MHz) and worst-case (40 kHz) decreases from 17 dB to only 7.4 dB. As a result, the link margin of the inter-ventricular communication can be reduced at high frequencies.

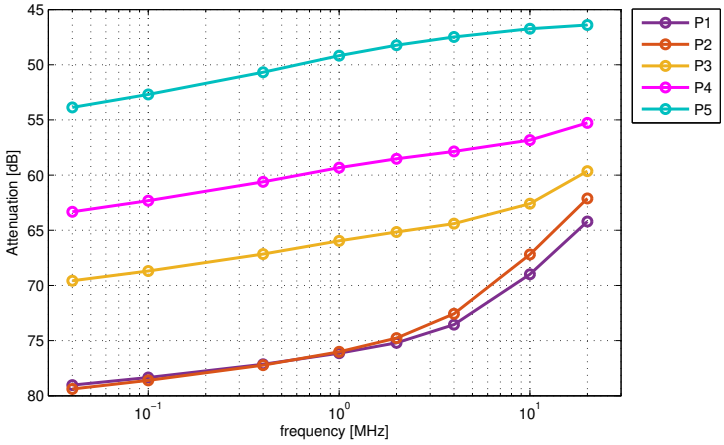

Figure 3.13: Attenuation levels of 5 epicardial probes set on the left ventricle: P1 (d=7.7cm), P2(d=7.2cm), P3(d=6.0cm), P4(d=4.9cm), P5(d=3.8cm)

3.1.6.3 Trans-thoracic channel

This is the last channel we will consider and it is essential for all LCP applications from single VVI Leadless pacemaker to the most complex multi-node LCP system. Indeed, it is used to program the device and retrieve information during the follow-ups with the physician. The external programmer can use patch electrodes to electrically couple with the implant devices. Less geometrical constraints are involved with trans-thoracic channel since the whole torso surface is reachable for the placement of the electrodes.
Figure 3.14 shows body surface potential polarities suggesting the optimal position of patch electrodes. One electrode should be placed on the mid-clavicular line of the fifth inter-costal space and the second electrode at the medial end of the fourth inter-costal space. This configuration allows to maximize the attenuation level for signals coming from right chambers of the heart since it minimizes the distance between the electrodes and the RV device. Moreover, the orientation of the patch electrodes is parallel to the RV apex minimizing channel losses for the RV.
The results can be seen in Figure 3.15, where the blue line represents the attenuation for the channel from the RV capsule toward the body surface, whereas the red and green lines represent the attenuation from the RA capsule respectively in the best-case and the worst-case scenario of the intra-cardiac communication. It is clear that the signals coming from the RV capsule are less attenuated by the media with values ranging between 37.4 dB and 41.5 dB. The low attenuation values are owing to the relatively short distance of $\sim$4 cm between the RV capsule and the body surface, as well as the large inter-electrode distance of the body surface probes, which is $\sim$7 cm.
For the RA capsule, attenuation results range between 50 dB and 45 dB and show an optimal value at 4 MHz allowing to have the same amplitude values for both RA

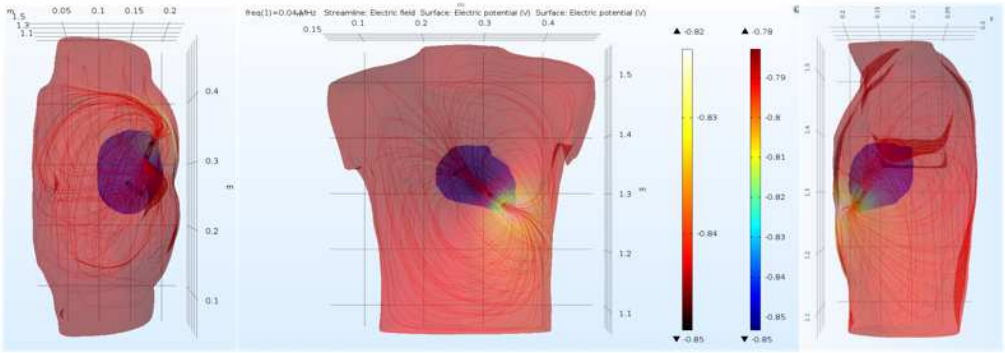

Figure 3.14: Graphical representation of simulation results for frequency equal to 40kHz, where both epicardial (rainbow color table) and body (thermal color table) surface potentials are represented. Electric field line distribution is shown in red.

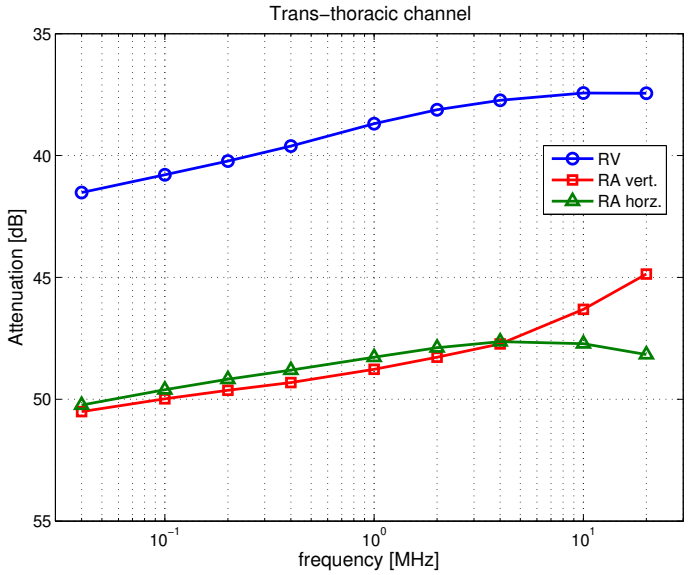

Figure 3.15: Attenuation levels of trans-thoracic channel having distance between RV distal electrode and the body surface equal to 3.52cm

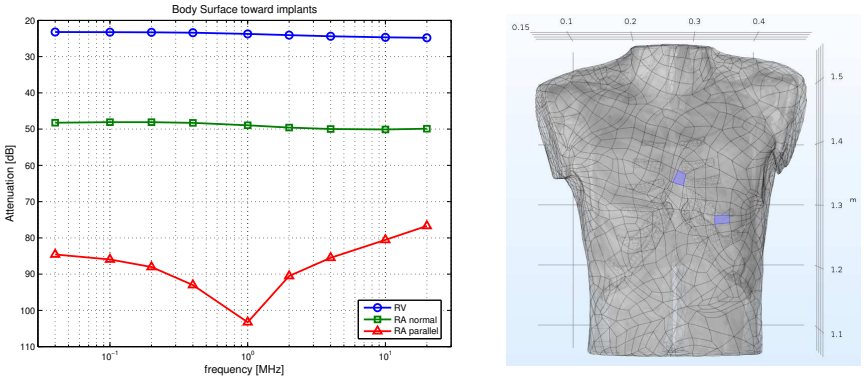

Figure 3.16: Trans-thoracic channel for out-in Intra Body Communication. On the left hand side the results using the emitter having inter-electrode distance equal to 7 cm. On the right hand side the placement of the Dirichlet boundary condition used to emulate patch electrodes on the body surface.

capsule positioning. The reason of the different path loss is that the distance between body surface electrodes and the RA capsule is bigger than the one concerning the RV capsule, due to the anatomic orientation of the heart, and it is approximately equal to 5 cm.
The Trans-thoracic channel experiences lower attenuation levels with respect to intra-cardiac and inter-ventricular channels. The reason is that surface electrode have an inter-electrode distance that is more than twice the capsule length and can be optimally placed on the body surface to maximize the differential voltage across the receiver dipole. Moreover, the RV capsule used to emit IBC signals is not far from body surface whose length is comparable with probe P1 of the inter-ventricular channel.

3.1.6.3.1 Directivity of Trans-thoracic channel

So far, in this subsection, we have discussed about the attenuation levels for the trans-thoracic channel from the implant devices toward the body surface. However, the trans-thoracic communication must be bidirectional and it is worth to see how the attenuation levels change with the direction of the propagation of IBC signals.
To do so, two Dirichlet's conditions were imposed on the outer surface of the accurate torso model to emulate patch electrodes. The surface boundary conditions were directly applied on model patches with surface area of circa 3 cm^2 that is similar in size to standard patch electrodes used for medical usage [66]. The cathode was fixed on the mid-clavicular line of the fifth inter-costal space to minimize the distance from the RV capsule, whereas the anode was placed in a parasternal position at the 4th costal cartilage to minimize the distance from the RA capsule.
The positioning of the patches are pointed out in Figure 3.16 where the inter-electrode distance was of 7 cm. The results of this particular setup are shown in Figure 3.16

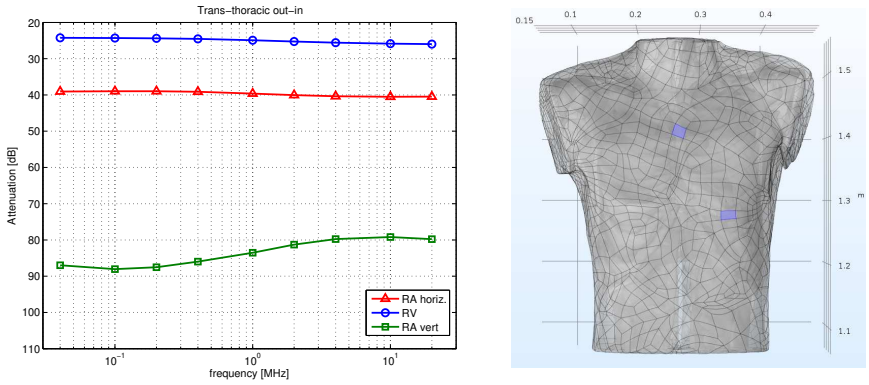

Figure 3.17: Trans-thoracic channel for out-in Intra Body Communication. On the left hand side the results using the emitter having inter-electrode distance equal to 12.5 cm. On the right hand side the placement of the Dirichlet boundary condition used to emulate patch electrodes on the body surface.

where the best attenuation levels are experienced for the communication channel with the RV capsule reaching values of almost 25 dB over the whole frequency of interest. The orientation strongly impacts trans-thoracic channel as can be seen from the difference of the attenuation levels for the RA capsule fixed on the free wall in parallel or normally to heart apex. In particular, RA values increase of almost 30 dB with peak of 52 dB reaching levels that would make the communication extremely difficult and power inefficient. To improve RA channel, the cathode has been moved at the first inter-costal to cover the whole heart reaching an inter-electrode distance of 12.5 cm.
The positioning of this particular case and the respective results are shown in Figure 3.17, where the attenuation levels for the RV capsule do not significantly change compared to the previous case; whereas the RA capsule experienced a lower attenuation that was equal to 40 dB for the best-case. For this second placement of the patch electrodes, there is a significant difference between worst- and best-case for the RA positioning with gap values that ranges from 50 dB to 40 dB.

3.1.6.4 Comparison with simple geometry model

For the author best knowledge, there are no IBC numerical studies for implant devices applications published in the literature. To highlight the importance of the geometry of the model, a simple geometry model [18] was built as described in Sec. 3.1.5. Comparison results of inter-ventricular and intra-cardiac channels are shown in Figure 3.18, where the dashed red lines represent the results of the simple geometry model and the green lines represent the simulation results of the accurate model.
The maximum absolute difference Δ_{max} between the results of the models reaches 14.6 dB and 9 dB for the inter-ventricular and the intra-cardiac channels respectively.

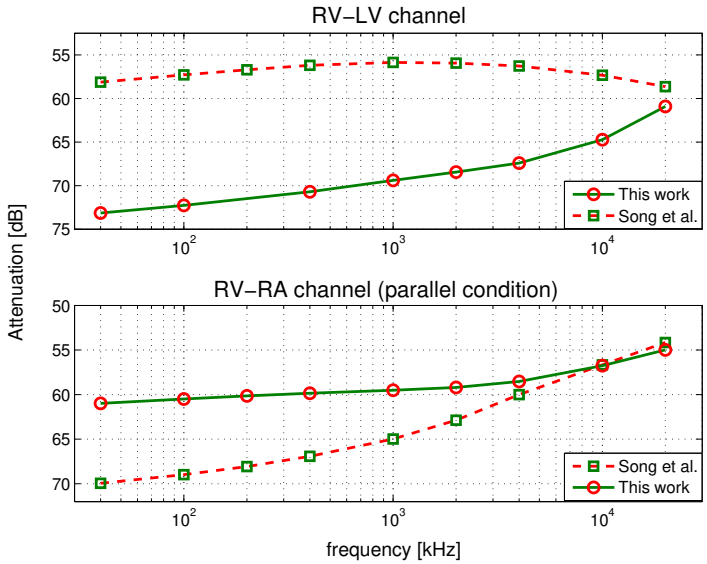

Figure 3.18: Attenuation comparison of the inter-ventricular (top) and intra-cardiac (bottom) channels between simulations performed with the simple geometry model (dashed line) and the accurate model (solid line) proposed in this work.

Such a big difference can be misleading when designing optimized transceivers, leading to wrong frequency and input dynamics selection. It is worth noting that simple geometries models can mislead to a wrong frequency choice according to the lowest attenuation. It was shown that keeping the same positioning of the devices and the same volume of the heart for the accurate and the simple geometry models led to different results in terms of both attenuation and frequency trend.

3.1.6.5 Input resistance effect

Previous Results were obtained considering receiving electrodes as separate entities to characterize the channels individually. Note that the input resistance R_{rx} of the receiving capsule can modify the channel attenuation.
As shown in Figure 3.19, the channel attenuation strongly depends on input receiver resistance for levels below 10 kΩ since low resistance levels are comparable with tissue impedance values reducing the equivalent resistance seen across the electrodes. For the sake of brevity, only the best-case scenario of the intra-cardiac channel was considered in this analysis, but the same principle can be extended to all the channels.
The study shows the importance of the choice of the input impedance for the receiver capsule. The effect of the input resistance is clearly visible on the whole frequency range of interest, but it is not constant with respect to frequency. At 40 kHz the gap between $R_{rx} = 100\ \Omega$ and $R_{rx} = 10\ \text{k}\Omega$ is ∼21 dB, whereas at 20 MHz the gap decreases ∼14 dB.

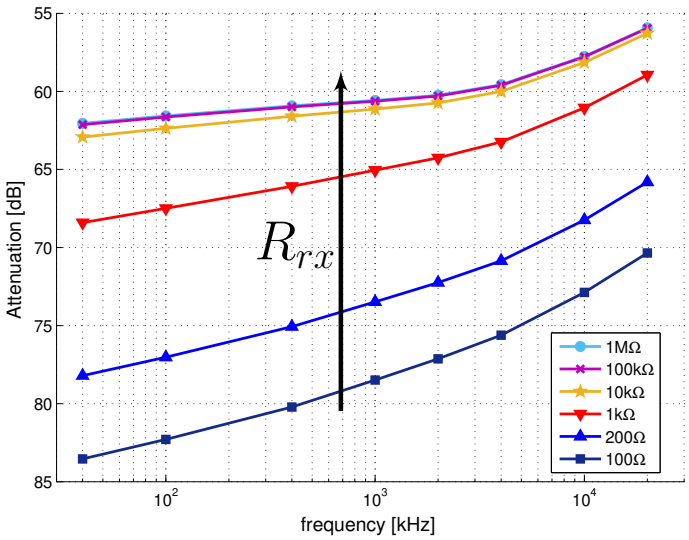

Figure 3.19: Results of parametric simulation with respect to receiving input resistance for the intra-cardiac channel.

The reason is that to higher frequencies correspond lower inter-electrode impedances, reducing the effect of the voltage divider at the receiver side.

3.2 Measurements

3.2.1 inter-electrode impedance measurements

The simulation model proposed in previous chapter can give an accurate representation of macroscopic effects of body tissues and discrete components that are embedded in the devices. The simulation model does not consider polarization impedance that arise at the interface between the electrodes and the ionic conductor.
The overall inter-electrode impedance Z_e can be represented by (3.17) and modeled as the circuit shown in Figure 3.20.

$$Z_e = Z_b + A(j\omega)^{-n} = Z_b + A\omega^{-n}\left(\cos\frac{n\pi}{2} - j\sin\frac{n\pi}{2}\right), \tag{3.17}$$

the first term Z_b represents the bulk impedance of the ionic conductor, whereas the second term $A(j\omega)^{-n}$ represents the polarization impedance with A and n constants and $0 < n < 1$ [67]. As can be seen, this impedance strongly decreases with frequency. However, to be sure that no remarkable errors were introduced to the simulation model due to polarization impedance, the inter-electrode impedance of measurement prototypes were measured.

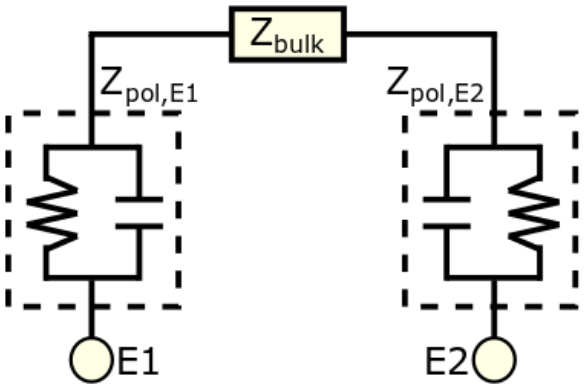

Figure 3.20: Overall inter-electrode impedance. $Z_{pol,Ei}$ represents the polarization impedance of the electrode i, whereas the bulk impedance Z_{bulk} represents the opposition of the electrolyte to ionic conduction.

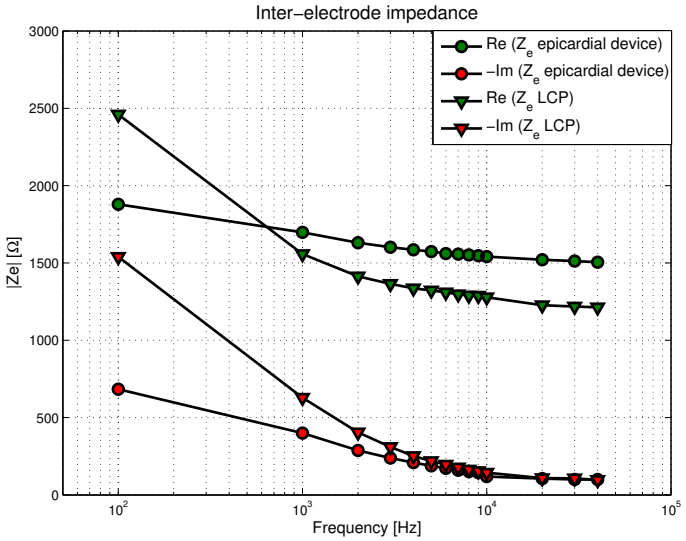

Figure 3.21: Measurement results of the inter-electrode impedance of the measurement devices in the frequency range [100 - 40k]Hz. Endocardial capsule prototype is represented by triangular markers, whereas Epicardial device by circular ones.

The prototypes were immersed in a saline solution with normality N=0.35 eq/l and the *3260B Precision Magnetics Analyzer* was used to measure the overall inter-electrode impedance Z_e. Using (3.17), it was possible to retrieve both real and imaginary part of Z_e. Figure 3.21 shows the imaginary (red) and the real (green) part of Z_e for both devices, where circular markers represent the values of the epicardial capsule and triangular markers represent the values of the LCP capsule. In both cases, an asymptotic behavior of Z_e was observed and no significant differences were detected for frequencies

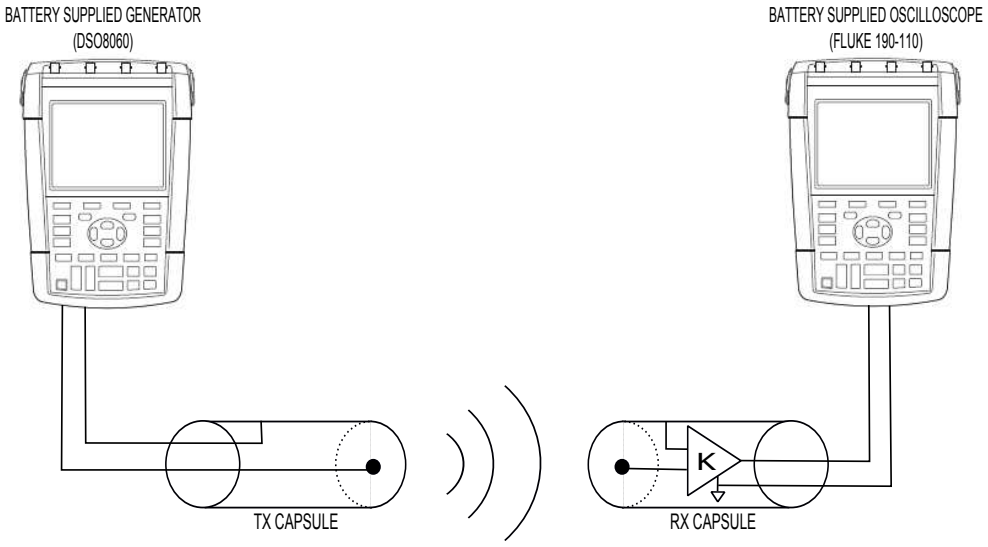

Figure 3.22: Measurement setup used for galvanic IBC measurements

higher than 10 kHz. This indicates that for relatively high frequencies the inter-electrode impedance reduces to the bulk impedance of the ionic conductor. This result is consistent with previous studies [20], where no attenuation effects were reported from polarization impedance.

3.2.2 Measurement setup

Galvanic signal measurements are not straightforward due to low amplitude levels and grounding effects that can be misleading for standard measurement devices. When prototyping measurement systems for galvanic IBC signals, one must pay attention to ground loops and cable coupling that may lead to completely incorrect results. To reduce ground loops, the common procedure is to use battery-supplied devices, even though, a capacitive coupling of measurement devices with ground can arise at high frequencies. In [21], several measurement setups have been compared, showing the importance of making use of battery supplied devices for galvanic measurements to reduce grounding effects.

In this work, a completely floating measurement system was set up using *DSO8060 Hantek* as waveform generator and *Fluke 190-110* as oscilloscope to acquire receiving voltage data. The oscilloscope was connected to a battery supplied laptop using the software *Flukeview* to acquire and store signal measurements as time varying vectors. To verify that there were not other contribution superposing to the useful signal leading to wrong measurements, a spectral analysis was performed before signal acquisitions using *Discovery 2™* from *Digilent©*, which is an Analog Digital Converter having a sampling frequency of 100 MHz.

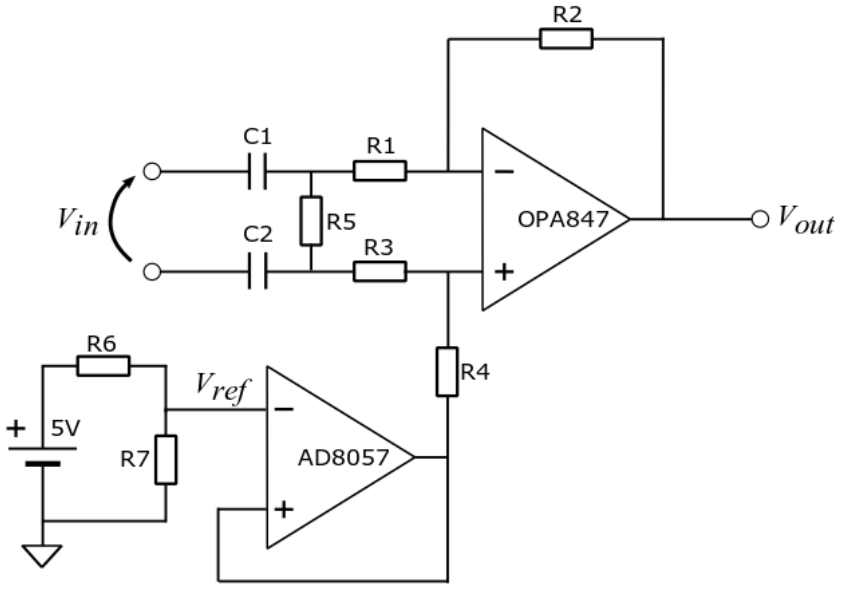

Figure 3.23: Schematic of the differential amplifier integrated in the capsule, where C1=C2=200nF, R1=R3=100Ω, R2=R4=6.8kΩ, R5=100Ω, R6=100Ω and R7=100Ω.

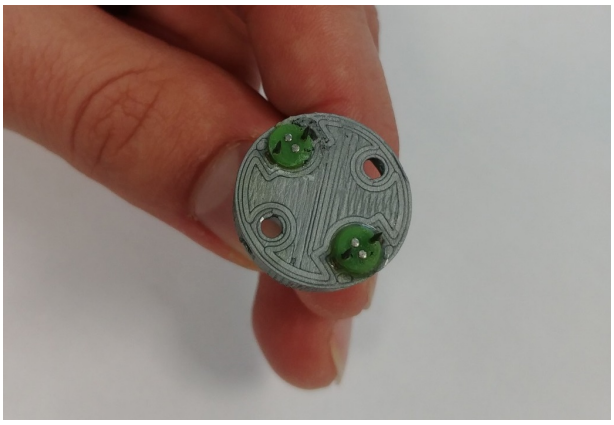

Figure 3.24: Epicardial capsule used for in vivo experiments.

Both devices were connected to the capsule prototypes by means of coaxial cables that were internally laser welded passing through a drilled hole at the distal part of the capsules. A differential amplifier with a gain of 36 dB, bandwidth of [20 kHz - 60 MHz] and input resistance $R_{in} = 100\ \Omega$ was designed and embedded in the receiver capsule to emphasize the local measurement and adapt amplitude levels to oscilloscope resolution. The differential amplifier was intended to be used only for measurements and no power optimization was assessed. Indeed, the receiver capsule was externally powered by a

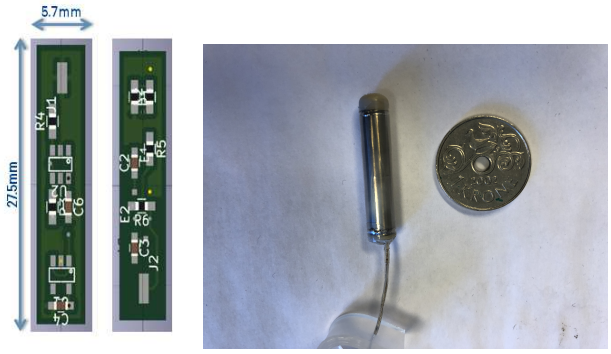

Figure 3.25: Leadless capsule rototype for in vivo measurement. On the right the printed circuit board for the integration of the differential amplifier.

5-volt battery to keep the system galvanically isolated from the ground. The circuit of the differential amplifier is shown in Figure 3.23, omitting power supply lines and the bypass capacitors that were connected as suggested by manufacturer in the datasheets to minimize power supply noise contribution.
Ultra-low noise operational amplifiers were used for both the amplifying stage (OPA847) and the voltage reference buffer (AD8057). OPA847 has a common mode rejection ratio CMRR_{OA} of 110 dB. To keep a high CMRR for the differential amplifier, resistors with tolerance $\sigma = 0.05\%$ were used achieving an overall $\text{CMRR}_D \sim 90dB$ [68]. A voltage reference of 1.5 V was made by means of a resistive voltage divider from the supply voltage achieving an output dynamic of 3 volts allowing to measure input signals upto 9 mV that was more than 7 times higher than the maximum expected input signal level. For the intra-ventricular channel verification, 2 couples of epicardial electrodes spaced by 1.4 cm were embedded on a 3D-printed epicardial support, having anchoring needles and suture holes to properly fix at the heart (Figure 3.24). Both electrode couples had diameters of 1 mm and distance of 2 mm, electrodes of the same couple were short circuited and connected to a coaxial cable.

Hospitals are noisy environments; thus, the acquired signals require to be filtered out to keep only the frequency of the useful signal. Filter design toolbox of MATLAB 2014 was used to design very narrow filters around each frequency of interest. In particular, Chebyshev FIR-filters were designed according to the sample rate of each acquired signal. The qualitative difference between the acquired signal and the filtered signal is clearly shown in Fig.3.26. Finally, peak to peak levels were retrieved by inspection and used to estimate the attenuation levels for intra-cardiac IBC communication using (3.18).

$$A_{dB} = -20 \times \log \frac{V_{RX,pp}}{V_{TX,pp}} + G_{RX}, \tag{3.18}$$

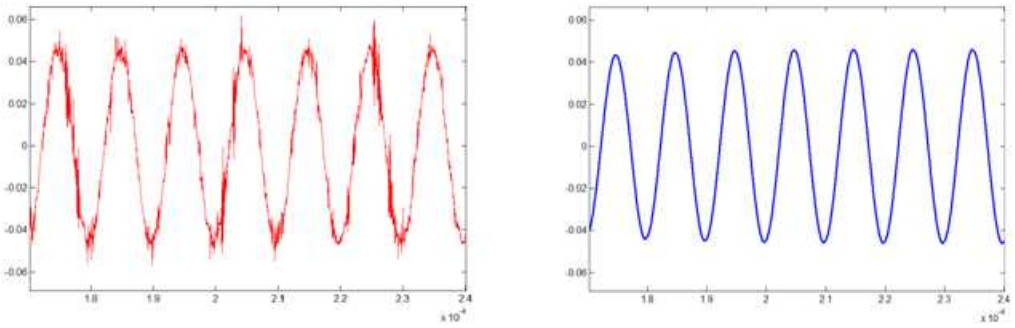

Figure 3.26: Comparison between sampled and processed signals.

Table 3.3: Liquid phantom characteristics

f	40kHz	100kHz	200kHz	400kHz	1MHz	2MHz	4MHz	10MHz	20MHz
σ [S/m]	0,1895	0,2151	0,2382	0,2685	0,3275	0,3809	0,4323	0,5013	0,5599
N [eq/L]	0,0183	0,0208	0,2304	0,0260	0,0318	0,0370	0,0420	0,0488	0,0545
m [m]	42,8	48,6	53,9	60,8	74,3	86,5	98,2	114,1	127,6

where $V_{RX,pp}$ is the peak to peak voltage of the filtered received signal, $V_{TX,pp}$ is the peak to peak voltage of the emitted signal and G_{RX} is the gain of the receiver amplifier in dB. Capsule hermeticity was ensured in order to use the measurement setup for both in vitro and in vivo measurements whose results are discussed in Section 3.2.4.

3.2.3 In vitro verification

3.2.3.1 Phantom description

The measurement setup has been tested in a custom liquid phantom based on a salt solution that reproduces conductivity of the heart from 40 kHz to 20 MHz. The phantom was made of deionized water and sodium chloride, whose concentration was modified for each frequency of interest. According to Gadani's studies, the ionic conductivity σ for NaCl solution at room temperature ($25°C$) can be calculated using (3.19), where N is the normality of the solution [69].

$$\sigma_{\mathrm{NaCl}}(25, N) = N[10.394 - 2.3776N + 0.68258N^2 - 0.13538N^3 + 1.0086\times10^{-2}N^4] \quad (3.19)$$

Phantom consisted of a water volume was 40 liters contained in a tank as shown in Figure 3.27, whose dimensions were 50 cm x 36 cm x 26 cm to reduce board effects that smaller phantoms may introduce. The concentrations of the phantom solution both in terms of normality N and mass m of NaCl are reported in Table 3.3. The mass of the solute was retrieved for 40 liters of solvent from the definition of Normality, described in (3.20), knowing the equivalent weight of the NaCl molecule.

$$N = \frac{m_{solute}}{eq.mass \times Vol._{solvent}} \rightarrow m = N \times eq.mass \times Vol._{solvent} \quad (3.20)$$

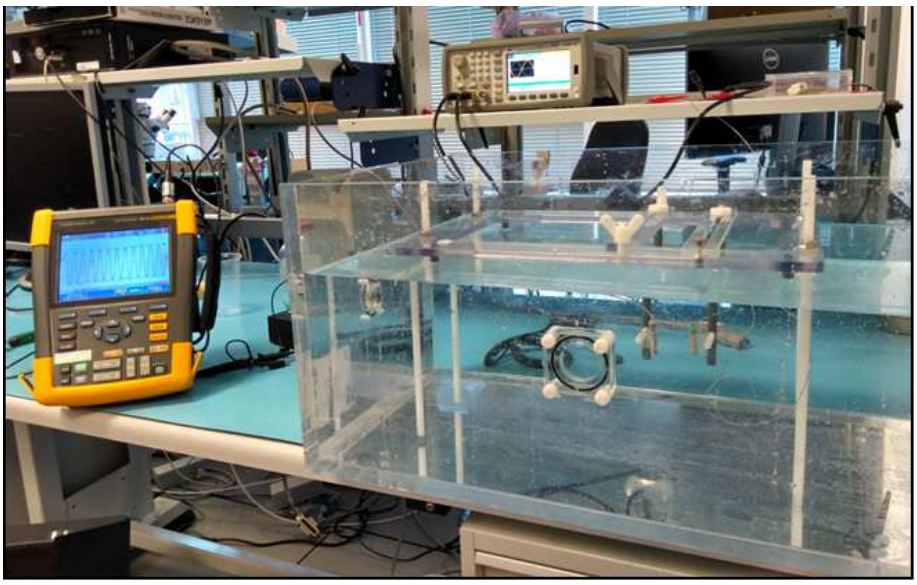

Figure 3.27: Custom phantom used for preliminary verification. Dimension of the tank were 50 cm x 36 cm x 26 cm containing 40 l of solution.

Emitter and receiver capsules were set at a distance of 3 cm between their respective medium points in parallel orientation to maximize sensed voltages.
The phantom has been reproduced and simulated in COMSOL Multiphysics in order to verify the reliability of the measurement setup. The input resistance of the receiving capsule R_{rx} has been added to the model using the *Electrical Circuit* module as previously described in Section 3.1.5.

3.2.3.2 Verification result

In vitro measurements were performed to verify the reliability of the measurement setup. Figure 3.29 compares measured attenuation levels of parallel capsules with channel length distance set equal to 3 cm with simulated results. The measurement values are in the range of [67.5-57]dB with maximum absolute error Δ_{max} of 3 dB with respect to simulations, which is 15 dB lower than phantom measurement proposed for body surface galvanic IBC [21]. Those measurements were performed in a homogeneous medium and cannot replicate in vivo measurements accurately. In a real case scenario, signals might benefit of border effects that will arise from the shape of the heart and due to the different properties of contact tissue of each electrode pair.

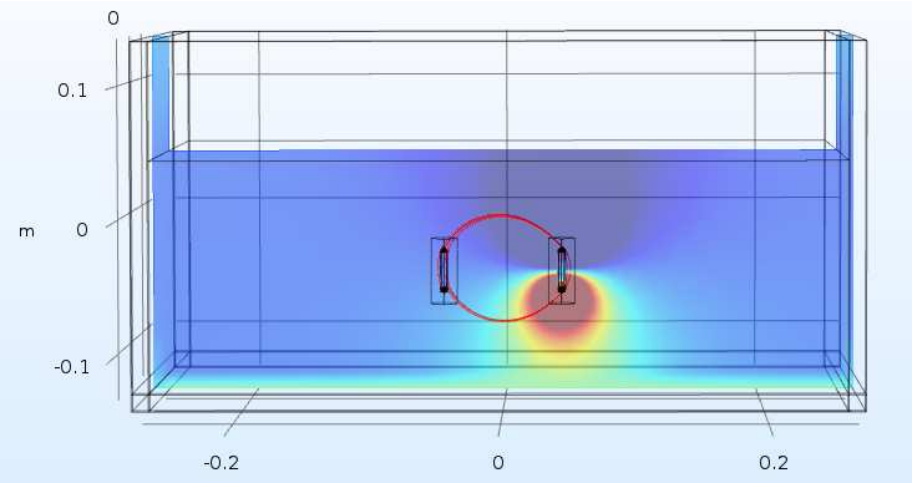

Figure 3.28: Reproduction of the phantom used for preliminary verification in COMSOL environment.

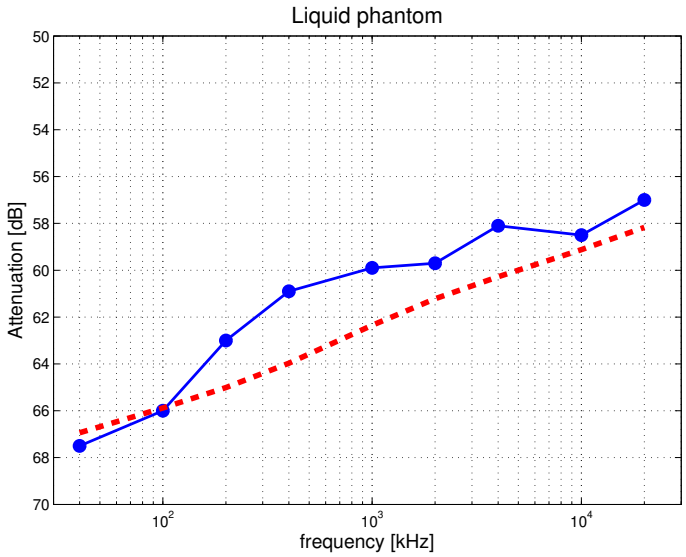

Figure 3.29: Verification results of in vitro measurements. Both measurement (blue solid line) and simulation (red dashed line) were performed in parallel orientation and channel length of 3cm.

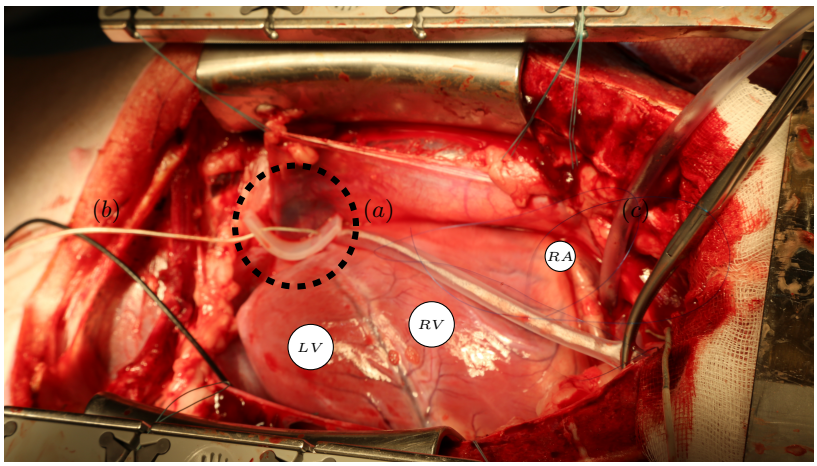

Figure 3.30: View of the access to the heart during in vivo measurements. (a) Silicon slice for anchoring RV apex. (b) Coaxial cables of RV capsule (white) and LV epicardial patch (black). (c) Forceps to secure suture stitches.

3.2.4 in vivo verification

3.2.4.1 Methodology

Three in vivo experiments were performed, one at Institut Mutualiste Montsouris Research (IMMR) and two in the Intervention Center at Oslo University Hospital. To emulate an environment comparable to human body, we used living pigs whose weight varied from 70 kg to 80 kg.

The appropriate anesthesia and pain medication were controlled by experienced professionals throughout the experiment ensuring animal welfare compliant with the local ethical standards and the Helsinki declaration on animal use in biomedical research [43]. The pig was delivered from an approved supplier to the research animal facility at the hospital two days before the experiment. As premedication on the day of the experiment, the pig received an intramuscular injection of Ketalar 20 mg/kg, Azaperone 3 mg/kg and Atropine 0.02 mg/kg. A 100-cm long infusion tube was used so the animal could move freely while premedication is injected.

After the animal has fallen asleep, venous cannula was attached to its ear vein, which allows easily replenishment of thiopental 50 mg/ml, if necessary, during transport to the operating room. When the pig arrived at the operation room, tracheostomy was made, and anesthesia was maintained with inhalation gas (isoflurane 2.1%) and morphine from 0.15 to 0.2 mg/kg/h, adjusted for pig autonomous stress response. Standard anesthesia monitoring was used, including ECG, SpO2, invasive blood pressure, temperature and diuresis.

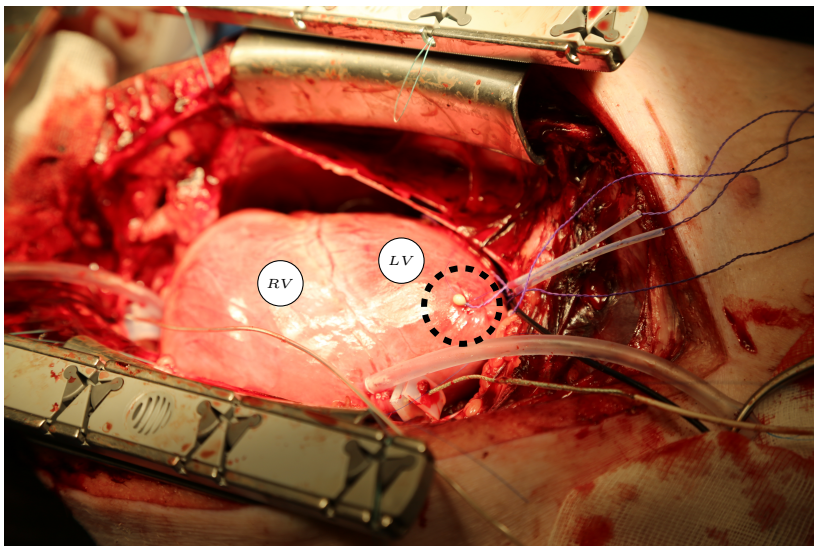

Figure 3.31: View of the access to the heart for the placement of the sonometric crystals

To correlate the IBC signal strength with the left ventricle (LV) hemodynamics, we continuously measured the LV volume using four sonometric crystals. The crystals were sutured on the LV epicardium, as shown in Figure 3.31. Two crystals were sutured on mid-posterior and mid-anterior locations of the LV and the distance between them was continuously measured, corresponding to the short-axis of the LV. The long-axis was measured as the distance between one crystal on the apex and one on a basal lateral locations. Assuming the LV to have a half ellipsoid shape, the LV volume was estimated as

$$V = \frac{2\pi \times a \times b^2}{3}, \tag{3.21}$$

where a is the long-axis and b is the short-axis. The receiver capsule was implanted in the RA by puncturing the right atrium. The puncture was closed using a snare suture technique, which involved suturing 4-5 stitches around the puncture site, passing the two stitching ends through a shaft using a snare, and pulling the stitch ends from the distal end of the shaft and secure them with forceps as can be seen in Figure 3.30.
This method allowed us to easily extract and replace the capsule by loosening the stitch ends through the shaft. A piece of silicon (Figure 3.30 a) was used to apply a small mechanical tension between the distal end of the capsule and the heart muscle to maintain contact between the capsule and the endocardium.
The emitter capsule was implanted in the right ventricle (RV) through a puncture on the RV apex in the same way as the RA capsule.
A 3D-printed device with a diameter of 1.7 cm, width of 0.5 cm, and two electrodes of 1 mm radius separated by 1.4 cm was implanted on the epicardium of the left ven-

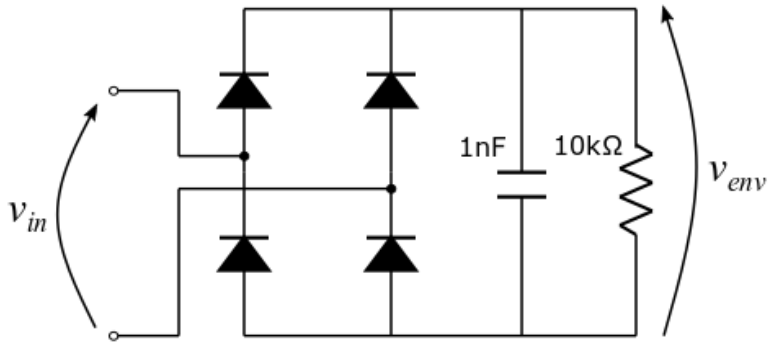

Figure 3.32: Full bridge rectifier used to retrieve the envelope of the IBC signal

tricle. The epicardial capsule was placed on the LV lateral free wall about 5 cm from the apex. The capsule was sutured to the LV epicardium and connected to a differential amplifier with the same characteristics of the one embedded in the RX capsule. Implanted capsules were connected to the measurement devices as previously described in Section 3.2.2. Nine different frequencies of the spectrum of interest were assessed: 40 kHz, 100 kHz, 200 kHz, 400 kHz, 1 MHz, 2 MHz, 4 MHz, 10 MHz and 20 MHz.

The heart is a moving environment. As such, it makes the effective channel length change during a whole heart cycle. To characterize the effect of the heart movement, a 3-minute long time acquisition has also been performed for a signal frequency of 500 kHz. To do so, we substituted the oscilloscope with PowerLab© 16/35 (AD Instruments), which is an Analog Digital Converter (ADC). Since the maximum sampling frequency of the ADC was limited, we rectified the receiver capsule output through a full-bridge rectifier to retrieve the amplitude envelope of the IBC signal. The full-bridge rectifier was composed of low voltage fast switching diodes (BAT54 Vishay©). A second battery supplied amplifier having a gain of 35.2 dB, input resistance of 1 MΩ, and output swing of 12 V was interposed between the capsule output and the rectifier to increase the amplitude of the IBC signal improving the resolution of the digital acquisition. The continuous LV volume, a 3-lead ECG, and the envelope signal were connected to Powerlab© for the analysis.
After the experiment, according to the Helsinki declaration, the animal was humanely euthanized by intravenously injecting 1 g pentobarbital and 100 mg morphine followed by 100 mmol of KCl.
The long time acquisition of the envelope signal was digitally filtered using LabChart©:

- Low pass filter with a cutoff frequency of 20Hz to limit the spectral range to physiological activities
- Low pass filter of 0,7 Hz to point out the respiration effect on the signal attenuation

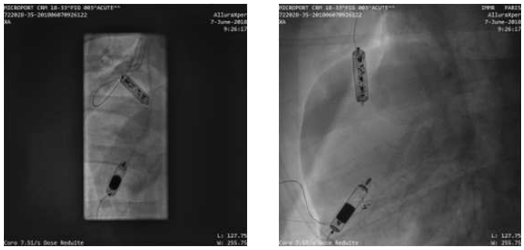

Figure 3.33: X-Ray images of worst-case (left) and best case (right) positioning during in vivo experiment

3.2.4.2 Results

Intra-cardiac results are plotted in Figure 3.34, where best- and worst-case simulations are represented by the two dashed lines. The results of the measurement performed at IMMR are plotted in yellow and orange and their positioning are reported in the X-ray images in Figure 3.33. The yellow line represents orthogonal positioning (worst-case) and the orange line the parallel positioning (best-case). The measurements performed at Oslo University Hospital are reported by the blue and green lines. Both were performed fixing the RA capsule as parallel as possible to the RV capsule.
Attenuation levels of measurement results varied between 90.6 dB and 69 dB with the different positioning and frequencies. High frequencies show lower attenuation levels - a trend verified by the simulations. In fact, most of the measurement results lie in the region bounded by the best- and the worst-case simulation curves.
Inter-ventricular results are plotted in Figure 3.35 where the dashed red line represents the simulated results and the blue line represents the in vivo measurements. The results show a monotonic increase of received voltage values with a difference of around 10 dB between the lowest frequency (40 kHz) and the highest frequency (20 MHz).
Measurement and simulated results are highly comparable fluctuating by only around 3 dB at 20 MHz. In vivo results follow the same trend of simulations confirming the reliability of the torso model for the estimation of the attenuation.

The heart cycle that experiences the highest amplitude swing of the envelope signal is reported in Figure 3.36, where the ECG signal is represented to have a time reference of the heart cycle. It was found that the maximum relative difference of the envelope amplitude signal over the whole acquisition time was about 5.3 dB. The best timing for the intracardiac channel communication occurs at the end of the repolarization phase, whereas the worst attenuation values results were experienced after the depolarization of the ventricles (QRS complex). This can be explained from the change of the heart volume during the heart cycle. As you can see from Figure 3.37, the amplitude of the envelop signal increases as the heart volume decreases.
The highest amplitude swing were experienced during inflation period, whereas the low-

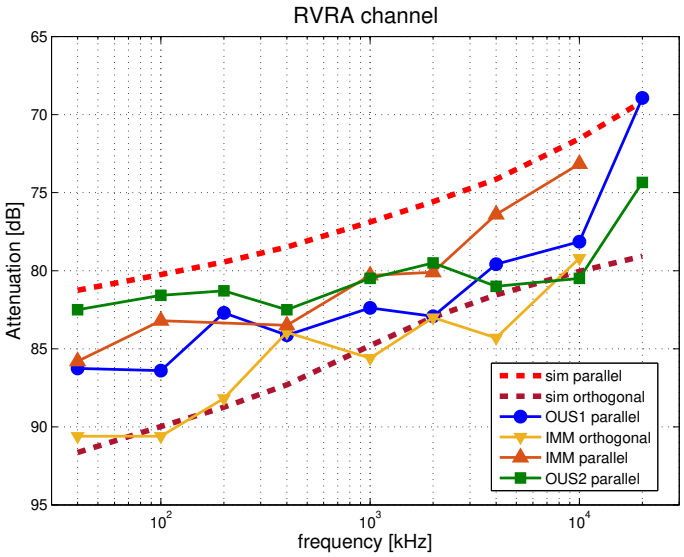

Figure 3.34: Measurement results of in vivo experiments for the intra-cardiac channel, where solid lines represent in vivo trials, whereas dashed line represent simulations for both best-case and worst-case positioning.

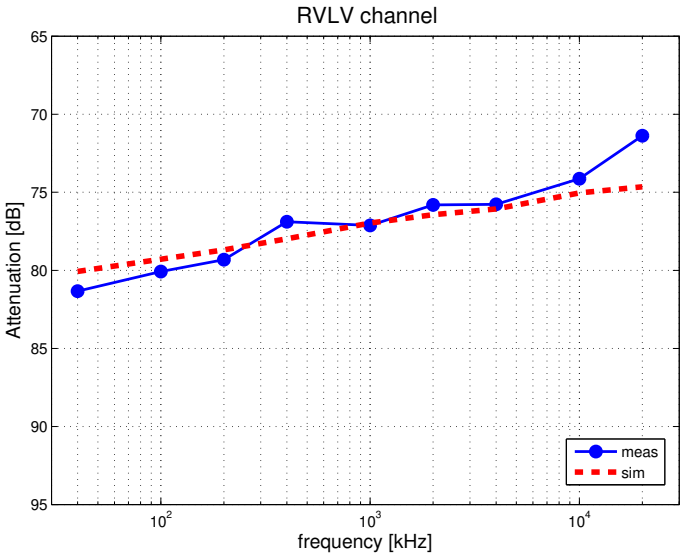

Figure 3.35: In vivo measurement results for the inter-ventricular channel, where the solid line represents the in vivo trial, whereas the dashed line represents simulation results.

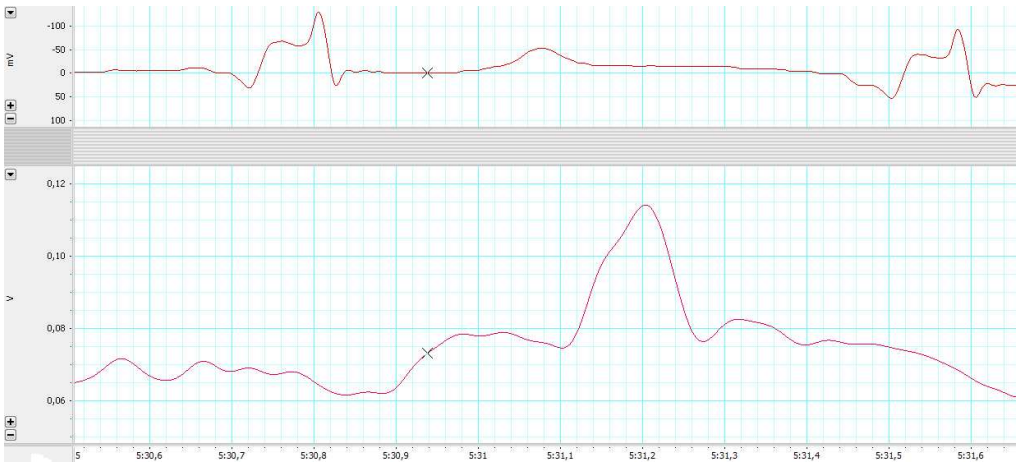

Figure 3.36: The maximum amplitude swing of the envelope (bottom signal) referred to ECG (top signal) over one cardiac cycle. The abscissa represents the time, whereas the ordinates represents the voltage of the signals

est amplitude swing was retrieved during deflation phase. During deflation phase the amplitude swing between best- and worst- timing reduces to 3 dB. This confirms the dependency of the IBC signal attenuation on both the effective channel length and the environment condition.

The dependency on the heart beating can be considered to efficiently transfer data among the devices. However, for LCP synchronization purposes, the transmission timing could be constrained by the information latency constraint. For example, if we consider physiological pacemakers, we need to transfer the P-wave information from the RA capsule to the RV capsule during the early PR-interval.

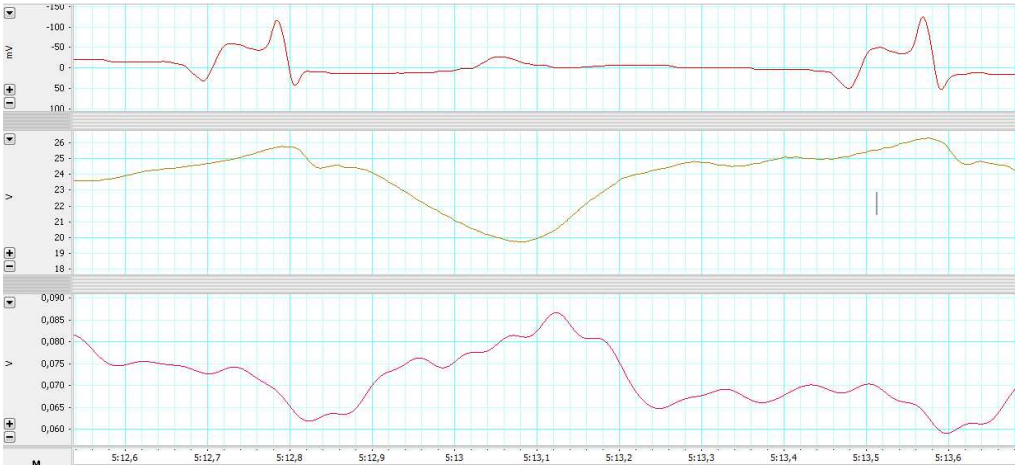

Figure 3.37: The minimum amplitude swing of the envelope (3^{rd} signal from the top) referred to ECG (1^{st} signal from the top) and LV volume change (2^{nd} signal from the top) over one cardiac cycle. The abscissa represents the time, whereas the ordinates represents the voltage of the signals.

Figure 3.38: Long-time representation of the envelope amplitude. In green the raw envelope signal, in red the envelope signal low-pass filtered at 20 Hz; in purple the envelope signal low-pass filtered at 0.7 Hz

3.3 Discussion

The simulations performed in this work highlight the need for accurate models to characterize galvanic intra-body communication channels for deep-implant devices. It was shown that the accurate and the simple geometry models led to different results in terms of both attenuation and frequency trend. Even though the heart anatomy changes among the population, accurate model showed to better follow in vivo frequency trends. Multi-nodal LCP systems need to communicate with different devices set in different positions leading to completely different channels. We estimated through simulations the attenuation levels for all the channels involved in a CRT-leadless system.
The attenuation levels of the trans-thoracic channel are much lower than cardiac ones. The reason is that the surface electrodes can be optimally placed on the body surface to maximize the differential voltage across the receiver dipole. The mutual orientation between emitter and receiver strongly impact the signal attenuation. Nevertheless, the communication must be possible for any implant positioning.
Worst and best-case conditions were identified for the intra-cardiac channel. The attenuation variability according to positioning can be used to set the link margin of the channel considering the worst-case scenario and design a receiver whose specifications allow demodulating data either way. For the intra-ventricular channel, it was found that the link margin reduces at high frequency. The reason is that longer channels experience higher attenuation and have higher relative benefits of working at frequencies resulting in higher conductivity of tissues.
The simulation model has been verified using a galvanically isolated measurement system using capsule prototypes having the same size as the simulated capsules. To verify the coherence between the simulation environment and the suggested measurement setup, we compared in-vitro measurements with simulation results. To do so, we have used an NaCl-solution whose concentration was adapted to follow the frequency trend of the heart conductivity. This technique allows predicting attenuation difference due to conductivity variation and made possible the verification of the simulation approach, but it cannot replace in vivo experiment due to the homogeneity of the phantom.
In vivo experiments verified the effect of RA capsule positioning since almost the same difference was found between worst- and best-case between measurement and simulations. The difference of the pointwise results between in vivo measurement and simulation can be explained by the different morphology of the heart and the error introduced from the measurement system and the quasi-static approximation.

The evolution of the IBC signals has been monitored over the whole cardiac cycle showing the influence of the movement of the heart to attenuation values. Furthermore, it was shown that close physiologic changes can impact the propagation of the IBC signals. In particular, it was shown that the attenuation of the intracardiac channel is also impacted by the respiration. The lowest attenuation was experienced during inflation phase, when the lungs are filled with air lowering the overall conductivity of lung tissue

Table 3.4: Pathloss comparison

Technology	frequency	Distance	Attenuation
ISM	2.4 GHz	8.5 cm	87 dB
MICS	402 MHz	9 cm	55 dB
Galvanic IBC	2 MHz	9 cm	70 dB

[45]. Although the anatomy of the respiratory system of the animal model does not match with the human body, it is very likely that a similar effect would be experienced in human bodies.

It is worth pointing out that the receiver input resistance plays a role in the attenuation level as well. In this particular case, the simulation showed that an input resistance of the order of 10 kΩ maximize the incoming signal. It will be a good approach for designers to choose an input resistance that is, at least, ten times bigger than the bulk impedance across the electrodes maximizing the input signal level concerning the resistive thermal noise.

All the IBC channels considered by this study show lower attenuation at high frequencies. However, micro-electronic circuitry requires more power as soon as we increase the working frequency. The optimal frequency will depend on the particular application targeted, but in any case, IBC frequencies are well below standard RF communication frequencies. Considering the worst-case scenario, the IBC pathloss is lower than ISM band for a similar distance [70], while it is 15 dB higher than MICS band at the same distance.

Table 3.4 resumes the values of the attenuation of ISM, MICS and IBC for intra cardiac wave propagation. A further advantage of galvanic IBC is the size reduction since there are no additional components, such as antennas, needed. This reduces the biocompatibility and integration issues, especially in the MICS band region due to size limits coming from the relatively long wavelength of the carrier signals. Indeed, the electrodes can be shared for several functions such as stimulus delivery, ECG detection, and communication, reducing device cost and volume. Moreover, Galvanic IBC improves the cyber-security of communication since eavesdropping would require direct contact with the patient. For all of these reasons, galvanic IBC can be a valuable technique for LCP applications.

4 Ultra-Low-Power transceiver

The characterization of the channel attenuation for Leadless pacemaker applications described in Chapter 3 was an essential step for the design of power-optimized transceivers. Hereafter, we will consider only the synchronization issue of multi-node leadless pacemakers since it is the most critical communication in terms of average power consumption. Indeed, synchronization among capsules must occur each cardiac cycle to adapt the timing of the therapy stimuli according to the spontaneous activity of the heart. In particular, the transceiver must be able to send cardiac event detection information from one capsule implanted in a first chamber of the patient heart to another capsule that is implanted in a neighbor chamber of the multi-LCP system. The cardiac event information will be used by the receiver capsule to trigger the therapy according to the other chamber activity. This information must occur each cardiac cycle for the whole device lifetime; thus it requires an ultra-low-power technique to minimize the power budget of the wireless communication. In the following section, we specify the constraints of the intra-cardiac channel for leadless pacemakers using galvanic IBC. Then, we point out a convenient ultra-low power receiver architecture, the Super-Regenerative Receiver, which can sustain the high sensitivity constraint that this kind of application requires. Finally, a CMOS design tailored to fit the specification is proposed.

4.1 Transceiver requirements

In this section, we consider the main characteristics of the transceiver separately, evaluating the maximum acceptable values for each of them.

4.1.1 Average current consumption

Leadless Cardiac Pacemakers are limited in size, reducing the battery capacity, which ranges in [120 - 248]mAh [36, 71]. Nevertheless, LCP lifetime must be ensured for several years to reduce surgical operation required to replace the exhausted device with a new

one. Let us evaluate the average current budget leading to device longevity of 10 years. To do so, let us consider the whole battery capacity range [120 - 248] mAh. We can easily calculate the average current consumption range as

$$I_{average} = \frac{battery\ capacity}{10\ years} \approx \frac{[120 - 248]\ mAh}{87600\ h} = [1.37 - 2.83]\ \mu A. \tag{4.1}$$

Thus, the communication module of LCPs should be able to operate with an average current I_{COM} lower than $I_{average}$ to minimize the reduction of the device longevity. As a rule of thumb, we can set I_{COM} one order of magnitude lower than $I_{average}$, leading to values as low as hundreds of nA.

4.1.2 Latency

As a gold standard, physicians measure heart chamber synchrony through Doppler echocardiography. Echocardiography relies on ultra-sound pulse wave reflections, where the time resolution of images mainly comes from the length of the pulse-width and the propagation delay through the media. However, the longer the pulse-width duration, the better the image quality [72, 73]. As a compromise, the manufactures of echocardiography systems provide resolution of the order of 10 ms. Thus, from a clinical validation point of view, atrioventricular (AV) synchronization can have, at most, the same time resolution of doppler echocardiography systems. To keep the same time resolution for AV synchronization in leadless pacemaker systems, we need a maximum uncertainty of 10 ms. Consequently, the maximum latency of the transceiver should not exceed the maximum time uncertainty required.

4.1.3 Maximum emitting voltage

LCPs are medical devices; as such, they must limit emission to ensure safety for patients. The International Commission on Non-Ionizing Radiation Protection (ICNIRP) provides safety guidelines for radiation exposure over a broad frequency spectrum. For what concerns the high-frequency spectrum (HF), the physical quantities used to measure radiation exposure are the Specific Absorption Rate (SAR) and the current density. The scientific community defined SAR as the power absorbed per unit mass, which is related to the increase of temperature in biological tissue. According to ICNIRP, a rise exceeding $1°C$ is considered to be unsafe, and the threshold value of the SAR causing this temperature increase is 4 W/kg. A safety factor of 50 times is introduced for exposure to the general public, giving an average whole-body SAR of 0.08 W/kg [74]. The contribution of the electric field to the SAR is analytically represented by

$$SAR = \frac{\sigma}{\rho} E^2, \tag{4.2}$$

where σ is the conductivity of the biological tissue, ρ is the mass density, and E is the root mean squared value of the internal electric field. Numerical evaluation has been

conducted in [75], where the result suggests that it is not difficult to satisfy the SAR guidelines for Intra-Body Communication. Indeed, the authors obtain SAR levels 60 dB lower than the safety limit, when they apply 1V at the emitter side. For what concerns the current density restriction, the limit of its root mean square value is dependent on signal frequency. In detail, the current density limit was chosen to neglect the influence of transmitted signals to neuronal activity [76], and it is equal to

$$J = \frac{f}{100} \quad [mA/m^2] \tag{4.3}$$

where f is the frequency in Hz. It is not straightforward to comply with the Current density constraint since LCP electrodes can be small in size, reaching considerable current density levels. Considering the smallest electrode described in Section 3.1.5, having a contact surface $S = 4\ mm^2$, and an inter-electrode impedance R_e=1 kΩ, we find out that the current density is equal to

$$J = \frac{V_{RMS}}{S \cdot R_e} = 250 \times V_{RMS} \tag{4.4}$$

Substituting this value in (4.3), we find that the maximum voltage at the emitting capsule must be lower than

$$V_{RMS} = \frac{f}{25000}. \tag{4.5}$$

Recalling the attenuation of the intra-cardiac channel for the worst-case scenario (-70 dB), we can find out the minimum amplitude of the expected input signal of the receiver:

$$v_{in,RMS}(min) = \frac{f}{25000} \times 10^{-\frac{70}{20}} = 4f \times 10^{-8.5} \tag{4.6}$$

The value of $v_{in,RMS}(min)$ can be considered as the minimum sensitivity of the receiver that guarantees the detection of the information in the worst-case scenario.

4.1.4 Modulation

Since the main goal is to optimize transceiver power consumption, the modulation complexity must be maintained as low as possible to relax transceiver performance requirements. On-Off Keying (OOK) and Frequency-Shift Keying (FSK) are viable modulation schemes for ultra-low-power receiver design [77]. FSK modulation, in general, requires more power at the receiver side compared to OOK modulated signals due to the necessity for an internal frequency reference to demodulate incoming signals [78]. In [79], *Cho* proposes a wake-up receiver using injection-locking technique for the demodulation of FSK signals reaching comparable power consumption of OOK receivers [80]. However, the circuit required periodic calibration, and the power consumption evaluation did not include the frequency reference circuitry. The Injection-locking technique lowers the power consumption of FSK receivers with the cost of being more sensitive to blockers [81]. FSK receivers usually experience higher bit rates compared to OOK receivers. However, the LCP synchronization does not require high data rate communications.

Considering that the latency constraint is respected, the cardiac event message reduces to binary information allowing the communication module to work with a single bit demodulation. Thus, we preferred the OOK modulation technique to the FSK in order to reduce the complexity at the emitter side.

4.1.5 Bit Error Rate (BER)

For what concerns the BER, there is not a standard for multi-node pacemaker systems. We can design the receiver to neglect the probability of the communication loss compared to the probability that sensors miss the atrial depolarization. Sensors can miss atrial events for several reasons: pacemaker programming problems (improper sensing threshold), insufficient myocardial voltage signal, lead or pacer failure (fibrosis, fracture), or an electrolyte abnormality [82, 83]. Loss of atrial sensing is 2%-11% among patients of clinical studies reported in the literature [84]. As a rule of thumb, the error probability of the communication must be at least ten times lower the probability of missing atrial detection, leading to a BER of 10^{-3} for single synchronization bit communication. The error probability of OOK signals is well approximated by the function expressed in (4.7)

$$P_e = Q(\sqrt{2E_b/N}), \tag{4.7}$$

where Q is the Q-function whose distribution depends on the energy per bit E_b and the noise amplitude N [85]. Since OOK modulation encodes only one bit per symbol, we can equate the ratio E_b/N to the signal noise ratio (SNR) and the error probability P_e to the BER. Thus (4.7) can be rewritten as

$$BER = Q(\sqrt{2SNR}). \tag{4.8}$$

According to (4.8), the SNR must be greater or equal than 10 dB to achieve a BER of 10^{-3}. Recalling that the input signal amplitude can be as low as -84 dBv and considering a margin of at least 10dB for the receiver noise figure (NF), the maximum input noise amplitude must be lower than -104dBv.

Let us now evaluate the characteristics of the OOK modulation pulse to find out the limiting values according to the allowed noise contribution. For the sake of clarity, we graphically represented the synchronization pulse in Figure 4.1, where T_{bit} represents the time duration of a single bit, and T_{CC} is the communication period that can vary according to the cardiac cycle. We can assume that T_{CC} is infinitely longer than T_{bit}, allowing to reducing the time-analysis of the signal to a single pulse. Thus, considering only the first harmonic of the carrier, the synchronization pulse can be represented in the time domain as

$$s(t) = \prod_{\frac{T_{bit}}{2}} \cdot cos(2\pi f_0 t) \tag{4.9}$$

where Π is the rectangular function, t is the time variable, and f_0 is the carrier frequency value. Let us now analyze the synchronization signal in the frequency domain $S(f)$.

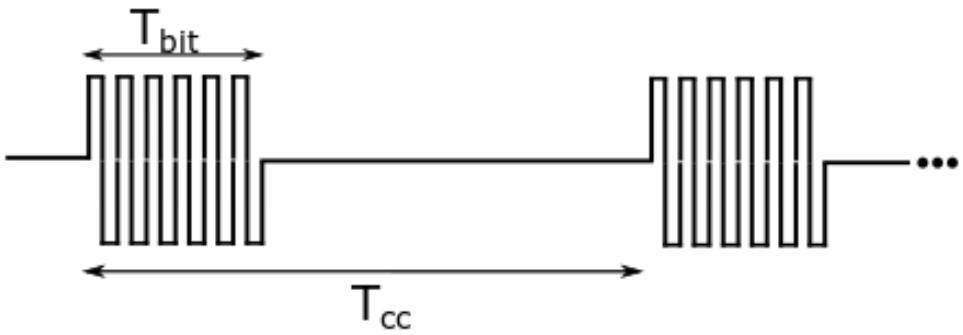

Figure 4.1: Example of OOK signal for LCP synchronization

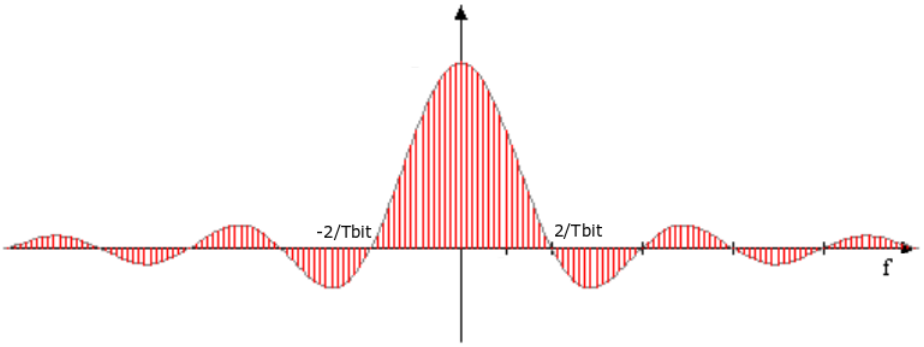

Figure 4.2: Example of OOK signal for LCP synchronization in frequency domain

Applying the convolution theorem of the Fourier transform, we can easily retrieve the analytical representation of synchronization pulse in the positive frequency domain [86].

$$\mathscr{F}\{s(t)\} = S(f) = T_{bit} Sinc(\pi f T_{bit}) * \delta(f - f_0). \tag{4.10}$$

For the convolution property of the Dirac function $\delta(f)$, we can represent $S(f)$ as a Sinc signal centered at f_0, as depicted in Figure 4.2 We can reasonably approximate the bandwidth of the synchronization signal to the main lobe of $S(f)$ that is equal to $4 \times \frac{1}{T_{bit}}$. The IBC channel can be considered as an Additive White Gaussian Noise channel (AWGN). Under this assumption, we can model the the thermal noise of the inter-electrode resistance as a voltage source, whose spectral density is

$$N_0 = \sqrt{4K_B \times T \times R \times BW} \tag{4.11}$$

where K_B is the Boltzmann constant, T is the temperature in kelvin, R is the inter-electrode resistance and BW is the bandwidth of interest. Considering that the body temperature is approximately $37°C$ (310,15 K), for R =1 kΩ, the spectral noise density is

$$N_0 = 4,13\ nV/\sqrt{Hz} = -166,65\ dBv/\sqrt{Hz} \tag{4.12}$$

Table 4.1: transceiver specification for LCP synchronization

Parameter	**Value**
Emitting voltage	$\frac{f}{25000} V_{RMS}$
Latency	10 ms
Modulation	OOK
T_{bit}(min)	1 ps
BER	10^{-3}
SNR	10 dB
Sensitivity	$4f \times 10^{-8.5}$

Classically, the input resistance of the receiver is matched with the equivalent source resistance to minimize the input noise of the receiver. Here, to maximize the useful input voltage of the receiver for the intra-cardiac channel, the input resistance of the receiver must be much greater than the equivalent inter-electrode resistance for the considerations pointed out in subsubsection 3.1.6.5. Thus, the input noise can be considered equal to the thermal noise of the inter-electrode resistance. As a result, we can find the maximum allowed bandwidth of the synchronization signal as

$$BW \cdot N_0 \leq -104dBv \Rightarrow BW = 4\ THz. \tag{4.13}$$

Recalling the relation between the bit duration and bandwidth of the OOK-modulated synchronization signal, we find a minimum bit duration $T_{bit} = 1\ ps$.
To conclude this section, we summarize all the technical requirements of the transceiver in Table 4.1. Those requirements will be used for the receiver design developed in section 4.4.

4.2 OOK receiver state of the art

Low-power OOK receivers use envelope-detectors for demodulation purposes. Thus, without appropriate filtering, they can suffer the presence of interferers [87]. Therefore, external components are usually necessary to filter out the interferers at the front-end. In [88], *Huang* suggests an envelope detector with a double sampling solution to reduce the noise effect on the demodulator performance. In the last decade, several quasi-passive wake-up receivers have been proposed [89, 90, 91, 92, 93]. Those solutions rely on signal rectification techniques already used for wireless power transfer [94]. This method is suited for reaching power consumption values in the sub-micro Watt scale. By the way, OOK receivers usually have low sensitivity due to diode threshold voltage activation. In [93], pre-layout simulations shows the feasibility of a receiver with sub-nW power consumption. However, correlation functions are applied to the base-band signal increasing

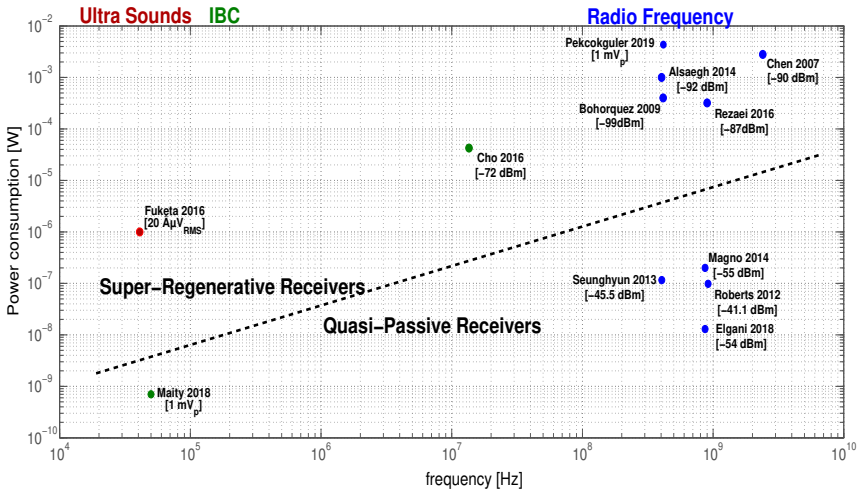

Figure 4.3: Power consumption of Ultra-low-power OOK receivers proposed in the literature

the latency of the demodulation up to 25 ms for an input signal of 1 mV. An elegant approach to minimize power consumption while increasing the sensitivity of OOK-receivers comes from Super-Regenerative architecture. Super-Regenerative Receiver (SRR) has been widely used in literature for ultra-low power applications since only two RF blocks are required to demodulate OOK signals [95]. SRR architecture can be used on the whole frequency spectrum and with different physical waves. In [96], *Fuketa* designed an SRR receiver in 0.25μm technology for ultrasound communication using an external transducer to couple the front-end LNA of the receiver. Super-Regenerative receivers for medical applications in the MICS band are proposed in [97, 98, 99], whereas receiver designs for the ISM band are suggested in [100] and [101] with center frequency respectively at 900MHz and 2.4GHz. A low power solution for IBC communication for body surface applications is also provided in [80] using a carrier frequency of 13.56 MHz. Figure 4.3 resumes the performance of all reported OOK-receivers, where we can see a linear dependence of the power consumption to frequency. High sensitivity values are reachable on the whole frequency spectrum thanks to the high gain of the SRR architecture. Low carrier frequency limits Super-Regenerative receivers in terms of data rate, as explained in section 4.3.1. Therefore, it is essential to correctly choose the carrier frequency according to the minimum data rate requirements. LCP synchronization is a low data rate communication requiring high sensitivity and broad input dynamics. For this reason, we opted for Super-Regenerative design among the low power alternatives of OOK receivers. In the next paragraph, we focus on SRR architecture, giving a detailed description of the analytical principles governing its performance.

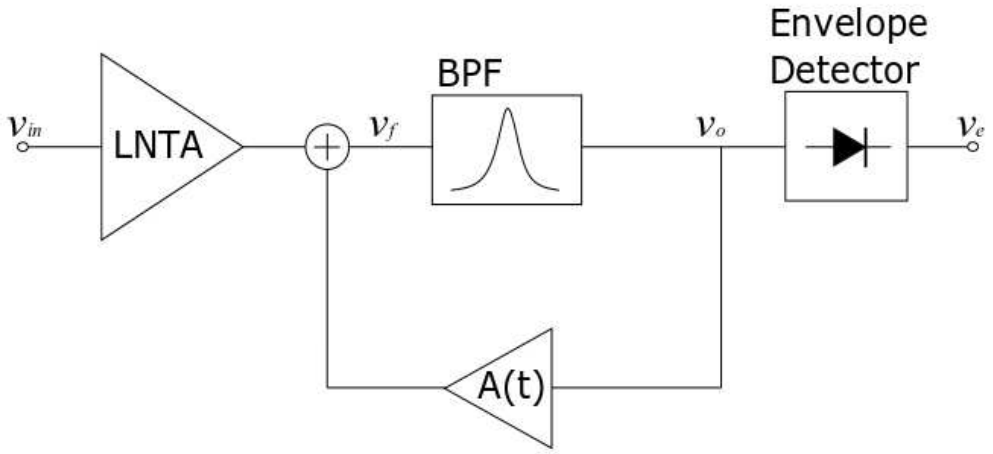

Figure 4.4: Block diagram of a Super-Regenerative Receiver

4.3 Super-Regenerative Receiver (SRR)

The super-Regenerative Receiver was invented by E. Armstrong in 1922 [102]. It was used during WWII to detect radio signals of military air-force. Technology improvement made the super-regenerative receiver less attractive compared to super-heterodyne architectures becoming obsolete by the late 1950s [95]. However, in the last decades, the SRR is back in fashion thanks to the rise of ultra-low-power sensor applications. There are no circuits as the SRR that allow us to get the greatest sensitivity with definitely the minimum number of active devices [103]. It is possible to achieve extremely high RF amplification and narrow-band filtering with a limited amount of current consumption thanks to the SRR architecture. As pointed out in Figure 4.4, the core of the SRR is an oscillator whose amplifier has a time-dependent gain. Above a critical gain value, the oscillator is able to satisfy the first Barkhausen criterion [104] that is necessary to induce instability.

A control signal drives the time-evolution of the gain to counteract the oscillator dispersion periodically. As a result, the system alternates instable periods, where it instaurates oscillations, and damping periods, where the control signal quenches the oscillations. The resonant tank circuit that fixes the resonance frequency of the oscillator is coupled with the input signal. Thus, the response of the oscillator varies according to the amplitude and the frequency of the input signal. The second active device required by the SRR is the low noise transconductance amplifier (LNTA) at the front-end of the receiver. The LNTA has a dual function: it injects in the oscillator tank an amount of current that is proportional to the amplitude of the input signal, and it isolates the input interface from the oscillations coming from the SRO reducing the leakage that would cause involuntary emissions once the system is resonating. There are two operating modes for the SRR receiver: linear mode, and logarithmic mode. The difference between the

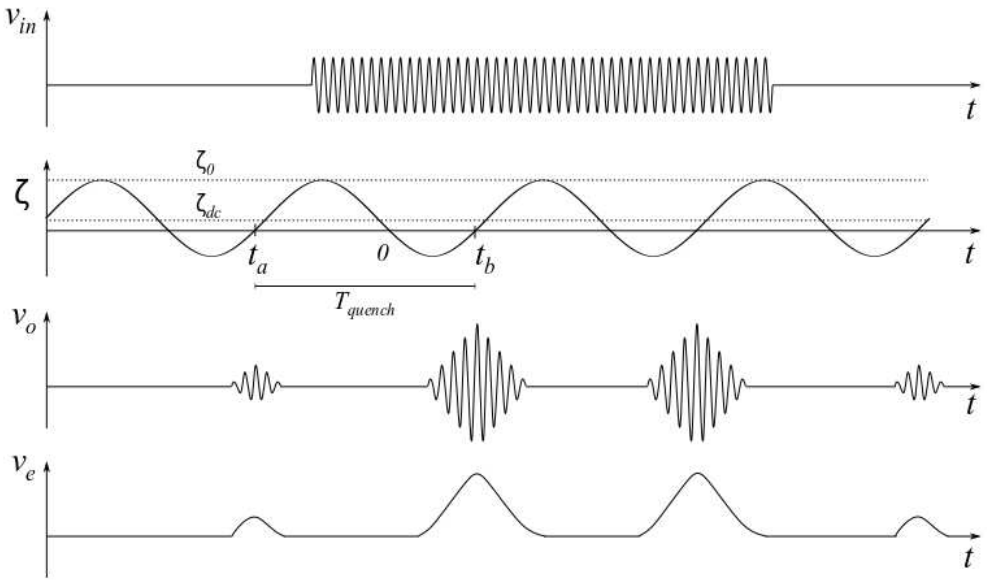

Figure 4.5: Evolution of the input signal through super-regenerative receivers according to the damping function ζ

operating modes stands in the interpretation of the detector output. In linear mode, the timing of the oscillator peak is periodic and depends only on the quench signal evolution. Hence, the detector works as an AM demodulator that periodically samples the peak voltage of the SRO output. In logarithmic mode, the quench signal lasts for an amount of time that is long enough to let the oscillator saturate. In this case, the information is encoded in the rising time of the oscillator to reach saturation. In logarithmic mode, the amplitude of the oscillator output is constant, but the incremental area under the envelope is proportional to the logarithm of the amplitude of v_{in} [105]. To point out the properties and characteristics of the SRR, the outcomes of a quantitative analysis are reported in the following paragraphs.

4.3.1 Analytic model of the SRR

Here, we summarize the outcomes of the analytical studies about the SRR, which were performed in previous works [105, 106]. A more detailed description is reported in the Appendix A.

4.3.1.1 Time domain analysis

Considering that the frequency behavior of the whole system, shown in Figure 4.4, is dominated by the band-pass filter, the response SRR is given by the solution of a

Super-regenerative gain	$K_s(t) = e^{-\omega_0 \int_0^{t_b} \zeta(\lambda)d\lambda}$
Sensitivity curve	$s(t) = e^{\omega_0 \int_0^{t} \zeta(\lambda)d\lambda}$
Normalized envelope	$p(t) = e^{-\omega_0 \int_{t_b}^{t} \zeta(\lambda)d\lambda}$
Regenerative gain	$K_r(t) = \zeta_0\omega_0 \int_{t_a}^{t_b} p_c(\tau)s(\tau)d\tau$

Table 4.2: Variables of the output response of the SRR when the input signal $v_in(t)$ is applied

second-order differential equation:

$$\ddot{v}_o(t) + 2\zeta(t)\omega_0\dot{v}_o(t) + \omega^2 v_o(t) = K_0 2\zeta_0\omega_0\dot{v}_{in}(t). \tag{4.14}$$

K_0 is the minimum attenuation of the filter, ω_0 is the resonant pulsation; whereas $\zeta(t)$ is the instantaneous damping factor, which is defined as

$$\zeta(t) = \zeta_0(1 - K_0 A(t)), \tag{4.15}$$

where ζ_0 is the quiescent damping factor.
The time evolution of the output signal of a SRR system is plotted in Figure 4.5. The instantaneous damping factor $\zeta(t)$ depends on the feedback amplifier gain that is controlled by the quench signal. When $\zeta(t) = 0$, the feedback amplifier counterbalances the dispersion of the band pass filter. The time interval during which $\zeta(t) < 0$ determines the super-regenerative interval, where the feedback amplifier is able to drive the system into instability. At $t = 0$, $\zeta(t) = 0$ meaning that the system satisfies the condition to oscillate. At this point, the injected signal significantly changes the initial condition of the oscillating system; thus, the contribution of the input signal reaches its maximum at $t = 0$. Then, the oscillation amplitude increases reaching its maximum value at $t = t_b$, where $\zeta(t)$ becomes positive and the oscillation is damped.
The quenching period T_{quench} must ensure that the oscillation expires to avoid that previous cycles interferes with the real-time demodulation.
Let us define the input signal as

$$v(t) = V p_c(t) cos(\omega + \phi), \tag{4.16}$$

where V is the amplitude, $p_c(t)$ is the *Normalized pulse envelope*, ω is the angular frequency and ϕ is the phase of the signal.
It can be shown that the output response of the SRR is given by

$$v_o(t) = V K_0 K_r(t) K_s(t) p(t)\ cos(\omega_0 t + \phi), \tag{4.17}$$

under the assumption that the system is underdamped (4.18) and that the damping factor changes slowly (4.19), such that

$$\zeta^2(t) << 1 \tag{4.18}$$

$$\dot{\zeta}(t) << \omega_0 \tag{4.19}$$

We represented the output response (4.17) using the variables resumed in Table 4.2. As can be seen, the receiver has an exponential response, boosting very low input signals up to supply voltage levels.

4.3.1.2 Frequency domain analysis

Let us consider the response to an input with arbitrary frequency

$$v_o(t) = VKp(t)\frac{\omega}{\omega_0}\frac{\int_{t_a}^{t_b} p_c(\tau)s(\tau)cos[(\omega-\omega_0)\tau+\omega_0 t+\phi]d\tau}{\int_{t_a}^{t_b} p_c(\tau)s(\tau)d\tau} \tag{4.20}$$

Assuming that $p_c(t)$ and $s(t)$ are equal to zero out of the considered interval $[t_a; t_b]$, we can define the complex function

$$\psi(\omega) = \int_{-\infty}^{\infty} p_c(t)s(t)e^{j\omega t}dt = \left[\int_{-\infty}^{\infty} p_c(t)s(t)e^{-j\omega t}dt\right]^* = \mathscr{F}^*\left\{p_c(t)s(t)\right\} \tag{4.21}$$

It can be shown that the frequency response of the SRR is

$$H(\omega) = \frac{\omega}{\omega_0}\frac{\psi(\omega-\omega_0)}{\psi(0)}. \tag{4.22}$$

Thus, we can rewrite the SRR output as

$$v_o(t) = VKp(t)|H(\omega)|cos[\omega_0 t+\phi+\angle H(\omega)] \tag{4.23}$$

Note that the frequency response of the Super-Regenerative output is a band-pass filter centered at the resonance frequency ω_0 whose output linearly depends on the amplitude of the input signal. This analysis is valid as far as the oscillations are small enough to keep the feedback amplifier in linear region. When the oscillation increases over an amplitude threshold depending on the characheristics of the feedback amplifier, the gain $A(t)$ reduces changing the instantaneous damping function. In this condition, the oscillation can reach saturation before $t = t_b$ when the oscillator is quenched and the output signal is damped out [105].

4.3.1.3 Noise analysis

Performing the time domain analysis using as input signal the noise n(t), we can find the noise contribution to the output response of the SRR such that

$$v_{o,noise}(t) = 2\zeta_0 K_0 K_s p(t)\omega_0 \int n(\tau)s(\tau)sin[\omega_0(t-\tau)]d\tau. \tag{4.24}$$

We can finally express the SNR over a unitary resistance [106]

$$SNR = \frac{V^2_{o,signalRMS}(t)}{\mathscr{E}\{v_{o,noise}(t)\}} = \frac{E_b\left(\int_{-\infty}^{\infty} p(\tau)s(\tau)d\tau\right)^2}{N_0\int_{-\infty}^{\infty} p^2(\tau)d\tau\int_{-\infty}^{\infty} s^2(\tau)d\tau}, \tag{4.25}$$

where

$$E_b = V^2_{in,RMS}(t) = \frac{1}{2}V^2 \int_{-\infty}^{\infty} p(\tau)d\tau. \tag{4.26}$$

Recalling the Cauchy-Schwartz inequality [85], we can see that the maximum value of (A.50) is $\frac{E_b}{N_0}$ that occurs when the envelope of the input signal $p(t)$ equals the sensitivity curve $s(t)$ [106]. For a practical point of view, we can apply an OOK modulated input with pulse duration that completely covers the sensitivity curve. In such a condition, we can neglect the contribution of the input envelope achieving the maximum value of the SNR. It is worth noting that the maximum value of the SNR for the SRR equals the SNR of standard OOK architectures $\frac{E_b}{N_0}$

4.4 SRR design

In the previous section, we pointed out the main characteristics of the SRR architecture. A quantitative analysis showed the critical importance of the quench signal on the overall response of the system. In particular, the sensitivity of the SRR improves when the quench signal varies slowly. LCP synchronization does not require high-speed communications, relaxing the constraint on the quenching frequency. To minimize both power consumption and chip size, we decided to build the quench signal using the 32 kHz clock of the LCP device. In this work, we do not consider the implementation of the quench signal circuitry, which was rather ideally modeled. All the blocks of the SRR represented in Figure 4.6 were designed using the technology XH018 from *XFAB©*. XH018 is a 0.18 μm technology for CMOS design that allows High Voltage applications required for therapy stimulation. Thus, this technology allows mono-chip integration of all the functional blocks required by pacemaker devices reducing both the cost and the size of the whole device production. In the next section, we will give a detailed insight into the receiver design, considering, first, each block as a standalone component, and then, describe the performance of the global functioning.

4.4.1 Receiver design

4.4.1.1 The oscillator

Let us start from the core of the Super-Regenerative receiver: the oscillator. Before dealing with the circuit design, let us remind some theory of oscillators that is essential to understand the design choices. Oscillators consist of an amplifying stage, a frequency-selective network, and a positive feedback network. The feedback circuit is required to sum the output signal to the input signal. Under proper conditions, the positive feedback system establishes an oscillatory response. Let us consider a generic feedback system, like the one shown in Figure 4.7. The direct gain of the system is $A(j\omega)$, whereas $\beta(j\omega)$ is the transfer function of the feedback network.

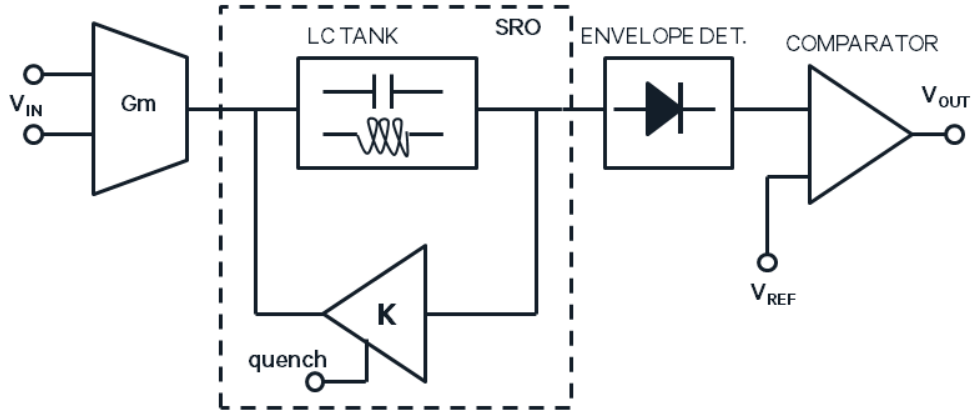

Figure 4.6: Block scheme of a Super-Regenerative Receiver

By circuit inspection of Figure 4.7, we can write

$$\begin{aligned} v_o &= A(j\omega)v_e \\ v_f &= \beta(j\omega)v_o \\ v_e &= v_i + v_f = v_i + A(j\omega)\beta(j\omega)v_e \Rightarrow \\ \Rightarrow v_i &= v_e[1 - A(j\omega)\beta(j\omega)] \end{aligned}$$

Let us express the closed-loop gain A_{cl} of the feedback circuit as

$$A_{cl}(j\omega) = \frac{v_o}{v_i} = \frac{A(j\omega)}{1 - A(j\omega)\beta(j\omega)} \tag{4.27}$$

where the product $A(j\omega)\beta(j\omega)$ is also known as *open-loop gain*. To let the system oscillate, the denominator of the open-loop gain must equal zero [107]. This condition is known as *Barkhausen criterion*:

$$1 - A(j\omega)\beta(j\omega) = 0 \Rightarrow A(j\omega)\beta(j\omega) = 1. \tag{4.28}$$

Let us consider to have a real positive gain $A(j\omega) = A_o(\omega)$ and rewrite the feedback transfer function as the sum of its real and imaginary contributions.

$$\beta(j\omega) = \beta_r(\omega) + j\beta_i(\omega) \tag{4.29}$$

It is possible to express (4.28) as

$$A_o(\omega)\beta_r(\omega) + jA_o(\omega)\beta_i(\omega) = 1 \tag{4.30}$$

Equating both terms of 4.30, we find that the *Barkhausen criterion* is respected if

$$A_o(\omega)\beta_r(\omega) = 1 \tag{4.31}$$

$$\beta_i(\omega) = 0 \tag{4.32}$$

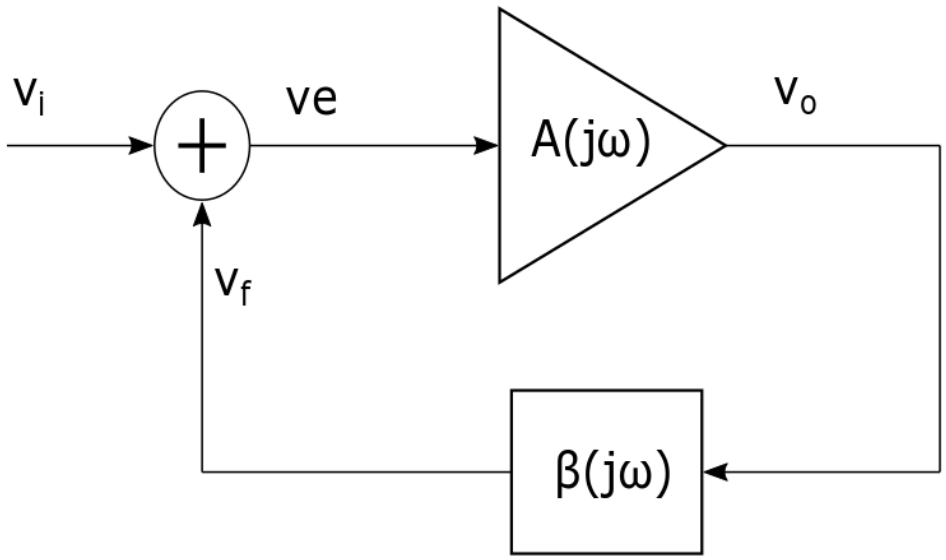

Figure 4.7: block scheme of the feedback circuit

The condition (4.31) is known as the gain condition, whereas (4.32) is known as the frequency condition. Thus, oscillations occur only for the frequency where the imaginary part of the feedback transfer function is equal to zero. The frequency of the oscillation is known as *resonance frequency* and symbolically represented by ω_0.
Several circuit architectures respecting the *Barkhausen criterion* can guarantee oscillation. We are interested in a particular family of oscillators having a frequency selective network made of passive components, called tuned circuit oscillators. Tuned circuit oscillators are widely used for frequencies above 100 kHz since they require only one transistor to counteract oscillation damping. The general structure of a CMOS tuned oscillators is represented in Figure 4.8, where we can identify the CMOS transistor ideal circuit model and the passive selective network, also known as *tank circuit*, composed by the reactive components Z_1, Z_2, and Z_3.
By circuit inspection of Figure 4.8, it is straightforward to retrieve the open-loop gain of the system that is represented in (4.33).

$$A\beta = \frac{-g_m r_d Z_1 Z_2}{r_d(Z_1 + Z_2 + Z_3) + Z_2(Z_1 + Z_3)}. \tag{4.33}$$

For the sake of simplicity let us consider ideal components such that the tank circuit is purely reactive having $Z_1(j\omega) = jX_1(\omega)$, $Z_2(j\omega) = jX_2(\omega)$ and $Z_3(j\omega) = jX_3(\omega)$. As such, we can express the open-loop gain as

$$A\beta = \frac{g_m r_d X_1(\omega) X_2(\omega)}{jr_d[X_1(\omega) + X_2(\omega) + X_3(\omega)] - X_2[(\omega)(X_1(\omega) + X_3(\omega)]}. \tag{4.34}$$

This circuit has an oscillatory response if the conditions (4.31) and (4.32) are respected. Since r_d is a positive real value, the frequency condition (4.32) is respected if and only

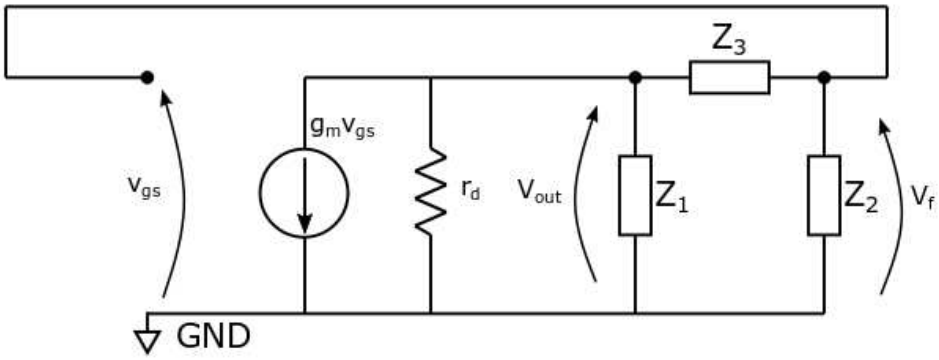

Figure 4.8: Ideal model of single transistor LC-oscillators

if

$$X_1(\omega_0) + X_2(\omega_0) + X_3(\omega_0) = 0. \tag{4.35}$$

At $\omega = \omega_0$, the open-loop gain of the system reduces to

$$A(j\omega_0)\beta(j\omega_0) = \frac{-g_m r_d X_1(\omega_0)}{X_1(\omega_0) + X_3(\omega_0)}. \tag{4.36}$$

Substituting the value of $X_3(\omega_0)$ coming from 4.35 we can rewrite the (4.36) as

$$A(j\omega_0)\beta(j\omega_0) = \frac{g_m r_d X_1(\omega_0)}{X_2(\omega_0)} \geq 1. \tag{4.37}$$

The open-loop gain (eq. 4.37) must be equal to one to respect the gain condition at the resonance frequency, and greater to one to initiate the oscillations. The gain condition is respected if and only if the reactive impedances X_1 and X_2 have the same sign since the transconductance g_m and the drain resistance r_d of the transistor are positive real values. In opposition, the frequency condition is respected if X_3 has opposite sign compared to X_1 and X_2. We decide to choose $Z_1 = C_1$, $Z_2 = C_2$, and $Z_3 = L$ to reduce the number of inductive components. This configuration of the tuned circuit oscillator is known as *Pierce oscillator*, where the resonance frequency is

$$\omega_0 = \frac{1}{\sqrt{LC_{eff}}} \tag{4.38}$$

$$C_{eff} = \frac{C_1 C_2}{C_1 + C_2} \tag{4.39}$$

Moreover, the oscillations can occur if the gain of the amplifier is greater than the capacitive ratio $\frac{C_1}{C_2}$ such that

$$g_m r_d \geq \frac{C_1}{C_2} \tag{4.40}$$

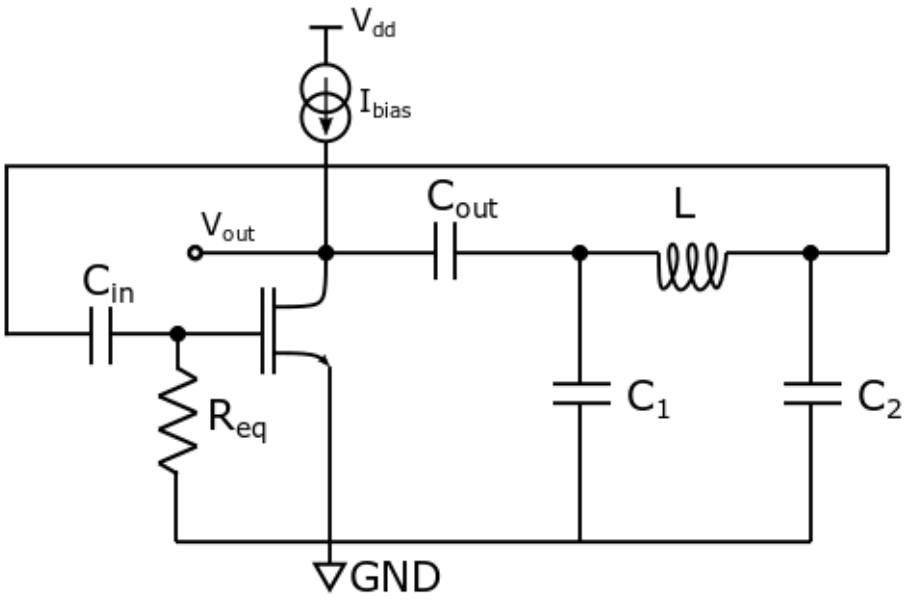

Figure 4.9: CMOS representation of the Pierce oscillator

Figure 4.9 represents the whole circuit of a Pierce oscillator including the two additional decoupling capacitors C_{in} and C_{out}, and the bias network of the amplifier composed of a current source I_{bias} and equivalent gate resistance R_{eq}. Due to the limited working frequency of Intra-Body Communication, the chip integration of the inductance would be unreasonable in terms of size and, consequently, production costs. Thus, we can use an external inductor for the selective network. It is convenient to maximize the reactance value $X_3(\omega_0)$ of the inductor L to limit the sizes of the capacitors C_1 and C_2. In this way, it would be possible to integrate C_1 and C_2, minimizing the number of external components. The component SDR0302-820KL from BOURNS™was selected, which has a surface-mounted package whose size fits the Leadless prototype capsule. This inductor has a typical value of 82 μH with a tolerance of 10%. The tolerance of the inductor must be compensated by trimming the integrated capacitors C_1 and C_2 accordingly. We decided to maximize the resonance frequency to minimize the attenuation levels of the intra-cardiac channel, as explained in Section3.1.5. However, the self-resonance frequency f_{SFR}(min)=12 MHz of the external inductor gives us an upper limit for the working frequency selection. The resonance frequency of the selective network was set to 4 MHz to ensure a stable value for the inductance. Recalling (4.38), the equivalent capacitance of the tank circuit must be equal to 19.32 pF.
The selectivity of the tank circuit depends on its quality factor, which is defined as

$$Q = \frac{1}{R_s}\sqrt{\frac{L}{C_{eff}}} = \frac{\omega_0 L}{R_s}, \tag{4.41}$$

where R_s is the stray resistance of the inductor [107]. We can notice that having an inductance value several orders of magnitude bigger than the equivalent capacitance leads to very high quality factors increasing the selectivity of the receiver. On the other hand, a very high selective network requires accurate reactance values that would lead to a complex trimming network of the capacitors. In order to limit the trimming of the equivalent capacitor to 1%, leading to a bandwidth of at least 40 KHz, we set the series resistance of the inductor $R_s = 16\ \Omega$. By specification, the maximum stray resistance of the chosen inductance is 2.10 Ω requiring an additional resistance of 14 Ω. The additional resistance needing is good news since it can be obtained through the trace resistance, relaxing the constraint of the layout.
To avoid that the bias network of the common source amplifier degrades the oscillatory response of the system, we integrated a decoupling capacitor C_{in}, whose value was selected to behave as a short circuit at the resonance frequency. The value of C_{in} must be sized according to the value of the gate equivalent resistance R_{eq} such that the cutoff frequency of the resulting passive high-pass filter lies at least a decade from ω_0.

$$C_{in} = \frac{10}{\omega_0 R_{eq}}. \tag{4.42}$$

For what concerns C_{out}, let us analyze its effect on the system, studying the poles of the transfer function. The open-loop gain equation in the Laplace domain considering C_{out} is

$$A(s)\beta(s) = \frac{-g_m(\frac{1}{LC_1C_2})}{s^3 + s^2\frac{C_1+C_{out}}{r_dC_1C_{out}} + s\frac{C_1+C_2}{LC_1C_2} + \frac{C_1+C_2+C_{out}}{r_dLC_1C_2C_{out}}} \tag{4.43}$$

where $s = j\omega$. Let us recall the transfer function H(s) of feedback oscillators

$$H(s) = \frac{A(s)\beta(s)}{1 - A(s)\beta(s)}. \tag{4.44}$$

To study the stability of the system, we need to characterize the poles of H(s). To do so, it is convenient to rewrite the open-loop gain 4.43 in its polynomial form

$$A(s)\beta(s) = \frac{KN(s)}{D(s)} \tag{4.45}$$

where

$$\begin{aligned} K &= \frac{-g_m}{C_1C_2L}, \qquad N(s) = 1 \\ D(s) &= s^3 + s^2\frac{C_1 + C_{out}}{r_dC_1C_{out}} + s\frac{C_1 + C_2}{LC_1C_2} + \frac{C_1 + C_2 + C_{out}}{r_dLC_1C_2C_{out}}. \end{aligned}$$

The closed loop gain H(s) can be rewritten according to 4.45

$$H(s) = \frac{KN(s)}{D(s) - KN(s)} \tag{4.46}$$

The poles of the system are defined as the values of s for which the denominator equals zero. Thus, let us focus on the denominator of the closed loop gain $D'(s) = D(s) -$

$KN(s)$.

$$D'(s) = s^3 + s^2\frac{C_1 + C_{out}}{r_d C_1 C_{out}} + s\frac{C_1 + C_2}{LC_1C_2} + \frac{C_1 + C_2 + C_{out}}{r_d LC_1C_2C_{out}} + \frac{g_m}{LC_1C_2} \tag{4.47}$$

From (4.47), it is clear that the system has 3 poles. A third-order system can be interpreted as the sum of the responses of a second- and a first-order transfer function.
Let us consider the system at the stability limit point, where the second-order contribution is critically damped such that the damping factor of the second order response can be neglected.

$$D'(s) = (s^2 + \omega_0^2)(s + a) = s^3 + as^2 + \omega_0 s + a\omega_0^2 \tag{4.48}$$

Finally, we can equate (4.48) with (4.47) to characterize the response of the system through the circuit parameters

$$\omega_0^2 = \frac{C_1 + C_2}{LC_1C_2} \tag{4.49}$$

$$a = \frac{C_1 + C_{out}}{r_d C_1 C_{out}} \tag{4.50}$$

$$a\omega_0^2 = \frac{C_1 + C_2 + C_{out}}{r_d LC_1C_2C_{out}} + \frac{g_m}{LC_1C_2} \tag{4.51}$$

From (4.49), we find out that the resonance frequency ω_0 is not impacted by the decoupling capacitor C_{out} and its value is equal to the previous evaluation (4.38). However, C_{out} can impact both the negative pole of the first order contribution and the overall gain, as shown respectively in Equation 4.50 and Equation 4.51.

To find the gain condition ensuring an oscillatory response we can equate

$$a\omega_0^2 = a\omega_0^2 \Rightarrow \tag{4.52}$$

$$\Rightarrow \frac{C_1 + C_{out}}{r_d C_1 C_{out}}\frac{C_1 + C_2}{LC_1C_2} = \frac{C_1 + C_{out} + C_2}{r_d LC_1C_{out}C_2} + \frac{g_m}{LC_1C_2} \Rightarrow \tag{4.53}$$

$$\Rightarrow \frac{\cancel{C_1^2} + \cancel{C_1C_{out}} + \cancel{C_1C_2} + g_m r_d C_1 C_{out}}{r_d LC_1^2 C_{out}C_2} = \frac{\cancel{C_1^2} + \cancel{C_1C_{out}} + \cancel{C_1C_2} + C_{out}C_2}{r_d LC_1^2 C_{out}C_2} \tag{4.54}$$

Since the denominator is different from zero, we can further reduce (4.54) as

$$g_m r_d C_1 = C_2 \Rightarrow \tag{4.55}$$

$$\Rightarrow g_m r_d = \frac{C_2}{C_1} \tag{4.56}$$

Equation (4.56) defines the stability limit, where the system can start oscillations. We find that the capacitor C_{out} has no effects since the same gain condition of 4.40 was found. To let the system start-up oscillations

$$g_m r_d > \frac{C_2}{C_1} \tag{4.57}$$

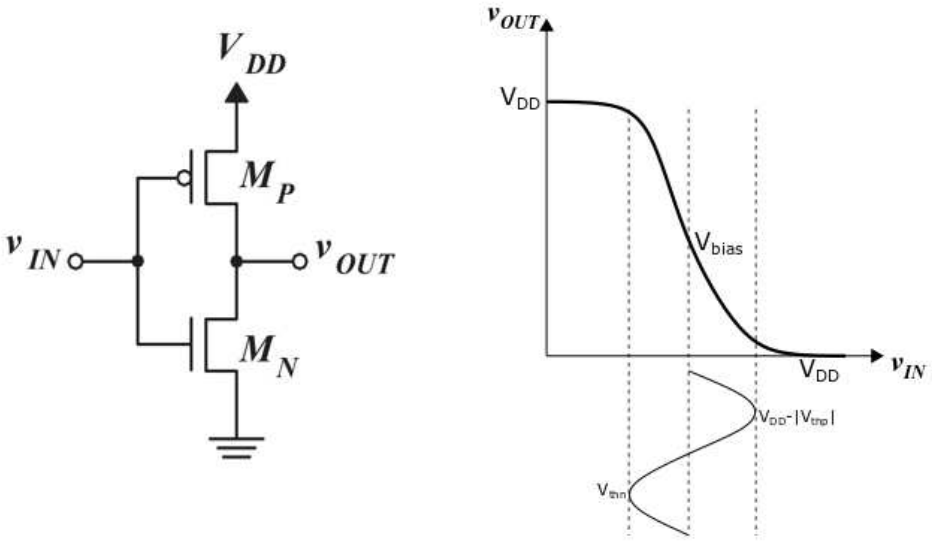

Figure 4.10: CMOS inverter circuit and its voltage trans-characteristics

Finally, the value of C_{out} can be chosen arbitrarily. However, we must ensure that the capacitor does not filter the resonance frequency ω_0. We set C_{out}=2 pF as a compromise between fast transient response and stationary behavior. Having a fast transient response reduces the start-up time of the receiver preventing useless power consumption during receiver stabilization.

4.4.1.2 Front-end amplifier

In the Super-Regenerative architecture, the front-end amplifier has dual functionality:

- to amplify the incoming signal;
- to decouple the resonant circuit and the front-end of the device.

Super-regenerative receivers do not have stringent requirements in terms of gain due to the intrinsic gain of the oscillatory response. On the other hand, the impedance of the front-end circuitry would degrade the selective network dramatically, preventing the rise of oscillation. A low power solution for transconductance amplifiers comes from the CMOS-inverter, which is an essential building block in integrated circuits, finding applications in both digital and analog circuits. The inverter topology finds applications in radio systems as well, thanks to the low complexity and occupational area [108]. Moreover, it allows rail-to-rail operations with reduced supply voltage levels,which is a interesting characteristic for ultra-low-power applications. Specifically, the minimum

supply voltage limit arises from the voltage thresholds of the transistors [109] such that

$$V_{DD} > V_{th,n} + |V_{th,p}|. \tag{4.58}$$

Moreover, the inverter is a single-stage building block. As such, it does not add internal zeroes and poles to the transfer function, which is not the case of conventional amplifiers based on the common-source topology [109]. To further improve the frequency operation of the inverter-amplifier, it is possible to add a feedback network to compensate for the poles coming from parasitic capacitances at the input and the output terminal [110]. The feedback is usually purely resistive; very high frequency applications can use inductors to improve the operational bandwidth[111]. Moreover, the feedback is also used to fix the bias point of the devices stabilizing the gain of the amplifier [112, 113]. The resistive part of the feedback has an impact over the input and the output equivalent resistances and can be used to match the antenna impedance in radio-frequency applications [114, 115].

For a quantitative analysis of the characteristics of the inverter-based amplifier, we reference *Sharroush* [111], who performed both the large and the small signal analysis. The inverter architecture requires to be correctly biased to work as an amplifier. In particular, both the p-MOS and the N-MOS composing the inverter must be biased in the saturation region.
To maximize the linearity and the input swing of the amplifier, the optimal bias point of the inverter must be at the middle point of the transition region of its voltage-transcharateristic. In the case of perfect matching, the transition occurs in the middle of the dynamic; thus, the optimum DC-operating point is $V_{bias} = V_{in} = V_{out} = \frac{V_{DD}}{2}$. To keep both the transistors in saturation region requires that the following inequalities are satisfied:

$$V_{DSn} \geq V_{GSn} - V_{thn}; \tag{4.59}$$

$$V_{DSp} \geq V_{GSp} - |V_{thn}.| \tag{4.60}$$

These conditions are satisfied if the output signal amplitude is limited by

$$V_{bias} - V_{thn} \leq V_{OUT} \leq V_{bias} + |V_{thp}|. \tag{4.61}$$

leading to a maximum output voltage swing $V_{O,swing} = V_{thn} + |V_{thp}|$. Thus, to ensure linearity, the input signal of the amplifier must be lower than

$$v_{in,max} = \frac{V_{O,swing}}{2(g_{mn} + g_{mp})(r_{0n} /\!/ r_{0p})}. \tag{4.62}$$

However, to feed the tank of super-regenerative receiver, we do not necessarily require to ensure linearity since the higher harmonics of the distorted signal would be filtered out by the oscillator. In this condition, we can have a rail-to-rail operation, and the maximum signal amplitude becomes

$$v_{in,max} = \frac{V_{DD}}{2(g_{mn} + g_{mp})(r_{0n} /\!/ r_{0p})}. \tag{4.63}$$

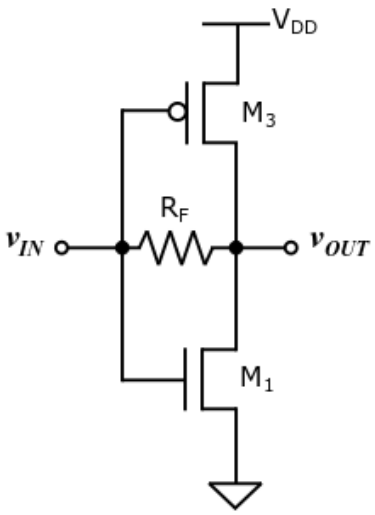

Figure 4.11: Inverter-based amplifier with resistive feedback

For a fixed value of transconductance, the voltage gain depends on the slope of the transition region. Fast transition regions lead to high voltage gains. Increasing the threshold voltages V_{thn} and $|V_{thp}|$, we can narrow the transition region, reaching its maximum when

$$V_{thn} + |V_{thp}| = V_{DD}. \tag{4.64}$$

However, a very narrow transition region is more sensitive to process-related variation (PVT) that would mismatch the inverter. In this condition the circuit would work as a digital inverter, loosing the small signal information. Thus, it is convenient to use the resistive feedback to improve robustness against PVT variations [116]. However, it is of our interest to maximize the value of the feedback resistance R_F to keep the output equivalent impedance as high as possible. As a compromise between bias stability and output gain we set R_F=4 MΩ. A feedback current flow arises whenever input and output bias points diverge from the matching condition. As a result, a voltage drop arises across R_F, tightening the input and output DC points.

To maximize the value of the resistance, we designed a matched inverter-amplifier such that in typical condition we have $V_{in} = V_{out} = \frac{V_{DD}}{2} = 500mV$. The output resistance of the inverter was designed to be much greater than oscillator resistance during precharge phase such that the oscillator gain is independent on the front-end circuitry. Quantitative speaking, we set

$$r_{0,LNTA} = \frac{R_F}{1 - A_v^{-1}} /\!\!/ (r_{0,n} /\!\!/ r_{0,p}) \approx 1\ M\Omega >> r_{0,SRO} = 140\ k\Omega \tag{4.65}$$

The transconductance of the amplifier was maximized to improve the sensitivity of the receiver, achieving

$$G_m = g_{mn} + g_{mp} = 200\ \mu S \tag{4.66}$$

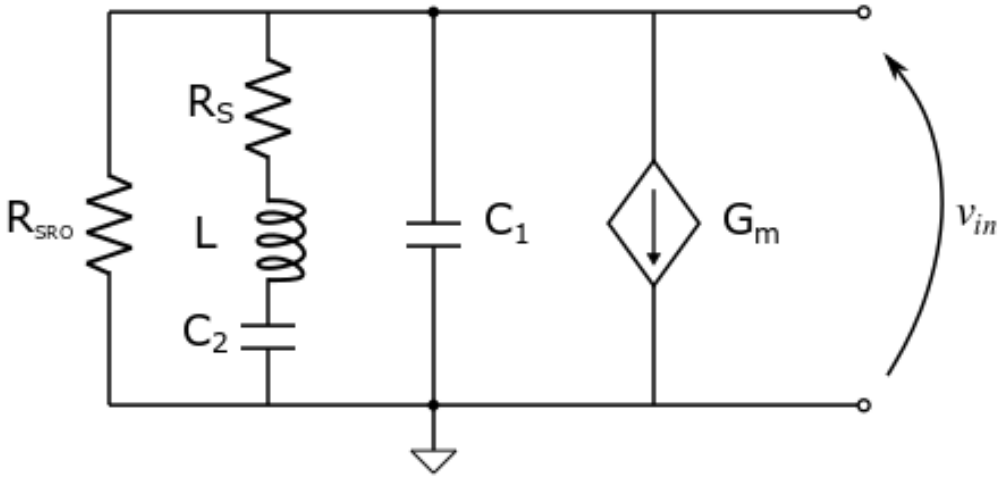

Figure 4.12: Equivalent circuit of the front-end amplifier

The overall gain of the LNTA depends on the charge of the selective network such that

$$A_v(s) = -G_m Z_L(s) \tag{4.67}$$

where

$$Z_L = \frac{s^3 LC_1C_2R_{SRO} + s^2C_2(C_1R_SR_{SRO} + L) + s(C_1R_{SRO} + C_2R_S) + 1}{s^3LC_1C_2 + s^2C_1C_2(R_{SRO} + R_S) + s(C_1 + C_2)} \tag{4.68}$$

For $\omega = \omega_0$ =4 MHz, we will have

$$A_v(j\omega_0) \approx 22.5\ dB \tag{4.69}$$

Let us now evaluate the noise contribution of the inverter-based amplifier. Two main noise contributions must be considered for CMOS circuits: the thermal noise and the flicker noise. The thermal noise is generated in the channels of MOS transistors. For each MOSFET working in saturation region, we can model the thermal noise as an additive current source across the drain and source with a spectral density that is equal to [117]

$$I_n^2 = 4KT\gamma g_m \qquad [A^2/Hz] \tag{4.70}$$

where K is the Boltzmann's constant, T is the temperature in kelvin, and γ is a technology related constant. On the other hand, the flicker noise can be modeled as a voltage source at the gate of the MOSFET with a spectral density given by

$$V_n^2 = \frac{K_n}{W_nLC_{oxn}f} \qquad [V^2/Hz] \tag{4.71}$$

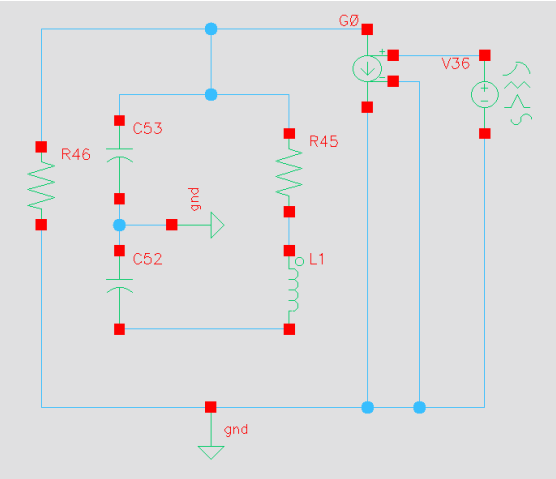

Figure 4.13: Testbench of the ideal front-end amplifier

where K_n is a process related constant, and f is the frequency of operation. Since in our application the signal is centered at 4 MHz, we can neglect the flicker noise contribution. Starting from this assumption, we can find the noise factor of the inverter. Considering that the signal to be amplified has an equivalent resistance R_s with noise power

$$N_{in} = 4KTR_{in}, \tag{4.72}$$

the total noise at the output node, for $Z_L << R_{out}$, is equal to

$$N_{out}(s) = (4KT\gamma g_{mn} + 4KT\gamma g_{mp})Z_L^2(s) + 4KTR_{in}(g_{mn} + g_{mp})^2 Z_L^2(s) \tag{4.73}$$

We can quantify the contribution of the front-end amplifier through the Noise Factor (NF), which is defined as the ratio between the total output noise and the output noise due to the input source [103]. Such that,

$$NF = 1 + \frac{(4KT\gamma g_{mn} + 4KT\gamma g_{mp})}{4KTR_{in}(g_{mn} + g_{mp})^2} \tag{4.74}$$

We can see from (4.74) that the larger the transconductances, the lower is the noise factor of the inverter-amplifier. However, the total output noise increases boosting the gain of the amplifier, as seen in (4.73). By the way, the selectivity of the equivalent load seen by the amplifier strongly reduces the noise contribution.

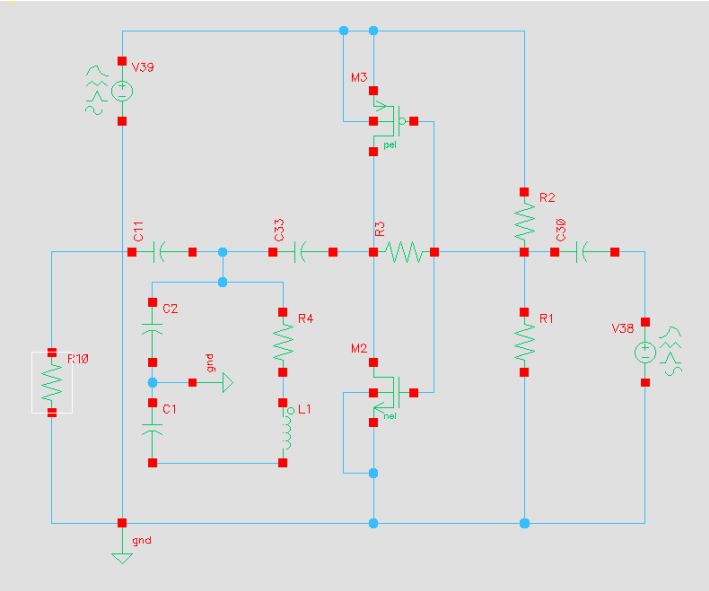

Figure 4.14: Testbech of the inverter-based amplifier with RLC output load

The front-end amplifier was designed using Cadence in Virtuoso© environment, as shown in Figure 4.14. Also the ideal model of the circuit has been designed to verify the analytical approximation we previously performed, where the front-end was substituted by a voltage-controlled current source having gm=200μS. The simulation results are reported in dB-scale by Figure 4.15, where the yellow dotted-line and the red solid-line represent the voltage across the tank circuit respectively for the ideal front-end and for the inverter-based amplifier. We can see that the ideal transconductance amplifier and the inverter-based amplifier almost match, proving that the bandwidth of the amplifier is dominated by the poles of the tank circuit. As expected, the front-end gives us an gain of 22 dB that will contribute to improve the sensitivity of the receiver, boosting the initial voltage of the oscillations.

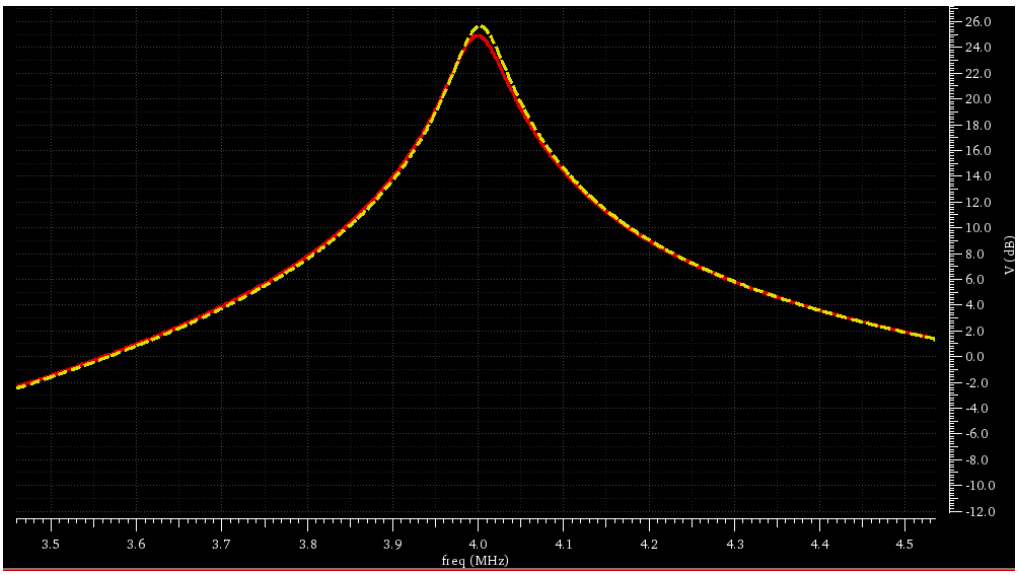

Figure 4.15: Simulation results of the front-end amplifier analysis, where the yellow dotted line represents the result of the ideal front-end amplifier, whereas the red solid line represents the results of the proposed inverter-based amplifier

4.4.1.3 Envelope detector

We have seen that super-regenerative receivers decode information from the envelope of the oscillator output. The simplest way to recover the envelope of a high frequency signal comes from the passive rectifier circuit, which is composed of a diode and an RC low-pass filter [94]. The diode lets the current pass-through charging the capacitor when it operates in the forward-bias region. As a result, the current injection makes the voltage drop across the capacitor $v_e(t)$ to rise. In CMOS circuits, it is common to design diodes using transistors having gates and drains tied together, known as MOS-diodes. The short circuit across the drain and the gate terminals force the transistor to work in the saturation region [109]. Thus, we can model the current passing through the MOS-diode by the large signal equation of the drain current, such that

$$I = I_D = \left(\frac{K'W}{2L}\right)(V_{GS} - V_{th})^2 \tag{4.75}$$

where K' is a constant related to the particular MOS technology, W and L are respectively the width and the length of the transistor channel. For a fixed value of voltage, the wider the channel, the bigger the output current. On the other hand, from the small-signal model of the CMOS transistor, we find out that the equivalent resistance of the MOS-diode is

$$r_{out} \approx \frac{1}{g_m}, \tag{4.76}$$

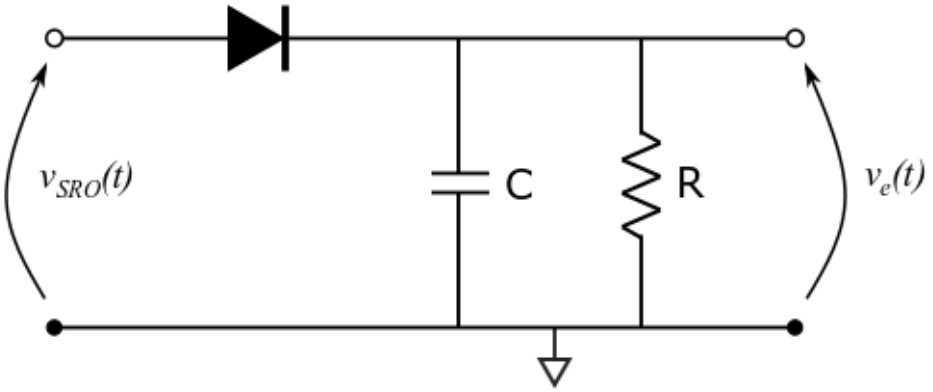

Figure 4.16: Passive envelope detector circuit

where g_m is the transconductance of the CMOS device. For a fixed value of gate-source voltage V_{GS}, the wider the channel, the smaller the equivalent resistor. We decided to use the minimum sizes for the MOS-diode to maximize its resistance and minimize the surface area occupation. As we have seen, the base-band characteristics of the envelope signal will depend on diode sizing. However, high frequency perturbations can interfere with the base-band signal. Indeed, voltage ripples superpose to the low-frequency signal due to the remaining component of the carrier frequency. If the diode operates in the cut-off region, it behaves as an open switch. As a result, the capacitor holds the value of the previous cycle. In this case, voltage ripples are also present due to the current leak through the resistance. Analog designers must carefully choose the time constant of the RC-network $\tau = RC$ to reduce voltage ripples. From a qualitative point of view, τ must be sufficiently large to filter out the high frequency component and small enough to follow the envelope of the incoming signal. If τ is too small, it might not be possible for the comparator to keep a stable value to detect the information correctly. On the other hand, if τ is too large, v_e will not be able to follow the envelope of the signal. For high data rate applications, the choice of the time constant becomes essential, and a compromise between envelope detection and ripple voltage must be found. In particular, for super-regenerative receivers this would arise hangover issues making challenging high data rate operation [105]. In our case, the resonant pulsation ω_0 is three order of magnitude higher than the quenching frequency. Thus, we decided to set the pole related to the time constant in the middle point between the quenching frequency and the resonance frequency. Such that

$$f_{quench} << \frac{1}{2\pi\tau} << \frac{\omega_0}{2\pi}, \tag{4.77}$$

leading to a low-pass filter with a pole at $\frac{1}{2\pi\tau}$=40 kHz.

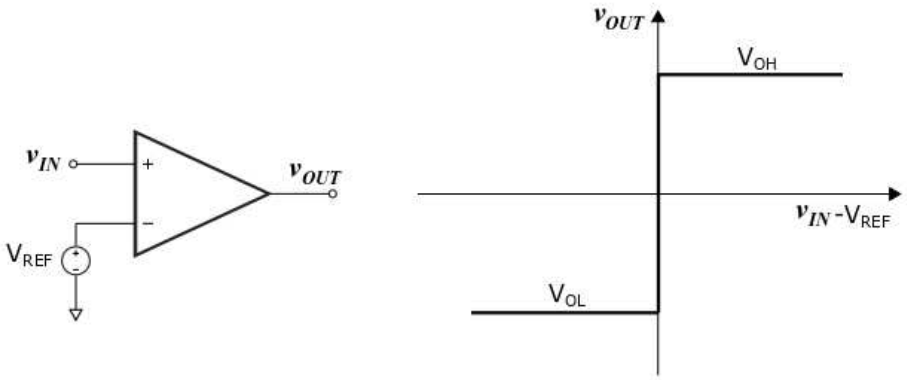

Figure 4.17: Circuit representation of the ideal comparator with its voltage transfer function

4.4.1.4 Comparator

The receiver output must interface with digital circuitry to demodulate the information. Usually, in CMOS technology, microcontrollers interpret binary data as 70% and 30% of the rail-to-rail dynamic [109]. Considering working with a microcontroller operating at 1.2 V, we must design the receiver having a maximum output level higher than 0.85 V. To do so, we can use comparators. There are two main categories of comparators: open-loop and regenerative comparators [109]. Open-loop comparators are amplifiers with no compensation feedback, whereas regenerative comparators use positive feedback to increase the resolution of the conversion. Regenerative comparators find applications in discrete-time conversions with high data rate sampling. The leadless synchronization we suggest requires a low data rate conversion, which is equal to the quenching period. Thus, it is convenient to reduce the complexity of the comparator designing an open-loop comparator. Moreover, a real-time comparison can retrieve the input amplitude information that would be lost using a discrete-time comparison. The amplitude information can give another degree of freedom to the microcontroller to demodulate input signals in noisy environments. We can ideally model a comparator as a differential amplifier with a reference voltage applied to the negative input terminal. As a result, the voltage transfer curve of the comparator can be represented by the voltage difference of the input terminals, as shown in Figure 4.17. Here, the output voltage of the comparator attains the high-value V_{OH} if the differential voltage is positive; otherwise, it attains the low-value V_{OL}. However, realistic output responses do have finite slope transition regions that determine the propagation delay of the comparator[109]. The propagation delay can limit the conversion rate. The propagation delay varies according to the input voltage level; the greater is the input, the faster is the response. For high input voltage levels, the conversion speed of the comparator comes from the slew rate of

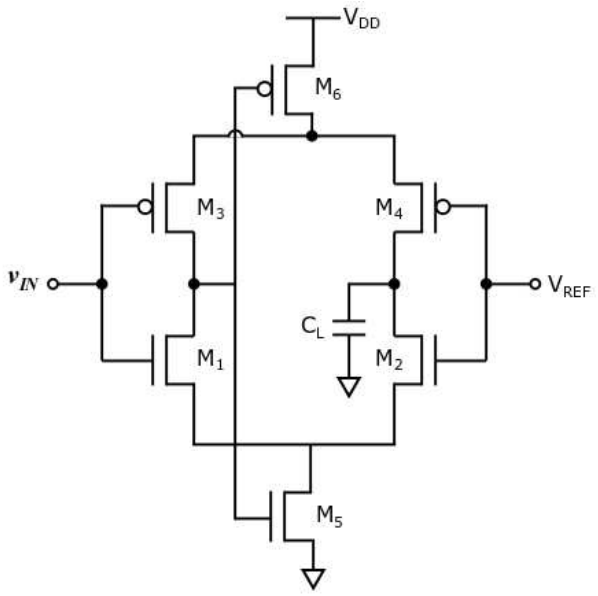

Figure 4.18: Self-biased comparator

the amplifier, which depends on the charge and discharge speed of the capacitive load. We can reduce the effect of slew rate, improving the sinking and sourcing properties of the output stage of the comparator. For our application, the incoming signal from the envelope detector has a limited frequency. Specifically, the frequency spectrum of the envelope signal will depend on the quenching frequency that is equal to 4 kHz. Thus, it is convenient to use comparator topologies suited to have high slew rates. The solution comes again from the inverter building block. As already seen in subsubsection 4.4.1.2, the inverter can sink and source large amounts of currents. In [118], *Bazes* proposes an elegant approach to have a self-biased architecture that can drive large capacitive loads. The differential amplifier consists of two inverter circuits respectively made by the transistor pairs M1-M3 and M2-M4. When the input voltage increases, the drain voltage of M_1 and M_3 drops to zero through M_6. As a result, M_6 turns on sourcing the output capacitance C_L. On the other hand, when v_{in} decreases, the drain voltage of M_1 and M_3, increases, turning off M_6 and letting M_5 to sink current from the load capacitor. The main advantage of this topology is that the circuit can source and sink high values of current with low quiescent consumption. The intrinsic threshold of the comparator is the input voltage of the transition region. To boost up the conversion, it is preferable to narrow the transition region of the inverter as much as possible. To do so, we used standard transistors instead of low power ones since they have higher values of threshold voltages. The DC component of the envelope signal is close to zero that would bias the n-MOS of the inverter deep in the cut-off region. In this condition, the output dynamic of the envelope signal will never reach the transition region imped-

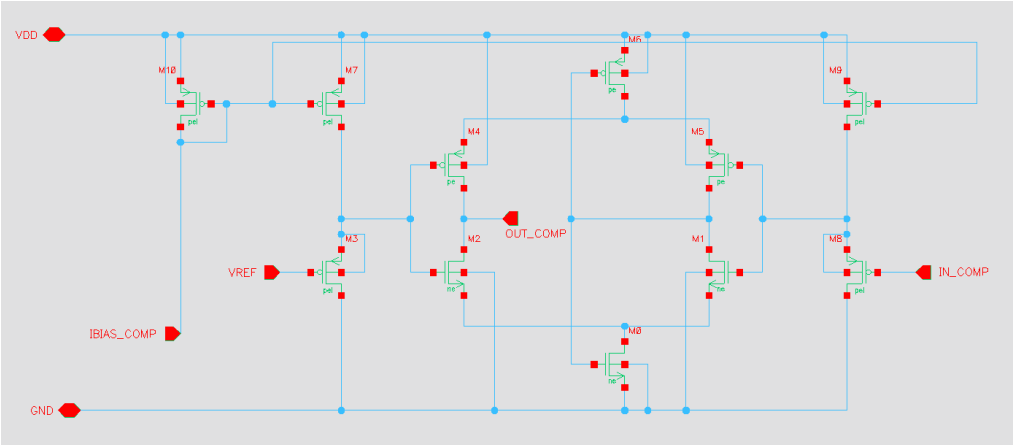

Figure 4.19: Proposed comparator circuit in Virtuoso© environment

ing the demodulation. To solve this issue, we shifted the DC level of the input and the reference signal through common-drain level-shifters [109]. Figure 4.19 shows the complete design of the proposed comparator, where the current mirrors M_{10}-$M_7/M9$ feed the voltage shifters of both V_{REF} and v_{in}. The common-drain shifter M_3 is not indispensable since we could consider to include the DC-level shift to V_{REF}. However, this additional branch preserves symmetry in the circuit, reducing the impact of PVT variations with the cost of a small additional current consumption. The whole block includes five terminals: two differential inputs (IN_COMP and VREF), the supply voltage VDD, the ground reference, and the output (OUTPUT_COMP). As previously done for the front-end amplifier, we simulated the comparator as a standalone building block. Figure 4.20 shows the test-bench of the comparator. We set VREF=100 mV through a DC-voltage source. We modeled the input of the comparator as a sinusoidal signal having an amplitude equal to 200 mV and a frequency of 4 kHz to resemble the transient response of the quenched oscillator. The output was loaded with a 40 fF capacitor to model the input of the digital interface. Figure 4.21 shows the transient response of a single comparison cycle, where the red dashed-line represents VREF, the green line is the input signal, and the yellow line is the output signal. The comparator gain was adapted to reduce the propagation delay of the comparator, achieving a value of 6.4 μs that is one order of magnitude lower than the reference clock of the Leadless pacemaker. The comparator was the last block of the receiver circuit we developed. Hereafter, we will see the performance of the whole receiver to see how these building blocks cooperate to achieve sensitive and power-efficient demodulation of OOK signals.

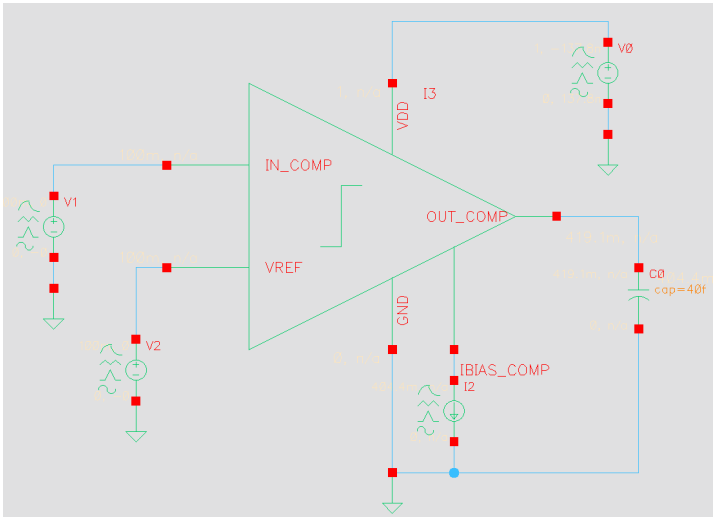

Figure 4.20: Testbench of the comparator building block

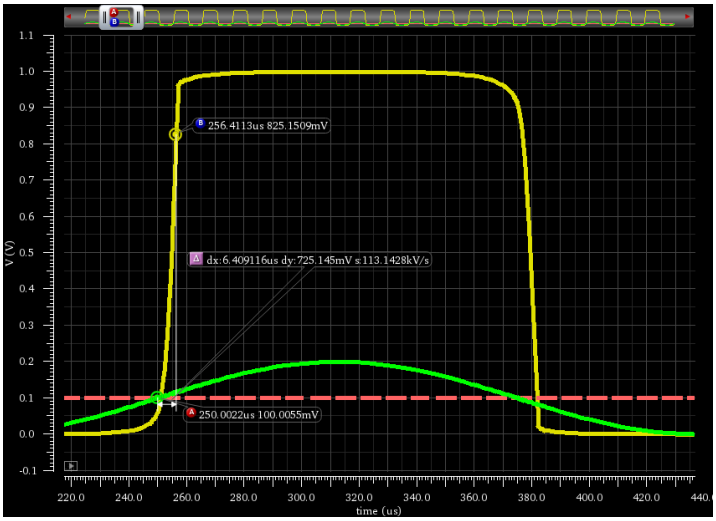

Figure 4.21: Output response of the self-biased comparator

4.5 SRR Simulation result

In the previous section, we have considered every single block of the Super-Regenerative receiver as a stand-alone entity. Here, we point out simulation results to see the performance of the whole architecture, which is represented in Figure 4.22. First, we will see the typical performance of the receiver stating the characteristic of the receiver such as sensitivity, Bit Error Rate (BER), receiver detection bandwidth, interference rejection,

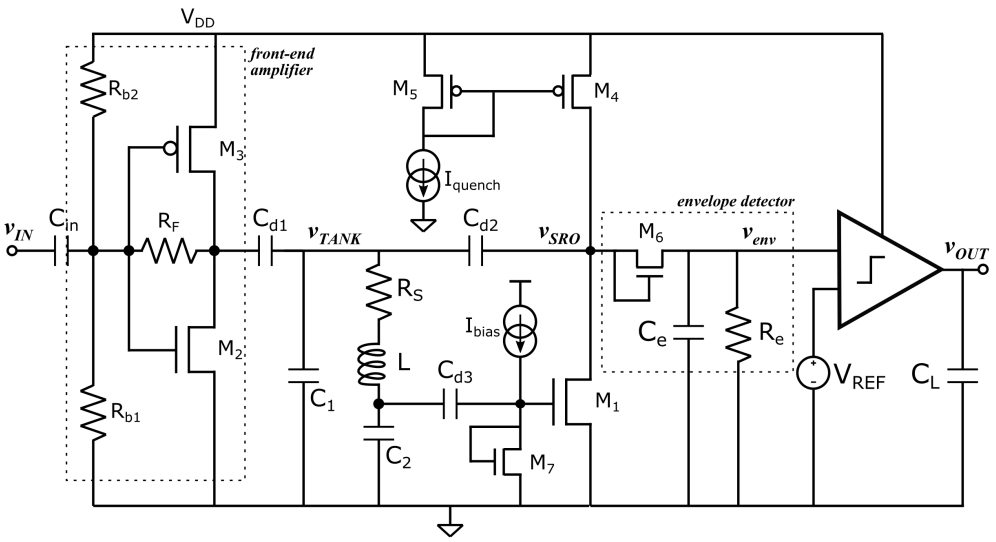

Figure 4.22: Schematic of the Receiver circuit

and power consumption. Many parameters of MOS transistors vary with temperature, making it challenging to operate across a wide temperature range [117]. However, leadless pacemakers are deep-implant biomedical devices, where the temperature range of operation must be moderate. We set the temperature of the reference simulation as the average temperature of the human body that is about 37°C [119]. However, in the last part of the section, we will analyze the reliability of the circuit design through simulation studies about the effect of the process, temperature, and voltage (PVT) variation.

4.5.1 Reference simulation

We performed reference simulations using typical values of MOS parameters given by the foundry. Figure 4.24 shows the testbench of the receiver. For the qualitative representation of the SRR characteristics, we will refer to subsection 4.3.1. For the sake of simplicity, let us recall (A.32) representing the output response of the SRR architecture:

$$v_o(t) = VK_0K_rK_sp(t)cos(\omega_0 t + \phi).$$

To achieve the required sensitivity, we tuned the regenerative gain K_r and the super-regenerative gain K_s without changing the front-end gain K_0, previously set to 22.5 dB. Specifically, this is obtained by acting on the time evolution of the damping function $\zeta(t)$. The time evolution of the damping function strictly depends on the real-time gain of the oscillator, which in turn depends on the quench signal.

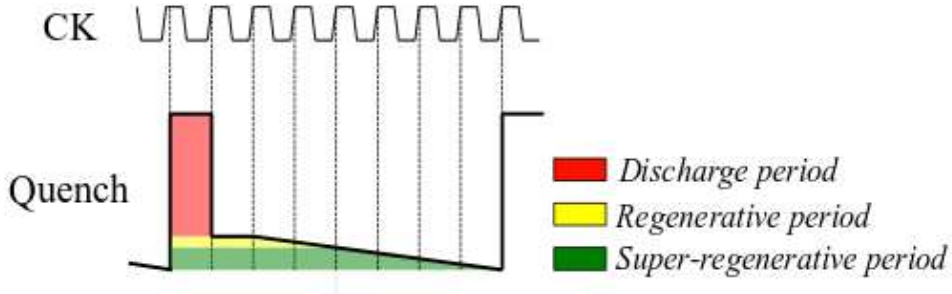

Figure 4.23: Time evolution of the quenching signal

4.5.1.1 Quench signal description

We decided to quench the oscillator through a variable current source. The p-MOS pair M4-M5 mirrors the quenching current to bias the common-source amplifier M1. We have seen that the quench signal must slowly change to improve the sensitivity of the SRR. On the other hand, the quenching must ensure full depletion of the charges stored in the tank to avoid intersymbol interference. To reduce the quench period, we suggest to face the dual task of the quench signal separately. Figure 4.23 shows the suggested waveform to quench the oscillator. It consists of a clock-driven signal that we can qualitatively divide into three regions:

- the discharge period used to deplete the capacitors of the tank circuit;
- the regenerative period used to initially charge the tank circuit according to the input signal coming from the front-end circuit;
- the super-regenerative period, where the oscillator is unstable, boosting the amplitude of the injected signal through the oscillatory response.

The whole quench signal spreads over eight clock cycles leading to a quenching period $T_{quench} = 250\mu s$. The discharge period lasts for one clock cycle and it is characterized by abrupt variation leading to a fast discharge of the selective circuit. In the next clock cycle, the quench signal passes from the discharge period to the regenerative period. Here, the gain of the amplifier is not sufficient to satisfy the gain condition of the oscillator, but it is high enough to neglect the damping of the injected signal. During the remaining six clock cycles, the quench signal decreases with a constant slope, crossing the critical value where the gain condition of the oscillator is satisfied. The oscillator output reaches its maximum value at the end of the super-regenerative period for the considerations we analyzed in subsection 4.3.1. Here, the output of the comparator can be sampled by the digital circuitry to demodulate the information. Let us recall the

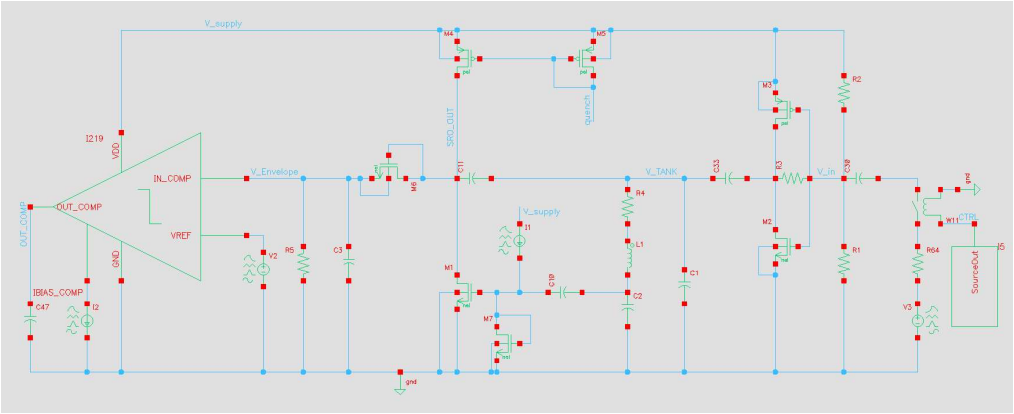

Figure 4.24: Test bench circuit of the proposed Super-Regenerative receiver

gain of the common source amplifier for a fixed gate-source voltage V_{GS}:

$$A(I_D) = -g_m(I_D) r_{out}(I_D).$$

We can modulate the damping function acting on the drain current of the M1. The highest peak of the quench signal corresponds to a null drain current of the common-source amplifier M1 giving to the tank circuit a low impedance pattern to the ground, allowing a fast discharging of the LC-circuit. Then, I_D is set to I_{start}, where M1 operates in the saturation region with a bias point close to VDS, sat, leading to a moderate output resistance. From the third clock cycle, I_D is linearly increased, reaching I_{stop} at the end of the super-regenerative period. In particular, we set I_{start} such that $A(I_{start})$ is slightly lower than the critical value. On the other hand, we set I_{stop} such that V_{DS} is lower than the threshold voltage of the diode of the envelope detector to avoid that the DC-bias point of oscillator dramatically contributes to the envelope detection.

4.5.1.2 Signal evolution through the receiver

Figure 4.25 shows the evolution of the OOK signal through the circuit. All the simulations performed included the thermal noise of the components to discriminate eventually false detections.

The peak amplitude of the input signal was set to 90 μV, which is slightly bigger than minimum expected voltage ($\sim 70\mu$V). The input level follows the oscillating response of the resonant circuit; however, the voltage levels are moderate, reaching a peak-to-peak voltage level of 700 μV. The voltage across the tank circuit (V_TANK) is an oscillating sinusoid that reaches saturation for a peak level of 300 mV with an almost null DC component. The maximum limit of V_TANK comes from the output dynamic of the Super-Regenerative oscillator, as can be seen, the signal SRO_OUT has the same peak-to-peak level as V_TANK. As soon as the oscillations rise, the voltage across the load of the envelope detector increases, reaching its maximum at 380 mV. This voltage

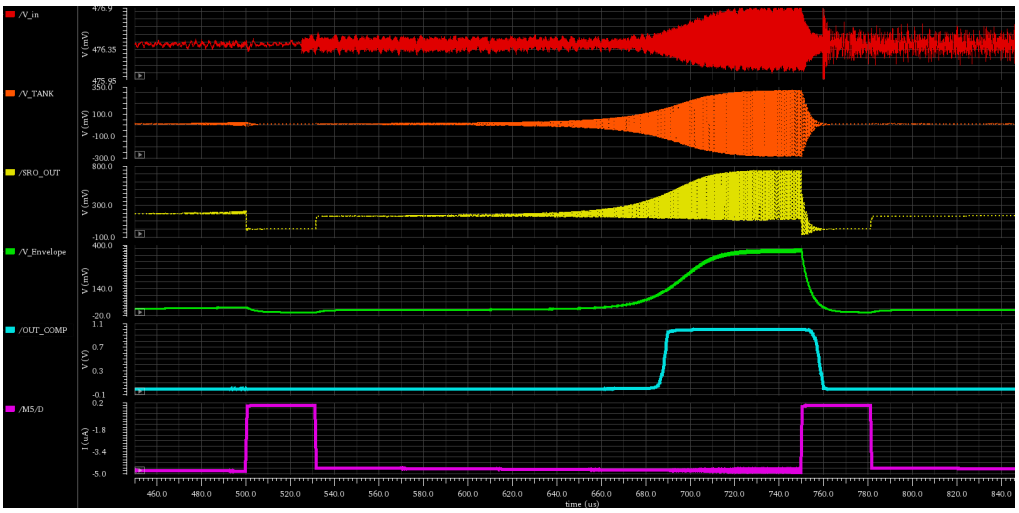

Figure 4.25: Time evolution of the input signal through the proposed receiver

level comes from the peak voltage of the oscillator output and a residual contribution of the time-varying DC point of the oscillator output. The output of the comparator (OUT_COMP) converts the low dynamic of SRO_OUT in a signal that is detectable by the binary logic of the digital circuit. The current signal of Figure 4.25 represents the quenching signal of the oscillator. The internal clock of the device drives the quenching current of the oscillator, as previously described. The output signal of the receiver rises almost 60 μs before the end of the quench cycle, allowing for relaxing the routing constraint of the clock signal to demodulate the information.

4.5.1.3 Sensitivity

We performed a parametric simulation of the input voltage to evaluate the sensitivity of the receiver. As can be seen in Figure 4.26, the minimum amplitude that is detectable by the receiver is about 10 μV. However, the time margin between the end of the quench cycle and the rise of the output signal lowers to 2 μs. Such a high sensitivity was achieved thanks to the regenerative gain of the SRR architecture. The total gain of the receiver can be retrieved as the ratio of the comparator output amplitude and the minimum detectable signal:

$$K = 20\log_{10}(\frac{V_{comp,out}}{v_{in}(min)}) = 100\ dB. \tag{4.78}$$

Considering that the maximum amplitude of the envelope detector reaches 370 mV, we can point out the gain of the comparator K_c and the oscillator gain K_{SRO} such as

$$K_{SRO} = K_{r,dB} + K_{s,dB} = 20\log_{10}(\frac{V_{SRO,sat}}{v_{in}(min)}) - K_{0,dB} = 68.8\ dB \tag{4.79}$$

$$K_c = K - K_{SRO} - K_0 = 9.3\ dB \tag{4.80}$$

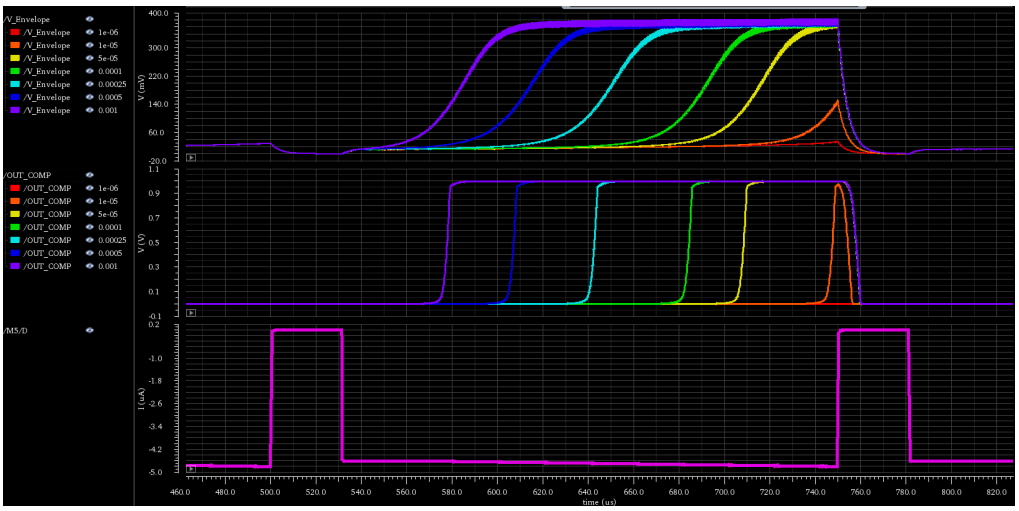

Figure 4.26: Output response of the parametric simulation with respect to the amplitude of the input signal

The proposed receiver circuitry respects the high sensitivity property of SRR architecture. At first glance, the receiver might not seem power-optimized concerning the sensitivity required. Here, it is worth reminding that this is the reference simulation performed with typical parameters of the MOS transistors leading to the best case scenario at 37°C. The minimum sensitivity was ensured over a broader temperature range as explained in subsubsection 4.5.2.1.

4.5.1.4 Detection bandwidth

Super-Regenerative receivers are very selective, increasing the robustness of the communication against interferers. On the other hand, extremely selective receivers require very low uncertainties of the components, needing high-resolution trimming of the selective network. To evaluate the bandwidth of the receiver, we performed a parametric simulation about the input signal frequency. The input amplitude was fixed to 90 μV since it is the minimum input signal expected for the intra-cardiac channel. The information was considered detectable as far as the output signal reaches V_H before quenching the oscillator. The frequency resolution of the simulation was set to 500 Hz, although Figure 4.27 shows only the response of the central frequency and the bandwidth limits. The receiver has a bandpass behavior centered at the resonant frequency $f_0 = 4$ MHz with a detection bandwidth of 13 kHz. As expected, the receiver is very selective. Let us define the relative detection bandwidth as

$$B = \frac{|f_0 - f_{H/L}|}{f_0} = \frac{\Delta f}{f_0} = 1.625\%, \tag{4.81}$$

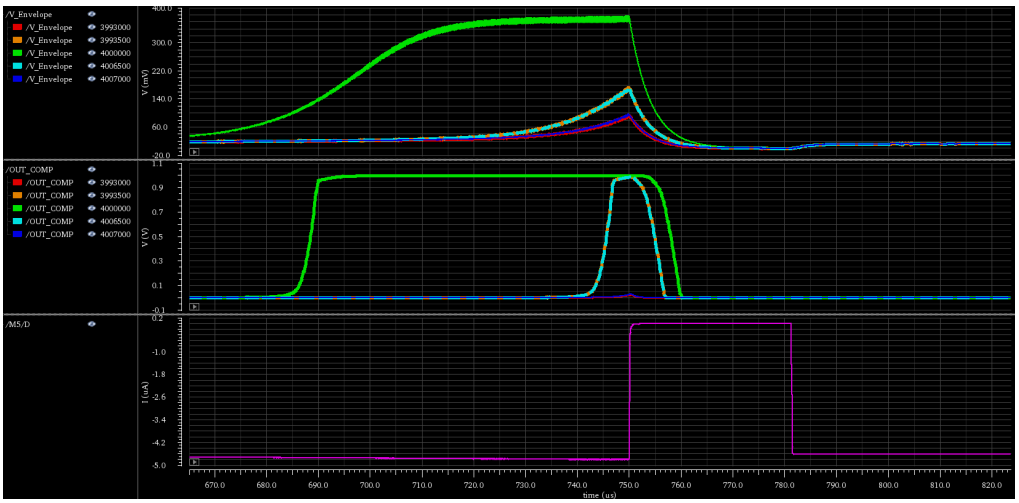

Figure 4.27: Output response of the parametric simulation with respect to the frequency of the input signal

where $f_{H/L}$ represents either the upper or the lower frequency limit of the detection bandwidth. B is related to the accuracy degree that the system requires to detect the information correctly. Indeed, the tolerance of the external inductor and the uncertainty of the integrated capacitors shift the resonance frequency f_0 such that

$$f_0' = f_0 \pm \delta_f.$$

As far as δ_f is lower than Δf, the receiver can detect the information. To achieve a resonant frequency with such a low uncertainty, we require to counteract the frequency shift, calibrating the capacitors of the tank circuit. However, in this analysis, we must consider the accuracy of both the emitter and the receiver. For example, let us consider receiving data from an emitter having a carrier frequency with the same uncertainty than the resonant frequency of the receiver; in this case, the value δ_f must be halved to ensure correct detections.
The integrated capacitors of the tank circuit have values of tens of pico-Farads. To achieve the accuracy required, we need a trimming network of capacitors with a resolution of the order of hundreds of fF, which is one order of magnitude bigger than the minimum integrable capacitance with the proposed CMOS technology.

4.5.1.5 Interference rejection

In the previous paragraph, we have evaluated the frequency response of the receiver finding out the detection bandwidth. Here, we intend to characterize another important feature: the robustness of the receiver to interferes. Let us define the interferers as signals whose frequency is out of the receiver detection bandwidth. Then, the interference

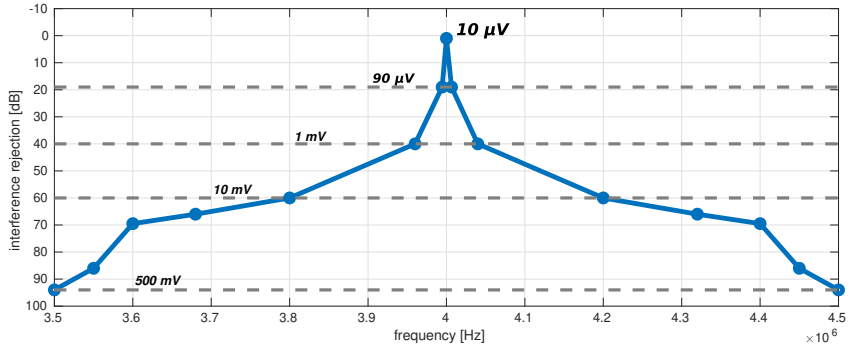

Figure 4.28: Normalized input sensitivity with respect to the resonance frequency.

rejection is the parameter describing the robustness of the receiver to interferers that are present in the radio-frequency spectrum. Quantitatively speaking, interference rejection is defined as

$$IR = \frac{v_{in,min}(\omega_0)}{v_{in,min}(\omega)}, \tag{4.82}$$

where $v_{in,min}$ represents the sensitivity of the receiver, which is the minimum input amplitude that can be detected by the receiver. Figure 4.28 shows sensitivity over a broad frequency spectrum. As can be seen, the receiver is very selective, achieving 60 dB of rejection for frequencies that differ only 200 kHz compared to the resonant frequency, corresponding to a relative difference of 5% from the central frequency of the selective network.

4.5.1.6 Bit Error Rate

The detection of the input signal depends on the incoming signal timing compared to the sensitivity period of the receiver, as explained in subsection 4.3.1. Thus, the input signal was modeled as an OOK signal with fixed pulse-width and variable period. The period was modeled as a stochastic variable with a gaussian distribution centered at $\mu = 3.33$ ms with a variance $\sigma^2 = 0.08\mu$. The variance was selected to limit the input period variation to 25%, according to the maximum acceleration of the sinoatrial activity. The mean value of the gaussian distribution μ was selected to have a reasonable computational time estimated to 24 hours. We performed a transient simulation of 34 s leading to a number of pulses

$$n \approx \frac{T_{sim}}{T_s} = \frac{34\ s}{3.333\ ms} \approx 10^4. \tag{4.83}$$

The result of the simulation experienced no missing detections ensuring a BER lower than 10^{-4}, which already ten times higher than the specification requirements. Moreover, no false detections were experienced as well, which is a nice property for Super-regenerative receivers. In fact, false detections would cause artificial disynchronization

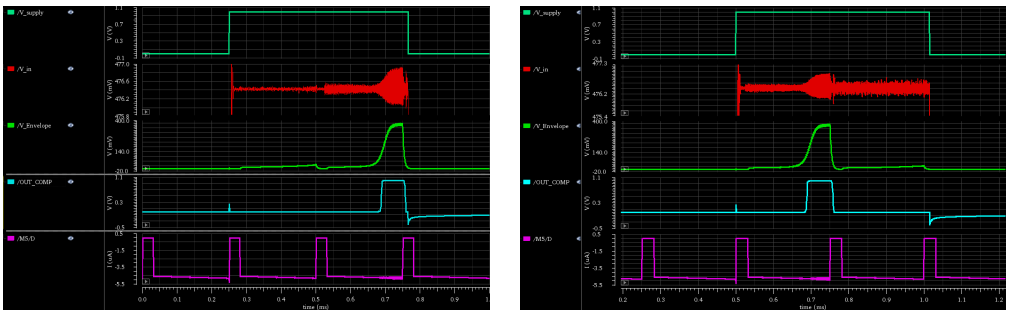

Figure 4.29: Transient analysis considering the start-up time of the receiver.

of the capsules preventing an efficient functioning of the system. The receiver achieves such a good performance in terms of BER thanks to the margin between the sensitivity and the noise level. Recalling the input noise spectral density $N_0 = -166,5dBv\sqrt{Hz}$, we can find the SNR of the receiver as

$$SNR = \frac{v_{in}(min)}{N_0 \times BW} = 25dB, \tag{4.84}$$

where BW is the detection bandwidth of the receiver that is equal to 13 kHz, as previously estimated.

4.5.1.7 Start-up time

Low-rate receivers usually do not work in continuous mode, but they are periodically activated to save current consumption during off-periods. The ratio of the on-time interval over one cycle period is known as *duty cycle*. For a fixed polling period, the lower the on-time, the higher is the power saved by the communication module. However, the active period must include the start-up time of the receiver to ensure that the receiver is functional when the emitter sends the information. The microprocessor is in charge of the activation of the receiver. Thus, to reduce the complexity, it is convenient to activate the receiver in phase with the discharge period of the quench signal. To do so, we substituted the DC voltage supply with a pulse generator having a pulse duration as long as twice the quenching signal for the consideration we pointed out in subsubsection 4.3.1.3. Figure 4.29 shows the two possible cases for the receiving of the information pulse. In Figure 4.29(left), the input signal occurs during the second quench cycle, whereas, in Figure 4.29(right), it occurs during the first quench cycle. There are infinite possibilities of input signal occurrence timing. We limited this study to these extreme cases to point out whether the receiver can correctly detect data without introducing false detections. As can be seen, when the supply voltage rises, the input of the front-end circuit rapidly reaches the stable condition imposed by the resistive bias-network of the LNTA before that the discharge period elapses. Even the comparator experiences a small perturbation caused by an initial inrush current flowing through the

output capacitor. However, the voltage level is small and cannot induce false detection.

4.5.1.8 Power consumption

Last but not least, we report the power consumption of the receiver. By definition, the power consumption of the circuit is given by the root mean square product between the supply voltage and the total current drawn. The supply voltage of the receiver is fixed and equal to 1 V. On the other hand, the current varies over time due to the current-driven quenching of the oscillator. Thus, the active power consumption of the proposed circuit can be found as

$$P_{active} = V_{supply} \cdot I_{RMS} = 18.25\ \mu W, \tag{4.85}$$

where I_{RMS} is the root mean square current drawn by the supply voltage generator. Here, we characterized the typical performances of the receiver through reference simulations. In the next subsection, we will evaluate how the receiver performances are impacted by PVT variations.

4.5.2 Process, voltage and temperature (PVT) variation

So far, we characterized the performance of the suggested receiver for typical conditions. However, CMOS components vary with the fabrication process, supply voltage, and ambient temperature. We denote these effects by PVT and design circuits such that their performance is acceptable for a specified range of PVT variations [117]. Those effects are tested separately to point out the effect of each variation over the typical performance of the receiver.

4.5.2.1 Temperature

The temperature dependence of MOS transistors is mainly related to the changes in the charge mobility and the threshold voltage [120, 121]. As a result, the drain current of transistors varies accordingly. The following equation quantifies the drain current considering temperature effect [109]:

$$I_D(T) = \frac{K}{2}\frac{W}{L}\left(\frac{T}{T_0}\right)^{-1.5}[V_{GS} - V_{th0} - \alpha(T - T_0)]^2, \tag{4.86}$$

where T_0 is the reference temperature in Kelvin, $V_{th0} = V_{th}(T_0)$, and α is an empirical coefficient that is positive for p-MOS and negative for n-MOS devices. Thus, to evaluate the effect of temperature variation, we launched a parametric analysis for a set of temperatures ranging in [27°C - 50°C]. We limited the analysis to such a moderate temperature range since the application targets deep-implant devices where the environment temperature must not extremely vary from 37°C. In particular, we considered as low temperature limit the room temperature of 300K (27°C) to have a reference

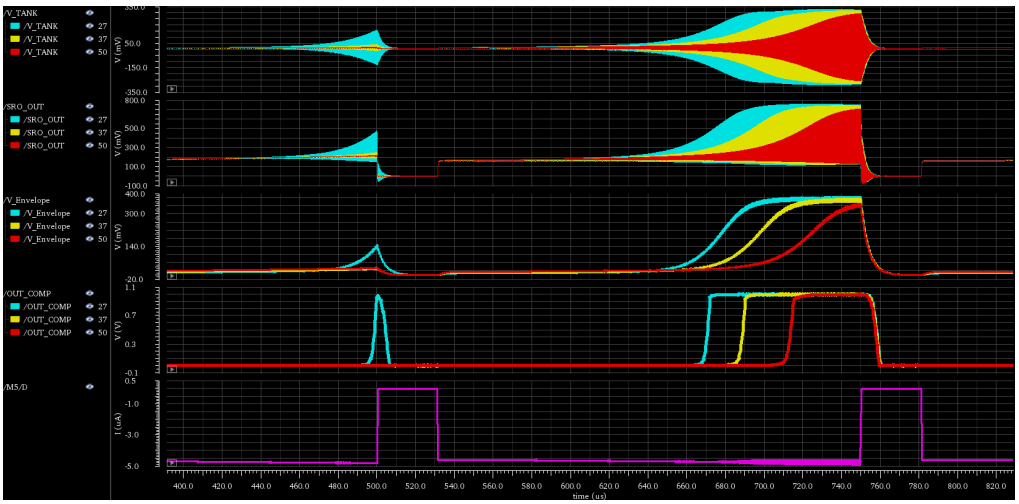

Figure 4.30: Results of a parametric simulation about temperature variation

for test-bench verification. On the other hand, we considered 50°C as maximum temperature to have some robustness margin that would consider the inner temperature gradient of the device. Figure 4.30 points out the evolution of the signals through the proposed super-regenerative receiver, where the light blue lines represent the signals at 27°; the yellow lines represent the signals at 37°, the red lines represent the signals at 50°, and the purple line is the quenching signal. As expected, the lower the temperature, the faster the saturation occurs, since the current drain controlling the gain of the oscillator increases according to (4.86). We designed M1 such that the output of the comparator reaches a stable value one clock cycle before the next quenching to increase the robustness of the demodulation.

4.5.2.2 Process

To evaluate the robustness of the receiver against process variations, we performed simulations using the corner libraries provided by the foundry. Such an evaluation, pointed out two main effects that require to be counteracted: the oscillator gain variation and the front-end input bias. To adjust the gain of the oscillator, we suggest to tune the DC point of the quench signal keeping the same slope of the ramp during the regenerative period. To do so, we only need to calibrate the I_{start} of the current drawn by the quench generator. The gain of the oscillator is given by the voltage gain of the n-MOS M1. Thus, Fast-n corners require lower values of I_{start}, whereas slow-n corners require higher value of I_{start}. The front-end circuit is based on a classical block used in digital circuits: the inverter. Thus, a particular behavior is expected by this circuit for Worst Zero and Worst One corner analysis. The voltage threshold mismatch among p-MOS and n-MOS devices makes challenging to keep the inverter-based amplifier in the transition region. However, it is possible to counteract the threshold voltage difference

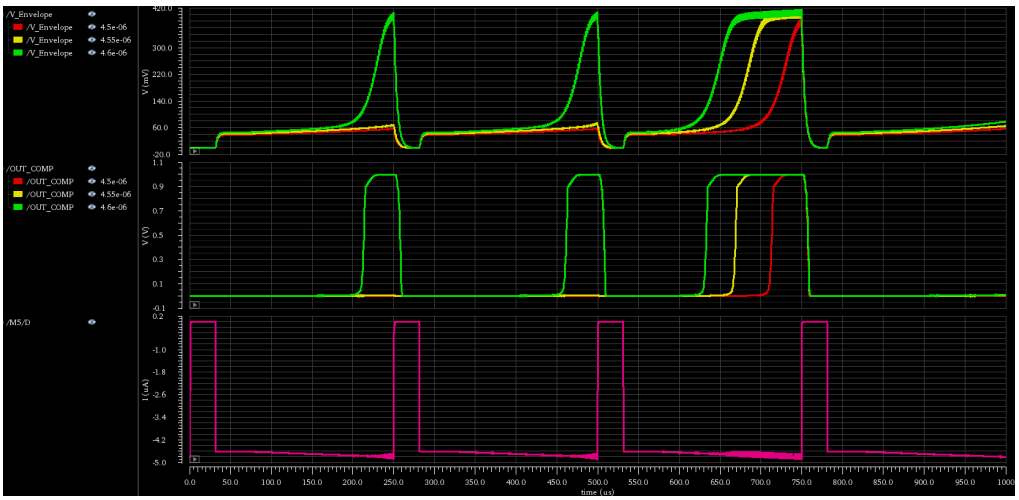

Figure 4.31: Simulation results of process-related variation (worst-power). A parametric simulation is shown acting on the initial current of the quench signal during the regenerative period

Table 4.3: Corner analysis

transistor model	I_{start}	**ΔR**	**Active Power**
Worst Power (fast n, fast p)	4.5 μA	0 Ω	36μW
Worst Speed (slow n, slow p)	4.7 μA	0 Ω	15μW
Worst One (fast n, slow p)	4.7 μA	-35 kΩ	18μW
Worst Zero (slow n, fast p)	4.7 μA	35 kΩ	18μW

acting on the gate-source voltage of the front-end devices. To do so, we suggest to trim the resistive network covering the maximum threshold change due to the process variation. Table 4.3 resumes the calibration required for every corner simulation to retrieve the same performance of the typical simulation. It is worth noting that the active power of the receiver is also impacted by the process variation almost doubling the power consumption for the worst-case scenario.

4.5.2.3 Voltage

Reference simulation was performed with a stable voltage supply. However, it is not straightforward to design DC voltage generators that do not vary with PVT variations. How does the suggested receiver work if the nominal supply voltage is shifted? To answer this question, we performed a parametric simulation varying the amplitude of the voltage supply. Figure 4.32 shows the results for relative variation up to 10% of the

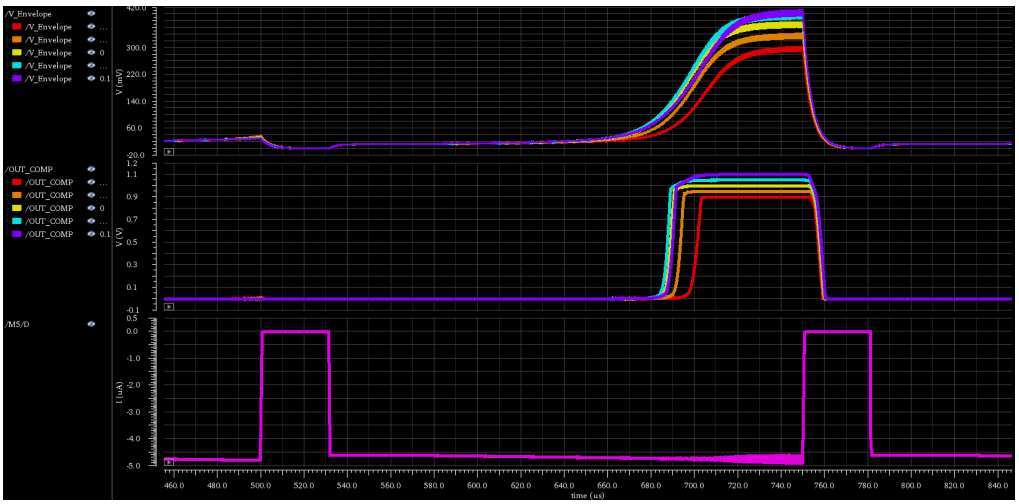

Figure 4.32: Simulation results of supply voltage variation.

nominal voltage. We set the variation limit considering more than 50 mV of margin from the analog value of the logic '1' signal (825 mV). For higher variation, even though the receiver can detect OOK signals, the detection would be limited by the intrinsic digital level of the binary information. As can be seen, the demodulation of the information is possible over the whole range of variation. The only effect that is reported is a slight increase of few μs to cross the reference voltage.

4.6 Conclusion

The atrioventricular synchronization of multi-node leadless pacemakers finds in the galvanic IBC a suitable technique for a telemetry-based solution. Indeed, capsules can send synchronization messages through the intra-cardiac channel. The synchronization is essential to adapt therapy stimulation to the physiological activity of patients and must occur each cardiac cycle with a maximum time uncertainty of 10 ms. Thus, although capsule synchronization does not require high data rate communication, it is the most challenging application in terms of average power consumption. The physical characteristic of galvanic IBC ensures robustness against eavesdroppers since a well-oriented direct contact with the patient is required to hack the communication. Thus, to minimize the complexity and the power consumption at the emitter side, we suggested using On-Off Keying (OOK) modulation. We performed a quantitative analysis of the maximum acceptable specification of OOK transceivers able to accomplish LCP synchronization. The most stringent constraint is the emitting voltage aiming to prevent interference with physiological neuronal activity. The higher the frequency, the lower the danger of perturbing the nervous system conduction. Thus, we suggest working in the MHz range. Low emitting voltages require receivers with high sensitivity. An ultra-

Table 4.4: Performance of the receiver designed

Parameter	**Our work**	**Cho2016**
Technology	180 nm	65 nm
Supply voltage	1 V	0.8 V
Frequency	4 MHz	13.56 MHz
Latency	250 µs	10 µs
Modulation	OOK	OOK
Data rate	2 kbps	100 kbps
BER	$< 10^{-4}$	10^{-5}
60 dB-Interference Rejection	$f_0 \pm 200\ kHz$	$f_0 \pm 6\ MHz$
Sensitivity	10 µV	1 µV
Power consumption	18.25µW	42.5µW

low-power architecture allowing detection of low input signals is the Super-Regenerative Receiver (SRR). This technique exploits the positive feedback of oscillators to reach incredibly high voltage gains minimizing the number of radio-frequency active blocks. We designed and simulated an SRR in 0.18 μm CMOS technology tailored for synchronization purposes.
It is not possible to compare exhaustively the suggested receiver to similar receivers of the state of the art due to the lack of scientific works in the literature.
We qualitatively compare our work with the super-regenerative receiver proposed by *Cho* in Table 4.4. Even though the receivers differ of several characteristics, the comparison can give a qualitative representation of the scientific results of our work. The main achievement of our design is the active power consumption, which is less than half the power of the circuit proposed by *Cho*. This result was obtained relaxing the constraints over data rate and sensitivity. It is worth pointing out that the maximum sensitivity of the receiver is still one order of magnitude lower than the worst-case input amplitude. Thus, it was convenient to improve the frequency selectivity achieving 60 dB of interference rejection two decades before compared to *Cho's* SRR.

Quantitatively speaking, the receiver consumes about 18 μW that is one order of magnitude higher than the maximum power budget allowed for the entire communication module. Thus, we should consider implementing an appropriate communication strategy to reduce the active time of the receiver, saving essential current to reduce the impact on the device longevity. In the next chapter, we detail a possible communication strategy allowing us to reduce the active power of the communication module dramatically.

5

Communication strategy

A multi-nodal leadless pacemaker system requires a communication network between the devices implanted in different heart chambers. The communication link aims to send physiological information such as EGM-event detections to deliver a synchronized therapy. Wireless communication approaches are power demanding reducing battery lifetime, which is a critical issue in permanent implants with limited battery capacity. In the previous chapter, we have seen that the Super-Regenerative Receiver can be an attractive solution for IBC intra-cardiac communication to demodulate low amplitude input signals. However, the active current drawn of the proposed circuit is still too high for continuous-time usage. Indeed, there is a need for smart strategies to reduce the duty cycle of the receiver and, consequently, its average power consumption. This chapter deals with a communication strategy for AV synchronization. The suggested algorithm is driven by the detection of the P-wave and can considerably reduce the power consumption of the receiver. According to clinical studies [122], the physiological heart rate does not accelerate by more than [25-35] % from beat to beat. Standard pacemakers have also the possibility to set a parameter for the beat to beat deceleration, which we will refer to as Δ_{pos}. Δ_{pos} reduces the artificial depolarization of cardiomyocytes and ranges from [0-30] % of the heart rate. Considering both the physiological acceleration and the allowed deceleration of the atrial activity, we find out that the P-wave information variability ranges in a time-window that varies from 25% and 65% of the heart-cycle duration. Even though we consider to turn on the receiver only during this amount of time, its power consumption would be extremely high compared to the LCP power budget.

5.1 Communication protocol description

In a healthy heart, the stimulation impulse propagates from the sinoatrial node of the RA to the ventricles, as described in chapter 2. However, electrical dysfunctions of

the conduction system can cause asynchrony to rise. Asynchrony among atrial and ventricular activity makes the heart functioning less effective. Dual-chamber pacemakers counteract the asynchrony between the RA and the RV, by adapting the RV-stimulation to the activity of the RA.
Let us now consider a leadless dual-chamber system. The capsule implanted in the RV requires the atrial activity information, such as the P-event detection of ECG sensors, to artificially synchronize the ventricular activity. Here, we focus on the communication protocol to synchronize LCPs, and we assume that EGM sensors are integrated in both devices to detect the local depolarization of the heart.
To artificially counteract chamber asynchrony, the RA capsule must send the timing information of the P-wave detection to the RV capsule. The communication protocol is driven by the RA capsule, which sends a synchronization pulse to the RV as soon as the P-wave detection occurs. To ensure a correct transmission of the information, the pulse-width of the synchronization signal is

$$T_{sync} = 2T_{quench} = 500\ \mu s, \tag{5.1}$$

where T_{quench} is the quenching period of the Super-Regenerative Receiver (SRR), proposed in chapter 4. Assuming to use the SRR, the RV capsule would consume 18 μW of power when the receiver is active. LCP devices have a limited power budget; thus, the RV capsule requires a strategy to reduce the listening time of the receiver. We suggest an adaptive listening window that exploits the periodicity property of P-wave events.
The RV capsule stores the timing information of the synchronization pulse when it correctly receives it. Otherwise, it sends a stimulation request to the RA capsule. The timing of previous synchronization pulses can be used to estimate the next P-wave event. Recalling that the maximum variability of physiological P-wave acceleration is 25%, we can reduce the listening window to

$$T_{RX} = 25\%HC + \Delta_{pos}, \tag{5.2}$$

where HC stands for the real-time heart cycle of the sinoatrial activity of the patient. For instance, considering a heart rate of 60 bpm and assuming to set $\Delta_{pos} = 0$, we would need a listening time equal to 250 ms, leading to a duty cycle of

$$DC_{RX} = \frac{T_{RX}}{1\ s} = 25\%. \tag{5.3}$$

In this condition, the average power consumption of the receiver is reduced by a factor 4, but it is still unreasonable compared to the total power budget of LCPs.
Let us now divide the synchronization issue into two separate aspects: the duty cycle reduction and the communication module synchronization. The next subsection focuses on a method to reduce the duty cycle of the SRR by one order of magnitude. Then we will see in subsection 5.1.2 the strategy to synchronize the communication modules with such a limited duty cycle.

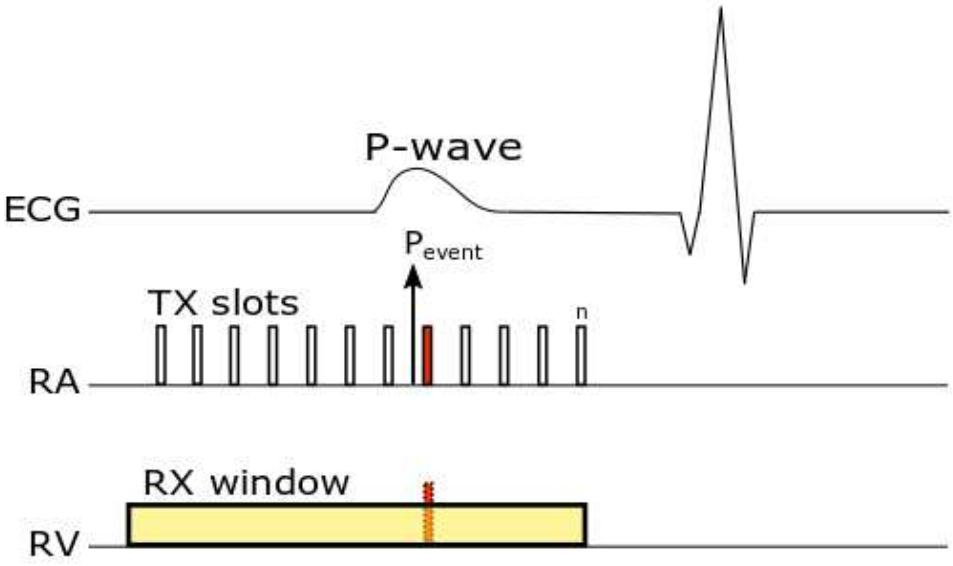

Figure 5.1: Communication-based synchronization of dual chamber LCP system

5.1.1 Duty cycle optimization for AV synchronization

Recalling that the LCP synchronization must occur with a maximum latency of 10 ms (see subsection 4.1.2), we can degrade the latency of the information transmission, reducing the duty cycle of the communication module.
Let us first evaluate the intrinsic propagation delay of the physical media. The speed v of the electrical propagation in the tissue is given by:

$$v \approx \frac{1}{\sqrt{\epsilon_{r,heart}\mu}} \approx 10^8 \ m/s \tag{5.4}$$

where $\epsilon_{r,heart}$ is the relative permittivity of the heart, according to *Gabriel's* studies [45]. We know that the Intra-cardiac channel length is almost $d = 10$ cm, which yields a propagation delay equal to:

$$t_{RX,delay} = \frac{d}{v} \approx 1 \ ns. \tag{5.5}$$

Thus, the propagation delay of the IBC signals can be considered negligible with respect to the digital clock reference, which is usually based on 32 kHz-quartz crystals [123].
As shown in chapter 4, the demodulation latency of the SRR depends on the quenching period. In the worst-case scenario, the synchronization pulse takes two quenching cycles to be demodulated, leading to a demodulation latency of ≈ 500 μs. Thus, there are still 9.5 ms of margin for the demodulation latency.
Here, we propose an event-driven communication that can occur during a predetermined

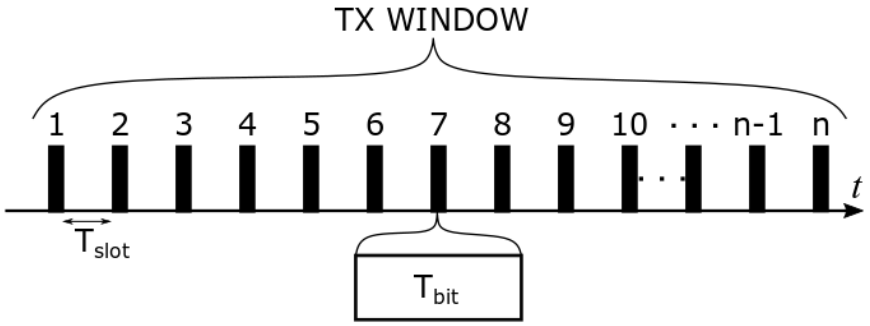

Figure 5.2: Sub-block representation of the emitter time-window

period. The basic concept is to map the physiologic period where the P-wave can occur into periodic sub-blocks where the communication can be enabled.
It is worth reminding that the P-wave acceleration is relative to the real-time heart rate. Thus, the number of sub-blocks must be adapted to the heart rate as well.
The time-window is composed of n periodic slots, covering the whole physiological time-window for both the emitter (RA capsule) and the receiver (RV capsule). Let us first consider the emitting slots of the RA capsule, represented in Figure 5.2. Each slot is equally spaced in time by T_{slot} and have duration pulse equal to T_{bit}. When the RA capsule detects the P-wave, it will use the first possible emitting slot of the TX window to send the synchronization pulse to the RV capsule. As previously said, $T_{bit} = 500\ \mu s$; then, to respect the latency constraint, the value of T_{slot} must be lower or equal to 9.5 ms. On the other hand, the RV capsule maps the physiological time-window into the same number of sub-blocks n, as depicted in Figure 5.3. Each sub-blocks is composed of a SLEEP-period and an ON-period. During the SLEEP-period, the main microcontroller of the device turns off the receiver, whereas, during the ON-period, it keeps it active. The ON-period must cover the starting time of the receiver, considering an appropriate margin to ensure the correct detection of the synchronization pulse. The number of slots n is given as the first integer number coming from the ratio between the physiological P-wave time-window and a single sub-block period (T_{sub}), as described by:

$$n = \frac{T_{RX}}{T_{sub}} = \frac{25\%HC + \Delta_{pos}}{T_{Sleep} + T_{ON}} \tag{5.6}$$

For example, if we consider having a heartbeat rate of 60 bpm with $\Delta_{pos} = 0$, the total physiological period is equal to 250 ms. Then, setting $T_{sleep} = 9\ ms$ and $T_{ON} = 1\ ms$, leads to n=25, reducing the overall listening time to 25 ms. Thus, the average power consumption of the receiver lowers of one order of magnitude, reaching an average current drawn of 450 nA. To further reduce receiver consumption during heartbeat acceleration, the receiver of the RV capsule could be disabled once the synchronization signal is received.

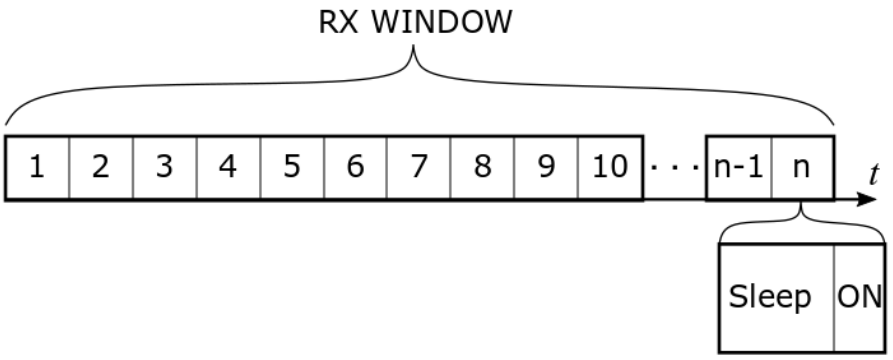

Figure 5.3: Sub-block representation of the receiver time-window

At the moment, we have considered only the duty cycle optimization according to maximum information latency. However, we still have to solve the capsule synchronization issue. Indeed, we need to synchronize the time-windows of the capsules to allow the correct transmission of the P-wave information between the LCP devices. To initiate the time windowing of the communication, which we will refer to as quasi-synchronized communication, we need to find a way to align the emitting and receiving slots of the two devices. Let us remind that cardiac events such as the P-wave are almost periodic in stable conditions. Then, it is possible after the first transmissions to estimate the next P-wave timing, which we will refer to as P_{est}. Both devices can independently perform the P-wave estimation and use P_{est} to center transmission windows. The following subsection describes the in detail synchronization methodology.

5.1.2 Communication window synchronization

We have seen that mapping the communication window in discrete slots can reduce the power consumption of the receiver of one order of magnitude, reaching power consumption levels that are feasible for the application. To ensure a correct transmission of the synchronization pulse, the capsules must have the same time reference, aligning the emitting and receiving slots. As we mentioned before, we suggest to take advantage of the periodic nature of physiological P-waves to adapt the communication slots.
Let us assume that the RA capsule detects a P-event, it will use the first slot after the detection to send a synchronization pulse. In particular, the first synchronization pulse is used to initiate the communication strategy for both the RA capsule and the RV capsule, setting to zero a reference timer. After initialization, the synchronization pulses are used to couple the RV capsule to the atrial activity. Figure 5.4 gives a graphical representation of the P wave detection transmission, where the RA capsule sends an OOK-modulated pulse with duration T_{bit}; whereas, the RV capsule senses the presence of the synchronization pulse through the SRR.

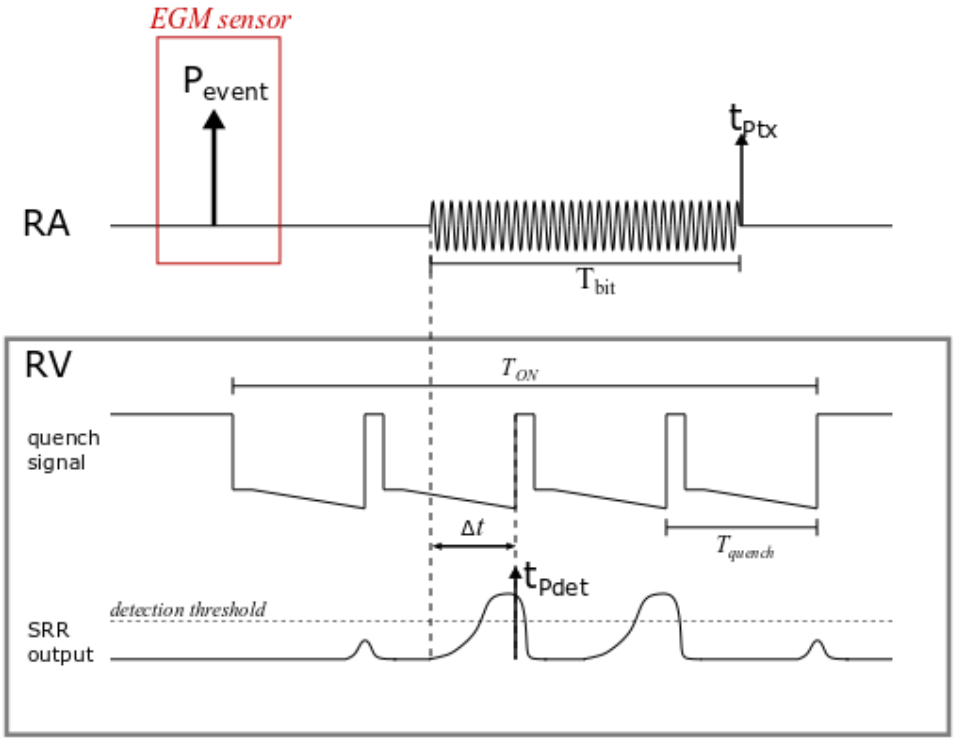

Figure 5.4: Transmission of the P-wave detection from the RA caspule to the RV capsule, using the SRR

The RA capsule stores the value of its reference timer PP_{tx} at the end of the transmission of the synchronization pulse t_{Ptx}. The RA capsule uses PP_{tx} to calculate the starting time of TX window for the next heart cycle.
During the first heart cycle, the RV capsule has no clue about whether and when the synchronization pulse can occur. Thus, the receiver is active all the time in a continuous way. As soon as the RV capsule detects the first synchronization pulse, it stores the value of its reference timer PP_{rx} at the detection timing t_{Pdet}. As a result, the time correlation between the time references of the capsules is given by:

$$PP_{rx,i} = PP_{tx,i} + (\Delta t_i - T_{bit}), \tag{5.7}$$

where i stands for the P-event number, and Δt_i is the demodulation delay for the i^{th} atrial event, which is strictly positive by definition. The next step is to estimate the timing of the next P-wave event using the heart cycle information, such that:

$$t_{Pest,RA} = t_{Ptx} + HC_{RA} \tag{5.8}$$

$$t_{Pest,RV} = t_{Pdet} + HC_{RV} = t_{Ptx} + (\Delta t_i - T_{bit}) + HC_{RV} = t_{Ptx} - \Delta T_i + HC_{RV}, \tag{5.9}$$

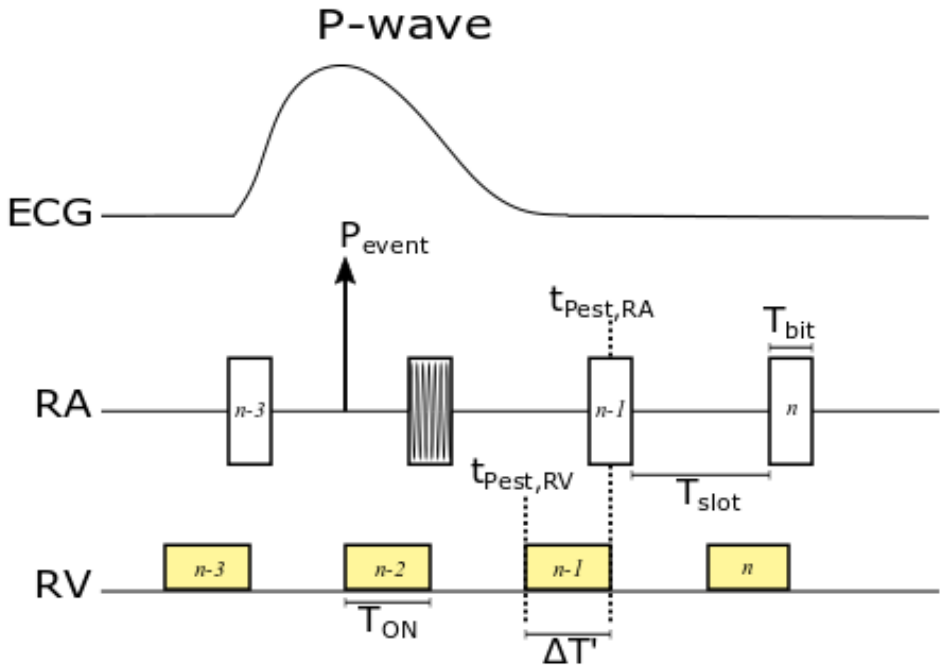

Figure 5.5: Representation of the main timing of the synchronization strategy

where ΔT_i represents the overall time difference between $P_{det,i}$ and P_{tx_i}. The value of ΔT_i depends on the demodulation delay of the SRR such that

$$0 < \Delta T_i < 250\ \mu s. \tag{5.10}$$

However, the value of the heart cycle estimated by the hemodynamic sensors could be different since they rely on local depolarization sensing. Indeed, HC_{RA} might differ of several milliseconds with respect to HC_{RV}, mismatching the communication slots. Thus, it is convenient to express (5.8) and (5.9) using only one independent variable. Once again, the nature of the information can help us to overcome this issue. Indeed, PP_{tx}, if correctly initiated, represents the PP-interval; thus, it can be used to estimate the heart cycle. It is convenient to calculate HC as the average of consecutive PP-intervals to increase the reliability of the measurement. For example, considering to estimate HC over two heart cycles we have

$$HC_{RA,i} = \frac{PP_{tx,i} + PP_{tx,i-1}}{2} \tag{5.11}$$

$$HC_{RV,i} = \frac{PP_{tx,i} - \Delta T_i + PP_{tx,i-1} - \Delta T_{i-1}}{2}. \tag{5.12}$$

Substituting (5.11) and (5.12) respectively in (5.8) and (5.9), the calculation of t_{Pest} resumes to:

$$t_{Pest,RA(i+1)} = t_{Ptx,i} + \frac{PP_{tx,i} + PP_{tx,i-1}}{2} = \frac{3PP_{tx,i} + PP_{tx,i-1}}{2} \tag{5.13}$$

$$t_{Pest,RV(i+1)} = (t_{Ptx,i} - \Delta T_i) + \frac{(PP_{tx,i} - \Delta T_i) + (PP_{tx,i-1} - \Delta T_{i-1})}{2} =$$

$$= t_{Pest,RA(i+1)} - \frac{3\Delta T_i + \Delta T_{i-1}}{2} = t_{Pest,RA(i+1)} - \Delta T'_{i+1}, \tag{5.14}$$

where $\Delta T'$ represents the overall time difference due to the demodulation latency.
For the sake of simplicity, let us consider the worst-case scenario, for which $\Delta T_i = T_{i-1} = 250\mu s$. In such a condition, the value of $\Delta T' = 500\ \mu s$. Considering a synchronization pulse with time duration $T_{bit} = 500\mu s$, the RX window requires sub-blocks with $T_{ON} = \Delta T'$ to ensure that the synchronization pulse totally covers at least one quench cycle of the SRR.

5.2 Algorithms for communication based dual chamber LCP system

In this section, all the algorithms used to implement the synchronization strategy are detailed. The RV capsule algorithm and the RA capsule one are considered as separate entities to resemble the real case scenario. Here, we assume that the devices can detect local depolarization events since all pacemakers embed hemodynamic sensors such as electrogram (EGM). The algorithms reuse the timing of previous synchronization signals to estimate the value of P_{est} and align the communication slots.

5.2.1 Synchronization algorithm of the RA capsule

Let us first consider the RA routine, represented in Figure 5.6. The device starts in the initialization phase to retrieve programmed information from the microcontroller. Moreover, during the initialization phase, the registers used for timing estimation can be reset. After the initialization step, the first synchronization events are sent asynchronously with a delay time less than 10 ms for the consideration previously reported. The microcontroller periodically checks the value of a counter to decide if the algorithm can move to the quasi-synchronized routine. If the value of the counter is less than *init*, the algorithm stays in the asynchronous routine; otherwise, it moves to the quasi-synchronized routine. The first step of the quasi-synchronized routine is the evaluation of the expected timing of the next P-wave (t_{Pest}). The value of t_{Pest} is updated each cardiac cycle as described in the previous section. Hereafter, we directly reference the labels of the algorithm steps of Figure 5.6 for the sake of clarity.
Moving forward through the algorithm, the detection of the P-wave is checked out (α)

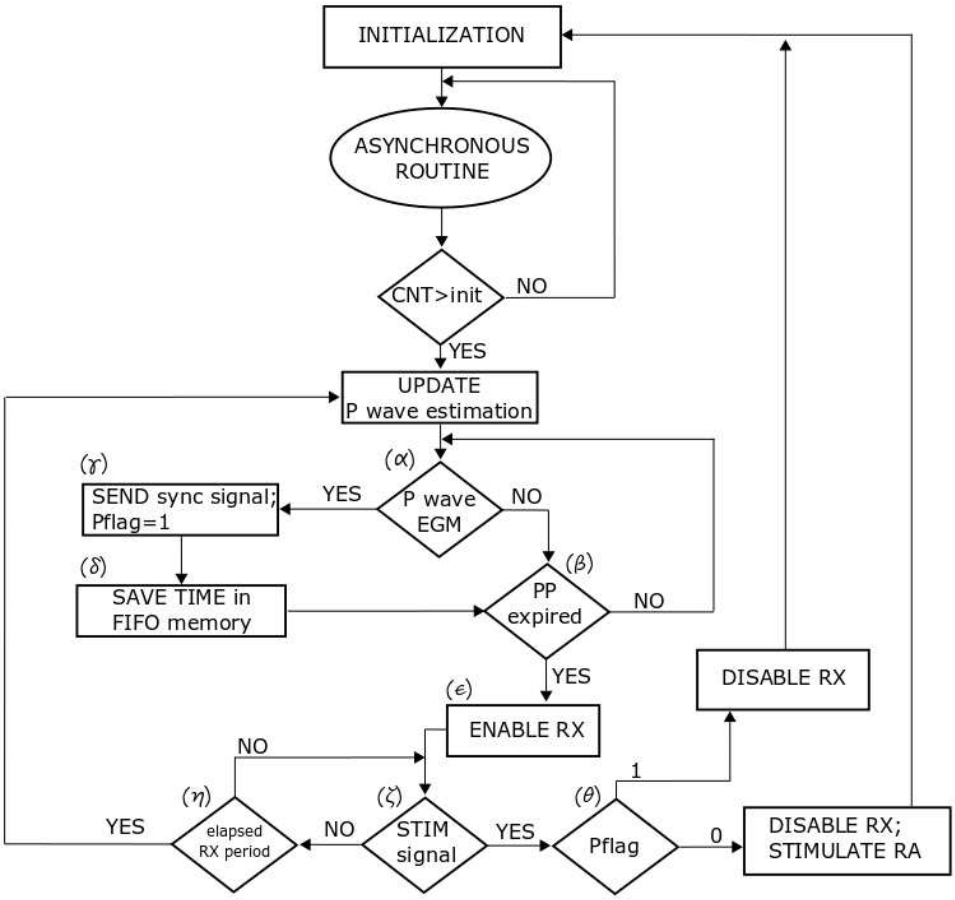

Figure 5.6: Synchronization algorithm for the RA capsule

during a predetermined period (β), which represents the maximum expected time between two consecutive P-waves. If a P-wave detection occurred, the RA capsule sends a synchronization pulse to the RV capsule and toggle the value of a flag register (γ). The RA capsule can use Pflag to take track of the correct emission of the synchronization pulse. Then, it stores the value of a time counter in a FIFO (First-In-First-Out) memory with length equal to *init* (δ). The values stored in the FIFO represents the time vector of P-wave transmission $PP_{tx}(n)$.

It is worth pointing out that the device retrieves the values of HC and t_{Pest} from the synchronization pulse timing that can differ from several milliseconds compared to the real P-wave detection performed using hemodynamic sensors. For this reason, HC and t_{Pest} values have no significance for medical diagnosis, and they are meaningful only for capsule synchronization purposes. Once that the EGM sensing period expires (β), the microcontroller enables the receiver (ϵ) for a predetermined time (η), the RX-period,

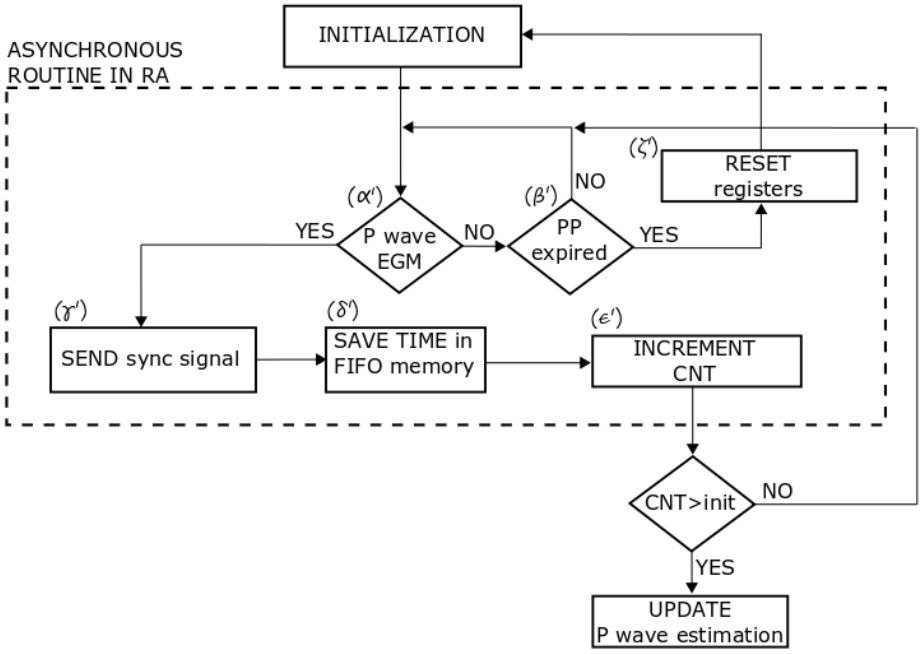

Figure 5.7: Asynchronous routine of the algorithm for the RA capsule

after a fixed delay from the last TX slot, as shown in Figure 5.10. During this amount of time, the RA capsule listens to the channel for stimulation orders coming from the RV capsule (ζ). If a stimulation order is detected (θ), the value of *Pflag* is used to discriminate stimulation orders ans transmission errors, i.e. the RV capsule does not correctly receive the synchronization signal from the RA capsule. Indeed, two possibilities are depending on the logical value of the *Pflag*:

1. $Pflag = 0$, the RA capsule disables its receiver and delivers a stimulation pulse to depolarize the RA

2. $Pflag = 1$, the RA capsule inhibits the stimulation and reinitializes the algorithm.

If no synchronization pulses are received, the algorithm starts again from the calculation of t_{Pest}.

Let us now zoom in the asynchronous routine of the RA capsule (Figure 5.7). In this routine, the RA capsule sends a synchronization pulse (γ') after the P wave detection (α'). As previously described for the quasi-synchronous algorithm, the RA capsule stores the value of the time counter in the FIFO memory (δ'). The value of an incremental counter takes track of the number of P-wave events (ϵ'). If the value of the counter is higher than *init* (e.g. init=3), the RA capsule leaves the asynchronous routine for the quasi-synchronous one. A reset state is included in the asynchronous routine of the

RA capsule to set the FIFO registers to zero in case a P-wave was missed during the firsts PP-intervals (ζ'). This ensures that the variables used for the quasi-synchronous algorithm (t_{Pest} and HC) are calculated in stable conditions.

5.2.2 Synchronization algorithm of the RV capsule

Let us now consider the algorithm embedded in the RV capsule, represented in Figure 5.9. As previously described for the RA capsule, also the RV algorithm starts with an initialization state. After the initialization state, the RV asynchronous routine is started. A detailed representation of the RV asynchronous routine is given in Figure 5.8. The first step of the asynchronous routine is to switch on the receiver (α'). If a synchronization signal is received (β'), the capsule saves the value of a time counter in a FIFO memory (δ'), as previously done for the RA capsule.

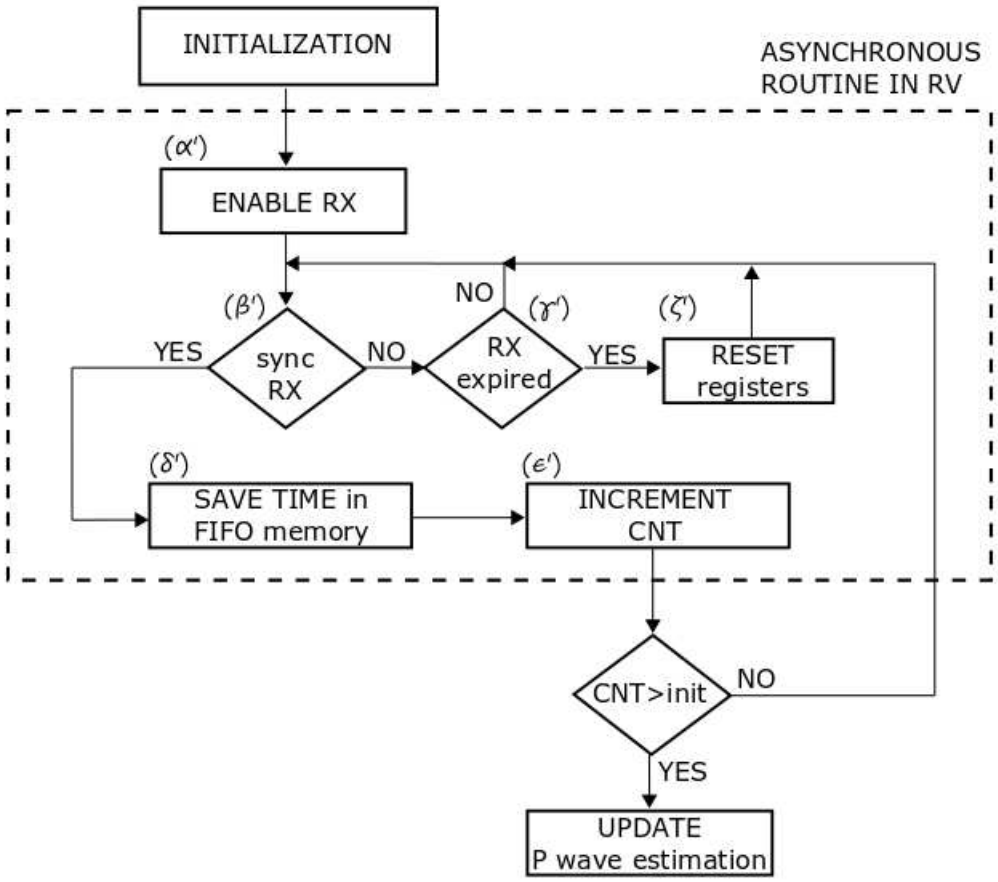

Figure 5.8: Asynchronous routine of the algorithm for the RV capsule

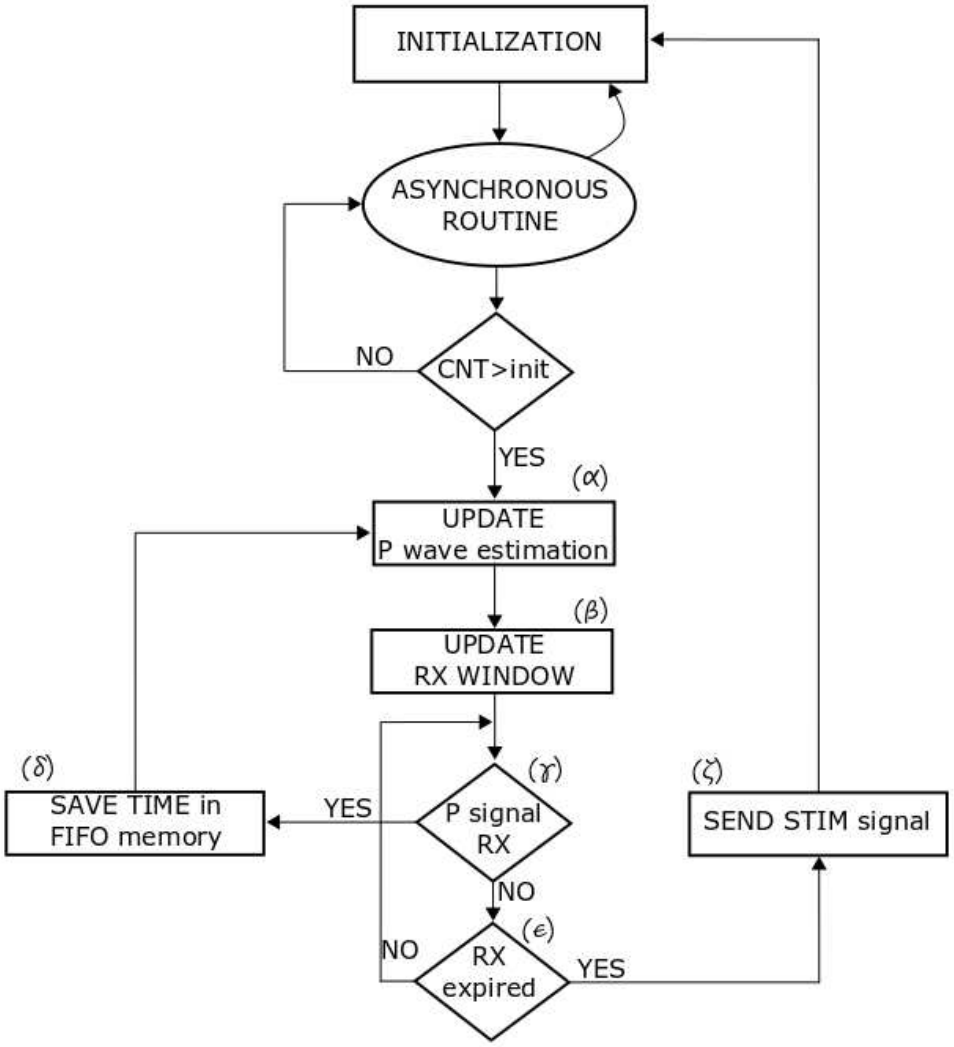

Figure 5.9: Synchronization algorithm for the RV capsule

Then, the RV capsule increments the value of a counter register (ϵ') and compares it to the threshold value *init*. If the value of the counter is higher than *init*, the RV capsule is ready for the quasi-synchronous routine. It is worth pointing out that the threshold value of the counters of the RV and the RA capsule must be equal to start the quasi-synchronous routine during the same cardiac cycle in both devices. Let us now focus the attention on the quasi-synchronous routine. The first step of the quasi-synchronous routine is to calculate t_{Pest} using the values stored in the FIFO memory (α). The RV capsule uses $t_{Pest}(n)$ to center the RX-Window (β), as shown in Figure 5.10. In the RX-Window, the receiver is periodically in ON-state. If a synchronization signal is received (γ), the RV capsule updates the FIFO memory with the value of the time counter

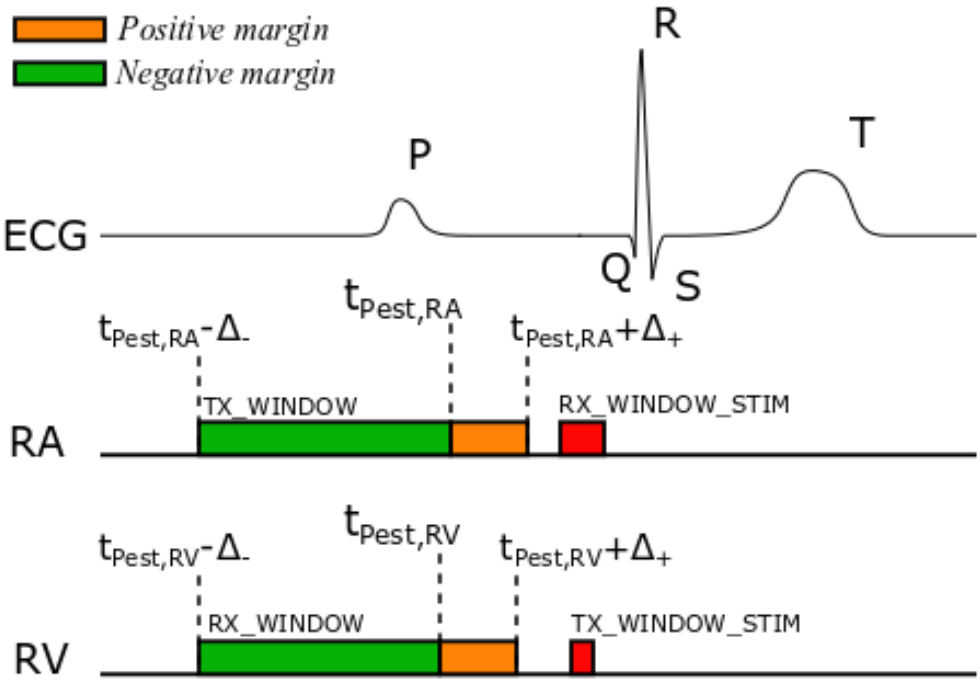

Figure 5.10: Communication window for synchronization purposes

(δ), and the algorithm restarts from the calculation of t_{Pest} (α). On the other hand, if no synchronization signals are received, the RV capsule sends a stimulation signal (ζ) after a fixed delay time from the last RX slot. Then, the algorithm restarts from the initialization phase to re-perform the asynchronous routine. This communication strategy allows synchronizing the therapy of LCP capsules saving a considerable amount of energy.

5.3 Digital circuit implementation

In the previous section, we pointed out the sequential actions that the RV and the RA capsules must perform to establish the suggested communication strategy. The key of the whole strategy is the prediction of the P-wave: each cardiac cycle, the LCP estimates the PP-interval leading to the prediction of the next P-wave timing t_{Pest}. The value of t_{Pest} is important for a dual scope:

- to reduce the overall communication window;
- to have a reliable time reference among the capsules.

Indeed, t_{Pest} is used to set the number and the timing of the periodic communication slots. Thus, the calculation of t_{Pest} must be performed in both the RA and the RV

capsules. Here, we propose a possible implementation which calculates the time-interval leading to t_{Pest} and all the variables that are meaningful to manage the communication module. For the sake of simplicity, the calculation of t_{Pest} will be performed averaging the heart cycle over only 2 events, as described in (5.13) and (5.14).
Low power systems, such as pacemakers, require managing with parsimony the active time of the execution units of the micro-controller [124]. Thus, it is convenient to implement the calculation of the time reference in hardware, instead of using software based solutions.
We suggest to calculate the reference for the communication module through a digital circuit, which works at the low frequency reference of the pacemaker.
Hereafter, we divide the description of the suggested piece of hardware into two subsections. The first subsection describes the data-path of the hardware, pointing out the functional units, the inputs and the output signals; whereas the second subsection deals with the time analysis of the circuit, pointing out the control signals that must be driven by the control unit of the pacemaker.

5.3.1 Digital circuit description

This subsection describes the calculation unit estimating the next PP-interval to activate the communication module. In particular, the output PP_{trx} is intended as the delay-interval before activating the communication module from the last synchronization pulse. Moreover, the circuitry is able to monitor the evolution of the PP-interval. In particular, the output signal *stable* informs the control unit that the PP-interval does not exceed the maximum physiological change of 25%. Figure 5.11 shows the schematic of the proposed data-path, whose sequential logic part is composed of

- One timer, to calculate the PP-interval each cardiac cycle;
- Five registers, to store the previous PP-interval and the arithmetic results.

On the other hand, the combinational logic part is composed of

- Three multiplexers (MUX), to regulate the internal signal traffic toward the adder;
- One adder, to perform arithmetic addition;
- One inverter, to change sign of the operator whenever subtractions are required;
- One absolute value converter
- One digital comparator, to check that the acceleration of the PP-interval is lower than 25%.

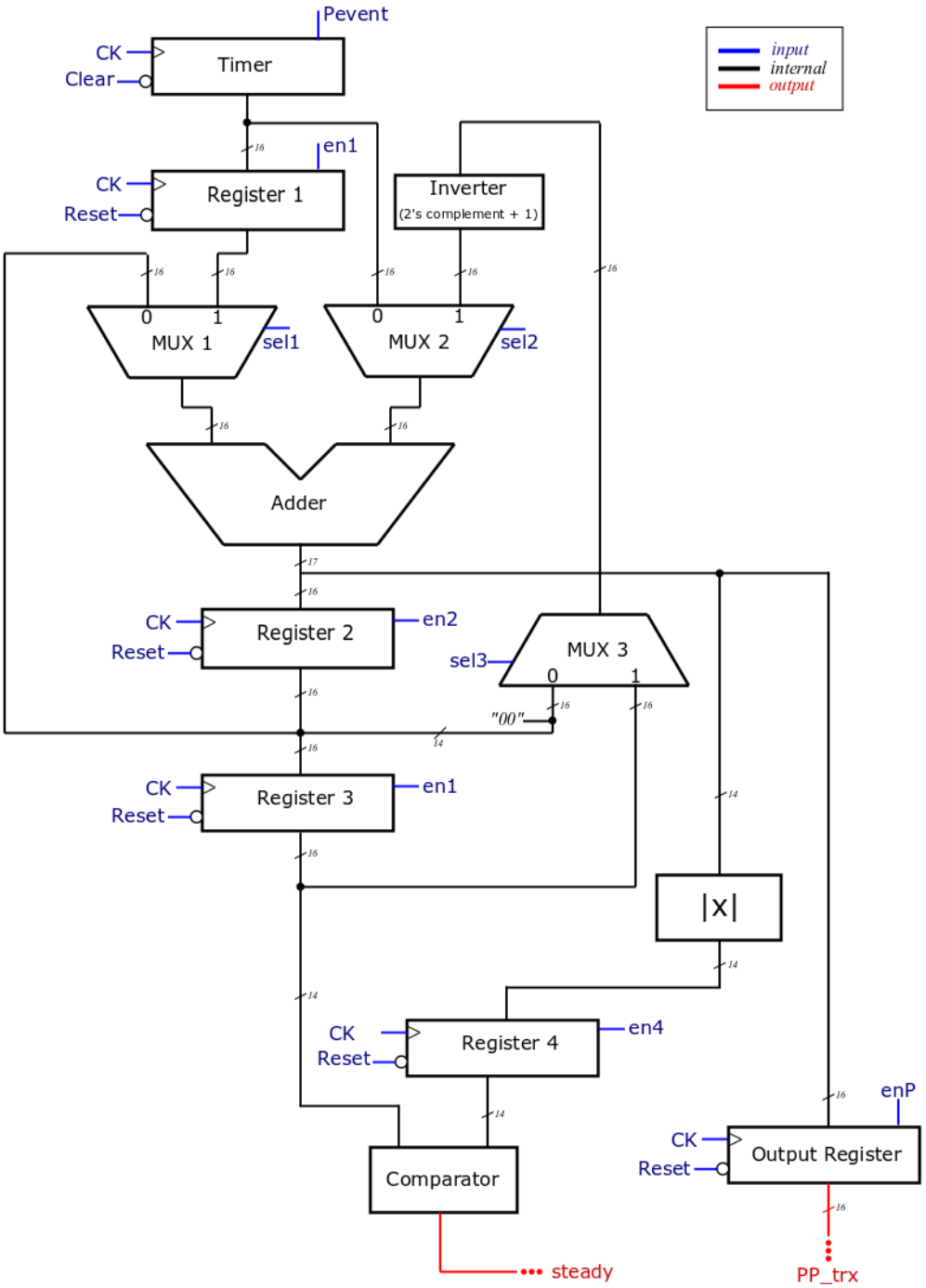

Figure 5.11: Datapath of for the calculation of the delay interval for the communication module.

Let us focus on each functional block to understand its role for the evaluation of the output signals.
The timer was designed as a 16-bit up-counter that increments its value at each cardiac cycle, limiting the maximum acceptable PP-interval to

$$PP_{max} = T_{CK} \times 2^{16} \approx 2 \ s, \tag{5.15}$$

which is an acceptable limit for the application since it would lead to heart rates of ≈ 30 bpm, which is lower than the minimum physiological heart rate of athletes at rest (40 bpm) [125].
Register 1 stores the value of the timer to keep track of the PP-interval for the next cardiac cycle. The adder has two 16-bit inputs and a 17-bit output to prevent overflow issues. The output of the adder is connected to three different blocks: the register 2, the absolute value converter, and the output register. Register 2 stores the 16 Most-Significant Bits (MSB) of the adder output. This operation allows storing the average of the sum directly. Indeed, register 2 is used to evaluate the average of the heart cycle such as

$$HC = \frac{PP_{tx,l} + PP_{tx,l-1}}{2},$$

where $PP_{tx,l}$ and $PP_{tx,l-1}$ are the P-wave intervals stored respectively in the timer and in register 1.
Register 3 stores the output of register 2 to keep track of the HC during the next event. To verify that the patient heart rate is in stable condition, we must check that the P-wave acceleration respects the physiological limit of 25%. To do so, the combinational logic performs the difference between the two last heart cycles that are stored in register 3 and register 2. The absolute value of this operation ΔPP is stored in register 4. Once that register 3 is updated, the digital comparator checks that the time difference between the last two PP-intervals is lower than 25%, comparing ΔPP and the 14 MSB of the register 3. The heart rate stability information is encoded on the signal *stable* that interfaces the control unit directly. Finally, the delay interval PP_{trx} for the RX window is calculated as

$$PP_{trx} = PP_i - 25\%P_i = 75\%P_i \tag{5.16}$$

The output register stores the value of PP_{est}, which is used by the control unit to manage the activation of the communication module.
To control the whole circuitry, the data-path requires 10 input signals:

1. CK, a 32 kHz clock;
2. Reset, a global signal to clear all the registers;
3. Clear, to reinitialize the timer.
4. Pevent, an enabling signal for the timer;
5. en1, to enable register 1 and register 3;

6. en2, to enable register 2;
7. en4, to enable register 4;
8. enP, to enable the output register;
9. sel1, to select the output signal of MUX 1;
10. sel2, to select the output signal of MUX 2;
11. sel3, to select the output signal of MUX 3.

In the next subsection, we will focus the attention on the time evolution of the data-path signals.

5.3.2 Time evolution of digital signals

Figure 5.12 represents the time-diagram of the proposed schematic, where the timing of the signals is synchronous with the clock. During the initialization phase (t=0), the control unit must set all the registers and the timer to 0 using respectively the signal *Reset* and the signal *Clear*. After the initialization phase, the control unit enables the timer through the signal *Pevent*, whose activation is dependent on the P-wave transmission timing. The second P-wave transmission disables the timer for three clock cycles representing the first event routine. During the first event routine, the value of the timer is stored in register 1 (*reg 1*) before being cleared and reactivated again. The timer keeps counting until a second P-wave event occurs. The adder sums up the value of the timer and the register 1, and its 16 MSB are stored in register 2. Once the average of PP-interval is stored, the registers 1 and 3 are updated and the timer is cleared and activated again. At the third P-event, the control unit updates the PP-interval average in register 2 during the first clock cycle. Then, the difference between register 2 and register 3 is performed, whose absolute value (ΔPP) is stored in register 4. Subsequently, to evaluate the heart rate stability, the combinational circuit performs the difference between the real-time heart cycle, stored in register 2, and the previous one, stored in register 3. The control unit enables register 4 to store the absolute value of the difference (ΔPP) in register 4, enabling the acquisition. During the next clock cycle, it updates register 3. The comparator is now able to check whether the real-time PP-interval is physiological. For simplicity, in this implementation, we limited the physiological acceleration to 25% of the heart rate. We have seen in the previous subsection that the data-path intrinsically performs a binary division by four feeding the comparator with only the 14 MSB of register 3, which stands for 25% of the real-time PP-interval.
If the value of register 4 is lower than the 14 MSB of register 3, the output signal *steady* rises to 1. This signal informs the control unit that a stable atrial activity is detected, and the device can start the quasi-synchronous communication. Finally the control unit enables the output register to store the next delay interval for the activation of the

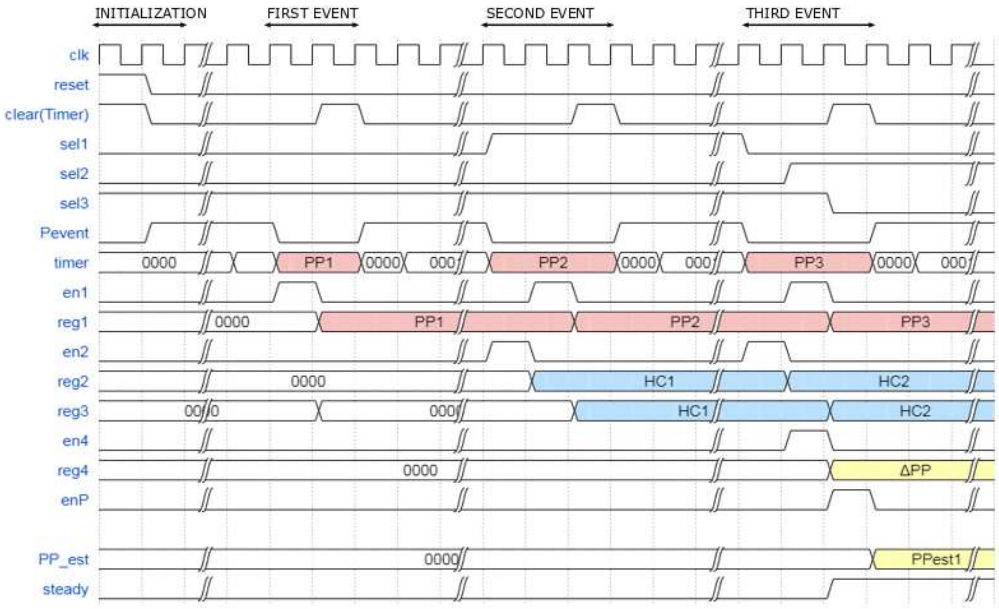

Figure 5.12: time diagram for the P wave estimation

communication module.

Here, we have pointed out how to drive the control signals to manage the datapath for the evaluation of the communication intervals. The total power consumption of digital circuits per device $P_{digital}$ is the sum of a dynamic component P_{dyn} from charging and discharging the parasitic output capacitor C_L and a static component from the leakage current I_{off} [124] such that

$$P_{digital} = P_{dyn} + P_{stat} = \frac{sr}{2} f_{clock} C_L V_{DD}^2 + I_{off} V_{DD}, \tag{5.17}$$

where sr is the switching rate, V_{DD} is the supply voltage. We suggest to drive the control signals through a FSM instead of using the main microcontroller to work at the low frequency reference of the pacemaker, ie f_{clock}=32 kHz. Since each P-wave event is processed in few clock cycles, we can consider that the dynamic power consumption will not weigh on the power budget of the communication module. Moreover, this circuit is intended to be integrated with the same technology of the receiver, which is a relatively large technology (0.18μm) having low leakage currents. Thus, the total power consumption of the digital circuit can be considered negligible compared to the receiver block.

5.4 Discussion

In chapter 4, we proposed an ultra-low power solution tailored for the intra-cardiac channel. However, the sensitivity requirement limited the minimum power consumption of the receiver. Even though the receiver consumption was reduced by more than a factor 2 compared to state of the art, the active power consumption of the circuitry prevents a continuous-time functioning of the communication module. The time variability of the P-wave signal makes standard pollings of the receiver insufficient. In this chapter, we suggested a simple solution to reduce the average power consumption down to 2% of its active power. The stochastic nature of the physiologic P-wave does depend on its previous value. In particular, PP-intervals should not exceed a beat-to-beat acceleration of [25-35]%. Physicians consider Sinoatrial activity accelerations faster than 25% as supraventricular tachyarrhythmia events. In this case, AV synchronization must be avoided preventing a dangerous ventricular tachyarrhythmia.
The proposed algorithm tracks previous PP-intervals to map sub-windows over the whole physiological variability period. Thanks to this method, we can synchronize heart chambers in a power efficient way. The active power consumption adapts to the heart rate making the average power consumption constant over time.
Thanks to the reduction of the duty cycle, the receiver achieves an average power consumption as low as 340 nW. To guarantee the same longevity of a single chamber LCP, for example 10 years, we would need an additive charge equal to

$$Q_{(mAh)} = \frac{I_{av}}{10 \times 365 \times 24} \approx 30\ mAh \tag{5.18}$$

The effort of this slight increase in battery capacity is rewarded with a continuous-time AV-synchrony, improving the hemodynamic of patients [126].
Pacemaker patients can experience supraventricular arrhythmia. In one embodiment of the proposed strategy, the right atrium capsule can send a disable message to decouple the functioning of the right ventricle capsule. In this condition, the right ventricle device works as a standard VVI pacemaker. The RA capsule monitors the evolution of the atrial arrhythmia event using standard hemodynamic sensors such as EGM. When the RA capsule detects the reestablishment of physiological atrial activity, it restores the AV-synchrony using an enabling message.

6

Conclusions and Future work

In this chapter, we review the main results of this doctoral thesis to take stock. A summary of the results is given in the section 6.1, followed by the future works, in section 6.2, necessary to develop the suggested system. Finally, we report the scientific contributions in section 6.3.

6.1 Summary of the main results

The main objective of this PhD project was to propose a power optimized solution for the synchronization of multi-node leadless pacemakers.
Among all radio-frequency communications, the galvanic Intra-Body Communication (IBC) seems to be tailored for leadless pacemaker applications. The advantages of IBC are:

1. ultra-low power requirement;
2. no additional antenna is required;
3. minimal risk of eavesdropping.

However, little work has been done about the IBC channel characterization for in-body communications since the IBC signal propagation is impacted by several factors, making difficult a pathloss analytical generalization. Thus, it was necessary to estimate the channel loss and point out the sensitivity requirements of the receiver.
To do so, we performed numerical simulations using a customized torso model, pointing out the voltage attenuation of IBC signals over a wide frequency domain [40 kHz - 20 MHz]. We focused on the main channels involved for LCP applications:

- the Intra-cardiac channel, defined as the communication channel between the RV capsule and the RA capsule;

- the Inter-ventricular channel, defined as the communication channel between the RV capsule and the epicardial surface of the LV;
- the Trans-thoracic channels, defined as the communication channel between the LCPs implanted in the heart and the body surface.

The simulation results showed that trans-thoracic channels experience the lowest attenuation, thanks to the possibility to place patch electrodes in an optimized positioning, leading to large inter-electrode distance and optimal orientation with respect to the implant device. The trans-thoracic channel is essential for programming the device and to retrieve data during patient follow-ups. However, these events are rare; thus, if properly managed, they will not weigh on the power budget of the LCP.
The attenuation of the Inter-ventricular channel ranges from 45 dB to 80 dB according to the channel length and the working frequency. The Inter-ventricular channel is intended to be used to share information among the RV capsule and an epicardial pacemaker fixed to the external wall of the LV.
The orientation of the capsules plays a key-role in the attenuation of IBC signals: the more aligned the lower the attenuation. However, the placement of the LCP must prioritize the optimization of the therapy, which can vary among the patient population. Thus, the attenuation of the intra-cardiac channel was estimated for both the worst- and the best-case condition. The intra-cardiac channel attenuation ranges from 72 dB to 55 dB, according to orientation and frequency. For capsules of fixed lengths, the orientation is the most effective variable, leading to an almost constant gap of 10 dB between the worst- and the best-case, over the whole spectrum under analysis. As foreseen by *Bereuter et al.* [20], the intra-cardiac channel experiences lower attenuation in the MHz-range thanks to the higher conductivity of the biological tissues.
This trend was confirmed through three in-vivo tests using capsules of the same size than those of the simulation. To do so, we prototyped a measurement system, which was verified and validated through in-vitro experiments. For the verification, we suggested a low-cost procedure using a NaCl-solution, whose concentration was changed to follow the conductivity of the heart over frequency. The results were validated through numerical simulations.
Thanks to the in-vivo trials, we were also able to see the relative change of the attenuation with respect to physiological activities such as respiration and heart beating. For what concerns respiration, the lowest attenuation was experienced during inflation; whereas for the heart cycle, we found that it is convenient to communicate during the ventricular repolarization (T-wave).
However, multi-node leadless pacemakers must be synchronized with the atrial activity of the heart (P-wave) to better reproduce a physiological heart functioning. Thus, the RA capsule must rather send a synchronization message to the other devices during the PR-interval.
We decided to focus our studies on the intra-cardiac channel that is the essential milestone toward multi-chamber leadless systems.

In the first part of chapter 4, we pointed out the transceiver constraints, considering the safety radiation guidelines provided by the International Commission on Non-Ionizing Radiation Protection (ICNIRP). The maximum allowed current density linearly increases with frequency. However, the power consumption of integrated circuits increases with frequency as well. Thus, we faced the low emission constraint designing a receiver with very high sensitivity property.
We identified a suitable ultra-low-power architecture for the receiver that could overcome the high sensitivity constraint: the Super-Regenerative Receiver (SRR). The SRR is particularly appealing since it can achieve extremely high gains with the lowest number of high-frequency blocks. A SRR was designed in 0.18 μm CMOS technology. The receiver was tailored for the synchronization of LCPs, achieving 18 μW of estimated active power. Simulation studies showed a robust design against the noise, achieving a Bit Error Rate lower than 0.01% of events with a sensitivity of -100 dBv.
Nevertheless, the active power consumption of the receiver prevents the LCP listening to the communication channel continuously. Thus, we acted on the optimization of the listening time of the receiver to reduce its impact on the device longevity. In chapter 5, we proposed an adaptive communication strategy allowing to reduce the receiver cycle time down to 2%. As a result, we have a receiver that can detect a synchronization pulse at each cardiac cycle, consuming only 340 nW of the LCP power budget. The additional power required by the receiver can be compensated over ten years increasing the battery charge capacity of 30 mAh, which is the 25% of the capacity of the LCP currently on the market.
This work led to the first power-optimized solution for communication-based LCP synchronization.

6.2 Future works

This work aggregates very different studies that were essential for the conception of an IBC-system for leadless pacemaker applications: channel characterization, ultra-low-power circuit, synchronization strategy; thus, there are aspects of the particular studies that could not be exhaustively covered by this work. Hereafter, we identify the future works that should be assessed to finalize and optimize our suggested solutions.

The characterization of the channels was tailored on a capsule prototype with length of 33 mm and diameter of 6.4 mm. More simulations should be performed to quantify the effect of the capsule length in terms of channel attenuation. Such a study can lead to an optimal LCP sizing as the compromise between low communication losses and mechanical constraints.
In this study, we used to inject IBC signals electrodes designed for therapy delivery to reduce the complexity of the LCP design. However, it is possible that sightly lower attenuation can be reached optimizing electrode size [127]. Moreover, with larger elec-

trodes come lower current densities, relaxing the constraint of the emitting voltage. This consideration is essential whenever IBC transceivers must work with limited carrier frequencies since the safety guidelines are more stringent at lower frequencies.
Furthermore, other in-vivo experiments should be performed to better characterize the environment noise and interferers, leading to a more accurate BER prediction.
Moreover, the same approach of channel characterization can be adopted for other implantable applications adapting the model to the particular sizing and positioning of the transducers.

In this work, an ultra-low-power receiver respecting all the specifications of our case of study was presented. As described in chapter 4, process-related variations must be counteracted, designing a calibration system for the receiver. Post-layout simulations must be performed to validate the results before the circuit integration. Then, the circuit should be tested using external signals to validate our results. These preliminary tests are intended to validate the performance of the super-regenerative receiver according to the proposed quenching signal. Once a correct operation of the suggested architecture is verified, a complete version of the transceiver must be designed. In particular, a stable signal generator is needed to quench the receiver, and a high-efficiency emitting circuitry must be designed.

The strategy suggested in this work can drastically reduce the power consumption for the synchronization of multi-node LCP systems. Multi-node LCP systems were chosen as the main application platform of our studies. However, the synchronization strategy can be adopted by any couple of devices including LCP implanted in the RV and another device that can detect the P-wave such as subcutaneous devices (i.e. Loop recorders, Subcutaneous-ICD). To validate the strategy, I suggest to synthesize the hardware and the controlling signals of the proposed technique in an FPGA. Then, in vivo experiments must be performed to evaluate how close the system is to a perfect atrioventricular synchronization.

6.3 Scientific contribution and publications

This work demonstrated the feasibility of a communication-based synchronization for Leadless Cardiac Pacemaker (LCP) through the Galvanic Intra-Body Communication (IBC). The system was analyzed from scratch, from the characterization of the channels to the drafting of the transceiver requirements. These requirements were used to design an ultra-low-power receiver in 0.18 μm CMOS technology to analyze the power budget required by this kind of solutions. The power budget of the receiver was amortized using an adaptable communication strategy leading to a power-efficient synchronization protocol.
The results of this work led to the submission of two patents to the french patent institute

(INPI) [128][129]:

- M.Maldari. *Système médical implantable pour mesurer un paramètre physiologique*, PA122168FR, 2019.
- M.Maldari. *Système pour réaliser une mesure d'impédance cardiographie*, PA126089FR, 2019.
- M.Maldari. *Procédé et système de communication entre plusieurs dispositifs médicaux implantables*, PA127465FR, 2020.

From what concerns the dissemination of this work, one international conference article [130], and one journal article [131] were published so far:

- M. Maldari, K. Amara, I. Rattalino, C. Jabbour, and P. Desgreys. *Human Body Communication channel characterization for leadless cardiac pacemakers*, 25th IEEE International Conference on Electronic Circuits (ICECS), 2018.
- M. Maldari, M. Albatat, J. Bergsland, Y. Haddab, C. Jabbour, and P. Desgreys. *Wide frequency characterization of intra-body communication for leadless pacemakers*, IEEE Transaction on Biomedical Engineering, 2020.

Another conference paper concurring to article extension selection is under submission. Furthermore, two works without acts were presented:

- M. Maldari. *Human Body Communication for leadless pacemaker applications*, International Micro-electronics Assembly and Packaging Society (iMAPS) Lyon, 2017.
- Mirko Maldari, Karima Amara, Chadi Jabbour, Patricia Desgreys. *Human Body Communication channel modeling for leadless cardiac pacemaker applications*, GDR SOC2 Paris, 2018.

Bibliography

[1] Plonsey Malmivuo, Jaakko Malmivuo, and Robert Plonsey. *Bioelectromagnetism: principles and applications of bioelectric and biomagnetic fields*. Oxford University Press, USA, 1995.

[2] J. L. Winter. Ecg educator blog, [online] available: https://ecg-educator.blogspot.com/2016/02/atrial-rhythms.html, 2016.

[3] Elaine Nicpon Marieb and Katja Hoehn. *Human anatomy & physiology*. Pearson education, 2007.

[4] Shaan Khurshid, Seung Hoan Choi, Lu-Chen Weng, Elizabeth Y Wang, Ludovic Trinquart, Emelia J Benjamin, Patrick T Ellinor, and Steven A Lubitz. Frequency of cardiac rhythm abnormalities in a half million adults. *Circulation: Arrhythmia and Electrophysiology*, 11(7):e006273, 2018.

[5] R. E. Kirkfeldt et al. Risk factors for lead complications in cardiac pacing: a population-based cohort study of 28,860 danish patients. *Heart Rhythm*, 8(10):1622–1628, 2011.

[6] R. E. Kirkfeldt et al. Complications after cardiac implantable electronic device implantations: an analysis of a complete, nationwide cohort in denmark. *European heart journal*, 35(18):1186–1194, 2013.

[7] M. S. Kiviniemi et al. Complications related to permanent pacemaker therapy. *Pacing and clinical electrophysiology*, 22(5):711–720, 1999.

[8] M. R. Sohail et al. Risk factor analysis of permanent pacemaker infection. *Clinical Infectious Diseases*, 45(2):166–173, 2007.

[9] E. O. Udo et al. Incidence and predictors of short-and long-term complications in pacemaker therapy: the followpace study. *Heart Rhythm*, 9(5):728–735, 2012.

[10] Wilhelm Fischer and Philippe Ritter. *Cardiac pacing in clinical practice*. Springer Science & Business Media, 2012.

[11] Marc A Miller, Petr Neuzil, Srinivas R Dukkipati, and Vivek Y Reddy. Leadless cardiac pacemakers: back to the future. *Journal of the American College of Cardiology*, 66(10):1179–1189, 2015.

[12] A. E. Epstein et al. Acc/aha/hrs 2008 guidelines for device-based therapy of cardiac rhythm abnormalities: a report of the american college of cardiology/american heart association task force on practice guidelines (writing committee to revise the acc/aha/naspe 2002 guideline update for implantation of cardiac pacemakers and antiarrhythmia devices) developed in collaboration with the american association for thoracic surgery and society of thoracic surgeons. *Journal of the American College of Cardiology*, 51(21):e1–e62, 2008.

[13] M Albatat, J Bergsland, H Arevalo, HH Odland, P Bose, PS Halvorsen, and I Balasingham. Technological and clinical challenges in lead placement for cardiac rhythm management devices. *Annals of Biomedical Engineering*, pages 1–21, 2019.

[14] M. S. Wegmüller. *Intra-body communication for biomedical sensor networks*. PhD thesis, ETH Zurich, 2007.

[15] D. Das et al. Enabling covert body area network using electro-quasistatic human body communication. *Scientific reports*, 9(1):4160, 2019.

[16] Thoams Guthrie Zimmerman. Personal area networks: near-field intrabody communication. *IBM systems Journal*, 35(3.4):609–617, 1996.

[17] M. A. Callejón et al. Galvanic coupling transmission in intrabody communication: A finite element approach. *IEEE Transactions on Biomedical Engineering*, 61(3):775–783, 2014.

[18] Y. Song et al. The simulation method of the galvanic coupling intrabody communication with different signal transmission paths. *IEEE Transactions on Instrumentation and Measurement*, 60(4):1257–1266, 2011.

[19] S. Maity et al. Bio-physical modeling, characterization, and optimization of electro-quasistatic human body communication. *IEEE Transactions on Biomedical Engineering*, 66(6):1791–1802, 2018.

[20] L. Bereuter et al. Fundamental characterization of conductive intracardiac communication for leadless multisite pacemaker systems. *IEEE transactions on biomedical circuits and systems*, 13(1):237–247, 2019.

[21] M.A. Callejón et al. Measurement issues in galvanic intrabody communication: Influence of experimental setup. *IEEE Transactions on Biomedical Engineering*, 62(11):2724–2732, 2015.

[22] Lukas Bereuter, Mirco Gysin, Thomas Kueffer, Martin Kucera, Thomas Niederhauser, Jürg Fuhrer, Paul Heinisch, Adrian Zurbuchen, Dominik Obrist, Hildegard Tanner, et al. Leadless dual-chamber pacing: a novel communication method for wireless pacemaker synchronization. *JACC: Basic to Translational Science*, 3(6):813–823, 2018.

[23] Lukas Bereuter, Thomas Niederhauser, Martin Kucera, Dominic Loosli, Immanuel Steib, Marcel Schildknecht, Adrian Zurbuchen, Fabian Noti, Hildegard Tanner, Tobias Reichlin, et al. Leadless cardiac resynchronization therapy: An in vivo proof-of-concept study of wireless pacemaker synchronization. *Heart rhythm*, 16(6):936–942, 2019.

[24] NTNU. Wireless in-body environment communication (wibec), 2017. [online] available: https://www.ntnu.edu/wibec, 2017.

[25] Frank Henry Netter, Sharon Colacino, et al. *Atlas of human anatomy*. Ciba-Geigy Corporation, 1989.

[26] Glauco Ambrosi, Giuseppe Anastasi, Dario Cantino, S Capitani, P Castano, FR Donato, AT Franzi, E Gaudio, R Geremia, M Gulisano, et al. Anatomia dell'uomo. *Seconda Edizione edi-ermes*, 2001.

[27] Comunità europee. Istituto statistico. *Health Statistics: Atlas on Mortality in the European Union*. Office for official publications of the European Communities, 2009.

[28] Baris Akdemir, Hirad Yarmohammadi, M Chadi Alraies, and Wayne O Adkisson. Premature ventricular contractions: Reassure or refer? *Cleveland Clinic journal of medicine*, 83(7):525, 2016.

[29] Julia Vogler, Günter Breithardt, and Lars Eckardt. Bradyarrhythmias and conduction blocks. *Revista Española de Cardiología (English Edition)*, 65(7):656–667, 2012.

[30] Carlos A Morillo, Amitava Banerjee, Pablo Perel, David Wood, and Xavier Jouven. Atrial fibrillation: the current epidemic. *Journal of geriatric cardiology: JGC*, 14(3):195, 2017.

[31] Mark A Crandall, David J Bradley, Douglas L Packer, and Samuel J Asirvatham. Contemporary management of atrial fibrillation: update on anticoagulation and invasive management strategies. In *Mayo Clinic Proceedings*, volume 84, pages 643–662. Elsevier, 2009.

[32] Ashish Shukla and Anne B Curtis. Avoiding permanent atrial fibrillation: treatment approaches to prevent disease progression. *Vascular health and risk management*, 10:1, 2014.

[33] Justin Z Lee, Jayna Ling, Nancy N Diehl, David O Hodge, Deepak Padmanabhan, Ammar M Killu, Malini Madhavan, Peter A Noseworthy, Suraj Kapa, Christopher J McLeod, et al. Mortality and cerebrovascular events after heart rhythm disorder management procedures. *Circulation*, 137(1):24–33, 2018.

[34] J William Spickler, Ned S Rasor, Paul Kezdi, SN Misra, KE Robins, and Charles LeBoeuf. Totally self-contained intracardiac pacemaker. *Journal of electrocardiology*, 3(3-4):325–331, 1970.

[35] Kenneth A Ellenbogen, Bruce L Wilkoff, G Neal Kay, Chu Pak Lau, and Angelo Auricchio. *Clinical Cardiac Pacing, Defibrillation and Resynchronization Therapy E-Book*. Elsevier Health Sciences, 2016.

[36] Neal Bhatia and Mikhael El-Chami. Leadless pacemakers: a contemporary review. *Journal of geriatric cardiology: JGC*, 15(4):249, 2018.

[37] Anne Kroman, Basil Saour, and Jordan M Prutkin. Leadless pacemakers: Recent and future developments. *Current treatment options in cardiovascular medicine*, 21(10):54, 2019.

[38] Larry Chinitz, Philippe Ritter, Surinder Kaur Khelae, Saverio Iacopino, Christophe Garweg, Maria Grazia-Bongiorni, Petr Neuzil, Jens Brock Johansen, Lluis Mont, Efrain Gonzalez, et al. Accelerometer-based atrioventricular synchronous pacing with a ventricular leadless pacemaker: Results from the micra atrioventricular feasibility studies. *Heart rhythm*, 15(9):1363–1371, 2018.

[39] Kalman Ausubel and Seymour Furman. The pacemaker syndrome. *Annals of internal medicine*, 103(3):420–429, 1985.

[40] Maria Amparo Callejon, David Naranjo-Hernandez, Javier Reina-Tosina, and Laura M Roa. A comprehensive study into intrabody communication measurements. *IEEE Transactions on Instrumentation and Measurement*, 62(9):2446–2455, 2013.

[41] Yong Song, Qun Hao, Kai Zhang, Ming Wang, Yifang Chu, and Bangzhi Kang. The simulation method of the galvanic coupling intrabody communication with different signal transmission paths. *IEEE Transactions on Instrumentation and Measurement*, 60(4):1257–1266, 2010.

[42] Assefa K Teshome, Behailu Kibret, and Daniel TH Lai. Galvanically coupled intrabody communications for medical implants: a unified analytic model. *IEEE Transactions on Antennas and Propagation*, 64(7):2989–3002, 2016.

[43] World Medical Association et al. World medical association declaration of helsinki. ethical principles for medical research involving human subjects. *Bulletin of the World Health Organization*, 79(4):373, 2001.

[44] Tarek Said and Vasundara V Varadan. Variation of cole-cole model parameters with the complex permittivity of biological tissues. In *2009 IEEE MTT-S International Microwave Symposium Digest*, pages 1445–1448. IEEE, 2009.

[45] C. Gabriel et al. The dielectric properties of biological tissues: I. literature survey. *Physics in medicine & biology*, 41(11):2231, 1996.

[46] C.Petrucci D.Andreuccetti, R.Fossi. An internet resource for the calculation of the dielectric properties of body tissues in the frequency range 10 hz - 100 ghz. ifac-cnr, florence (italy), 1997. based on data published by c.gabriel et al. in 1996. [online]. available: http://niremf.ifac.cnr.it/tissprop/, 1997.

[47] Darrell W Pepper and Juan C Heinrich. *The finite element method: basic concepts and applications with MATLAB, MAPLE, and COMSOL*. CRC Press, 2017.

[48] Robert Plonsey and Dennis B Heppner. Considerations of quasi-stationarity in electrophysiological systems. *The Bulletin of mathematical biophysics*, 29(4):657–664, 1967.

[49] Kyung Sup Kwak, Sana Ullah, and Niamat Ullah. An overview of ieee 802.15. 6 standard. In *2010 3rd International Symposium on Applied Sciences in Biomedical and Communication Technologies (ISABEL 2010)*, pages 1–6. IEEE, 2010.

[50] Y. Song et al. A finite-element simulation of galvanic coupling intra-body communication based on the whole human body. *Sensors*, 12(10):13567–13582, 2012.

[51] J. Wang et al. Analysis of on-body transmission mechanism and characteristic based on an electromagnetic field approach. *IEEE Transactions on Microwave Theory and Techniques*, 57(10):2464–2470, 2009.

[52] Synopsys. *Simpleware Scan IP Software, with the Simpleware FE, NURBS, CAD, FLOW, SOLID, and LAPLACE modules Reference Guide*, 2017.

[53] Alicia M Maceira, Sanjay K Prasad, Mohammed Khan, and Dudley J Pennell. Reference right ventricular systolic and diastolic function normalized to age, gender and body surface area from steady-state free precession cardiovascular magnetic resonance. *European heart journal*, 27(23):2879–2888, 2006.

[54] Yinshi Wang, Jack M Gutman, David Heilbron, Dennis Wahr, and Nelson B Schiller. Atrial volume in a normal adult population by two-dimensional echocardiography. *Chest*, 86(4):595–601, 1984.

[55] SW Rabkin. Epicardial fat: properties, function and relationship to obesity. *Obesity reviews*, 8(3):253–261, 2007.

[56] K. S. Cole and R. H. Cole. Dispersion and absorption in dielectrics i. alternating current characteristics. *The Journal of chemical physics*, 9(4):341–351, 1941.

[57] J. Larsson. Electromagnetics from a quasistatic perspective. *American Journal of Physics*, 75(3):230–239, 2007.

[58] Y. Gan et al. Dry electrode materials for electrocardiographic monitoring. In *2018 25th IEEE International Conference on Electronics, Circuits and Systems (ICECS)*, pages 645–646. IEEE, 2018.

[59] Peyman Mirtaheri, Sverre Grimnes, and G Martinsen. Electrode polarization impedance in weak nacl aqueous solutions. *IEEE Transactions on biomedical Engineering*, 52(12):2093–2099, 2005.

[60] M. Wegmueller et al. Measurement system for the characterization of the human body as a communication channel at low frequency. In *IEEE EMBC 2006*, pages 3502–3505. IEEE, 2006.

[61] VH Rumsey. Reaction concept in electromagnetic theory. *Physical Review*, 94(6):1483, 1954.

[62] Angelo Auricchio, Helmut Klein, Bruce Tockman, Stefan Sack, Christoph Stellbrink, Jörg Neuzner, Andrew Kramer, Jiang Ding, Thierry Pochet, Albert Maarse, et al. Transvenous biventricular pacing for heart failure: can the obstacles be overcome? *The American journal of cardiology*, 83(5):136–142, 1999.

[63] Christian Butter, Angelo Auricchio, Christoph Stellbrink, Michael Schlegl, Eckart Fleck, Walter Hörsch, Etienne Huvelle, Jiang Ding, Andrew Kramer, Pacing Therapies in Congestive Heart Failure II Study Group, et al. Should stimulation site be tailored in the individual heart failure patient? *The American journal of cardiology*, 86(9):K144–K151, 2000.

[64] Christian Butter, Angelo Auricchio, Christoph Stellbrink, Eckart Fleck, Jiang Ding, Yinghong Yu, Etienne Huvelle, and Julio Spinelli. Effect of resynchronization therapy stimulation site on the systolic function of heart failure patients. *Circulation*, 104(25):3026–3029, 2001.

[65] Angelo Auricchio, Christoph Stellbrink, Stefan Sack, Michael Block, J ürgen Vogt, Patricia Bakker, Christof Huth, Friedrich Schöndube, Ulrich Wolfhard, Dirk Böcker, et al. Long-term clinical effect of hemodynamically optimized cardiac resynchronization therapy in patients with heart failure and ventricular conduction delay. *Journal of the American College of Cardiology*, 39(12):2026–2033, 2002.

[66] S Grassini. Electrochemical impedance spectroscopy (eis) for the in-situ analysis of metallic heritage artefacts. In *Corrosion and Conservation of Cultural Heritage Metallic Artefacts*, pages 347–367. Elsevier, 2013.

[67] JB Bates and YT Chu. Electrode-electrolyte interface impedance: experiments and model. *Annals of biomedical engineering*, 20(3):349–362, 1992.

[68] Ramón Pallás-Areny and John G Webster. Common mode rejection ratio in differential amplifiers. *IEEE Transactions on Instrumentation and Measurement*, 40(4):669–676, 1991.

[69] D. H. Gadani et al. Effect of salinity on the dielectric properties of water. *NISCAIR-CSIR, India*, 2012.

[70] P. Bose et al. Rf channel modeling for implant-to-implant communication and implant to subcutaneous implant communication for future leadless cardiac pacemakers. *IEEE Transactions on Biomedical Engineering*, 65(12):2798–2807, 2018.

[71] Brian D McCauley and Antony F Chu. Leadless cardiac pacemakers: the next evolution in pacemaker technology. *Rhode Island Medical Journal*, 100(11):31–34, 2017.

[72] Alexander Ng and Justiaan Swanevelder. Resolution in ultrasound imaging. *Continuing Education in Anaesthesia Critical Care & Pain*, 11(5):186–192, 2011.

[73] Parisa Gifani, Hamid Behnam, and Zahra Alizadeh Sani. A new method for pseudo-increasing frame rates of echocardiography images using manifold learning. *Journal of medical signals and sensors*, 1(2):107, 2011.

[74] International Commission on Non-Ionizing Radiation Protection et al. Icnirp statement on the "guidelines for limiting exposure to time-varying electric, magnetic, and electromagnetic fields (up to 300 ghz)". *Health physics*, 97(3):257–258, 2009.

[75] Jianqing Wang and Qiong Wang. *Body area communications: channel modeling, communication systems, and EMC*. John Wiley & Sons, 2012.

[76] magnetic Guidelines for limiting exposure to time-varying electric and electromagnetic fields (up to 300 GHz). International commission on non-ionizing radiation protection. *Health Phys*, 74:494–522, 1998.

[77] Maarten Lont, Dusan Milosevic, and Arthur van Roermund. *Wake-up receiver based ultra-low-power WBAN*. Springer, 2014.

[78] Long Yan, Joonsung Bae, Seulki Lee, Taehwan Roh, Kiseok Song, and Hoi-Jun Yoo. A 3.9 mw 25-electrode reconfigured sensor for wearable cardiac monitoring system. *IEEE Journal of Solid-State Circuits*, 46(1):353–364, 2010.

[79] Hyunwoo Cho, Joonsung Bae, and Hoi-Jun Yoo. A 37.5 μw body channel communication wake-up receiver with injection-locking ring oscillator for wireless body area network. *IEEE Transactions on Circuits and Systems I: Regular Papers*, 60(5):1200–1208, 2013.

[80] Hyunwoo Cho, Hyunki Kim, Minseo Kim, Jaeeun Jang, Yongsu Lee, Kyuho Jason Lee, Joonsung Bae, and Hoi-Jun Yoo. A 79 pj/b 80 mb/s full-duplex transceiver

and a 42.5μw 100 kb/s super-regenerative transceiver for body channel communication. *IEEE journal of solid-state circuits*, 51(1):310–317, 2015.

[81] Joonsung Bae and Hoi-Jun Yoo. A 45μw injection-locked fsk wake-up receiver with frequency-to-envelope conversion for crystal-less wireless body area network. *IEEE Journal of Solid-State Circuits*, 50(6):1351–1360, 2015.

[82] Majid Haghjoo. Pacing system malfunction: evaluation and troubleshooting. *Modern Pacemakers–Present and Future. Rijeka: InTech*, pages 367–80, 2011.

[83] Payam Safavi-Naeini and Mohammad Saeed. Pacemaker troubleshooting: common clinical scenarios. *Texas Heart Institute Journal*, 43(5):415–418, 2016.

[84] VAN CMC CAMPEN, CAREL C DE COCK, Jeroen Huijgens, and Cees A Visser. Clinical relevance of loss of atrial sensing in patients with single lead vdd pacemakers. *Pacing and Clinical Electrophysiology*, 24(5):806–809, 2001.

[85] Upamanyu Madhow. *Fundamentals of digital communication*. Cambridge University Press, 2008.

[86] Claudio Canuto and Anita Tabacco. *Mathematical analysis II*, volume 85. Springer, 2015.

[87] John Oetting. A comparison of modulation techniques for digital radio. *IEEE Transactions on communications*, 27(12):1752–1762, 1979.

[88] Xiongchuan Huang, Simonetta Rampu, Xiaoyan Wang, Guido Dolmans, and Harmke De Groot. A 2.4 ghz/915mhz 51μw wake-up receiver with offset and noise suppression. In *2010 IEEE International Solid-State Circuits Conference-(ISSCC)*, pages 222–223. IEEE, 2010.

[89] A Elgani, M Magno, F Renzini, Luca Perilli, E Franchi Scarselli, Antonio Gnudi, Roberto Canegallo, G Ricotti, and Luca Benini. Nanowatt wake-up radios: Discrete-components and integrated architectures. In *2018 25th IEEE International Conference on Electronics, Circuits and Systems (ICECS)*, pages 793–796. IEEE, 2018.

[90] Michele Magno and Luca Benini. An ultra low power high sensitivity wake-up radio receiver with addressing capability. In *2014 IEEE 10th International Conference on Wireless and Mobile Computing, Networking and Communications (WiMob)*, pages 92–99. IEEE, 2014.

[91] Seunghyun Oh, Nathan E Roberts, and David D Wentzloff. A 116nw multi-band wake-up receiver with 31-bit correlator and interference rejection. In *Proceedings of the IEEE 2013 Custom Integrated Circuits Conference*, pages 1–4. IEEE, 2013.

[92] Nathan E Roberts and David D Wentzloff. A 98nw wake-up radio for wireless body area networks. In *2012 IEEE Radio Frequency Integrated Circuits Symposium*, pages 373–376. IEEE, 2012.

[93] Shovan Maity, David Yang, Baibhab Chatterjee, and Shreyas Sen. A sub-nw wake-up receiver for human body communication. In *2018 IEEE Biomedical Circuits and Systems Conference (BioCAS)*, pages 1–4. IEEE, 2018.

[94] Fei Yuan. *CMOS circuits for passive wireless microsystems*. Springer Science & Business Media, 2010.

[95] Brian Otis and Jan Rabaey. *Ultra-low power wireless technologies for sensor networks*. Springer Science & Business Media, 2007.

[96] Hiroshi Fuketa, Shinichi O'uchi, and Takashi Matsukawa. A 0.3-v 1-*mu*w super-regenerative ultrasound wake-up receiver with power scalability. *IEEE Transactions on Circuits and Systems II: Express Briefs*, 64(9):1027–1031, 2016.

[97] Samar Alsaegh, Sherif AS Mohamed, and Yiannos Manoli. Design of 1mwcmos ook super-regenerative receiver for 402–405mhz medical applications. In *2014 IEEE International Symposium on Circuits and Systems (ISCAS)*, pages 1400–1403. IEEE, 2014.

[98] Jose L Bohorquez, Anantha P Chandrakasan, and Joel L Dawson. A 350 μw cmos msk transmitter and 400μw ook super-regenerative receiver for medical implant communications. *IEEE Journal of Solid-State Circuits*, 44(4):1248–1259, 2009.

[99] Naci Pekcokguler, Gunhan Dundar, and Catherine Dehollain. Analysis, modeling and design of a cmos super-regenerative receiver for implanted medical devices under square and sinusoidal quench signals. *Integration*, 67:1–7, 2019.

[100] Vahid Dabbagh Rezaei, Stephen J Shellhammer, Mohamed Elkholy, and Kamran Entesari. A fully integrated 320 pj/b ook super-regenerative receiver with- 87 dbm sensitivity and self-calibration. In *2016 IEEE Radio Frequency Integrated Circuits Symposium (RFIC)*, pages 222–225. IEEE, 2016.

[101] Jia-Yi Chen, Michael P Flynn, and John P Hayes. A fully integrated auto-calibrated super-regenerative receiver in $0.13-\mu$m cmos. *IEEE Journal of Solid-state circuits*, 42(9):1976–1985, 2007.

[102] Edwin H Armstrong. Some recent developments of regenerative circuits. *Proceedings of the Institute of Radio Engineers*, 10(4):244–260, 1922.

[103] Thomas H Lee. *The design of CMOS radio-frequency integrated circuits*. Cambridge university press, 2003.

[104] Andrei Grebennikov. *RF and microwave transistor oscillator design*. John Wiley & Sons, 2007.

[105] F Xavier Moncunill-Geniz, Pere Pala-Schonwalder, and Orestes Mas-Casals. A generic approach to the theory of superregenerative reception. *IEEE Transactions on Circuits and Systems I: regular papers*, 52(1):54–70, 2005.

[106] Prakash E Thoppay, Catherine Dehollain, and Michel J Declercq. Noise analysis in super-regenerative receiver systems. In *2008 Ph. D. Research in Microelectronics and Electronics*, pages 189–192. IEEE, 2008.

[107] Guillermo Gonzalez. *Foundations of oscillator circuit design*. Artech House Norwood, 2007.

[108] Miguel A Martins, Pui-In Mak, and Rui P Martins. A 0.02-to-6ghz sdr balun-lna using a triple-stage inverter-based amplifier. In *2012 IEEE International Symposium on Circuits and Systems*, pages 472–475. IEEE, 2012.

[109] Phillip E Allen and Douglas R Holberg. *CMOS analog circuit design*. Elsevier, 2011.

[110] Gyu-Seob Jeong, Hankyu Chi, Kyungock Kim, and Deog-Kyoon Jeong. A 20-gb/s 1.27 pj/b low-power optical receiver front-end in 65nm cmos. In *2014 IEEE International Symposium on Circuits and Systems (ISCAS)*, pages 1492–1495. IEEE, 2014.

[111] Sherif M Sharroush. Design of the cmos inverter-based amplifier: A quantitative approach. *International Journal of Circuit Theory and Applications*, 47(7):1006–1036, 2019.

[112] Skawrat Wangtaphan and Varakorn Kasemsuwan. A high performance thermal noise-canceling transimpedance-based differential amplifier. In *TENCON 2009-2009 IEEE Region 10 Conference*, pages 1–4. IEEE, 2009.

[113] Ahmad Yarahmadi and Abumoslem Jannesari. Two-path inverter-based low noise amplifier for 10–12 ghz applications. *Microelectronics journal*, 50:76–82, 2016.

[114] Ivy Lo, Olga Boric-Lubecke, and Victor Lubecke. 0.25 μm cmos dual feedback wide-band uhf low noise amplifier. In *2007 IEEE/MTT-S International Microwave Symposium*, pages 1059–1062. IEEE, 2007.

[115] Stanley BT Wang, Ali M Niknejad, and Robert W Brodersen. A sub-mw 960-mhz ultra-wideband cmos lna. In *2005 IEEE Radio Frequency integrated Circuits (RFIC) Symposium-Digest of Papers*, pages 35–38. IEEE, 2005.

[116] Jun-Young Park, Ji-Young Lee, Cheong-Ki Yeo, and Tae-Yeoul Yun. Analysis and optimization of a resistive-feedback inverter lna. *Microwave and Optical Technology Letters*, 60(5):1143–1151, 2018.

[117] Behzad Razavi. *Design of analog CMOS integrated circuits*. McGraw-Hill Education, 2017.

[118] Mel Bazes. Two novel fully complementary self-biased cmos differential amplifiers. *IEEE Journal of Solid-State Circuits*, 26(2):165–168, 1991.

[119] James S Hutchison, Roxanne E Ward, Jacques Lacroix, Paul C Hébert, Marcia A Barnes, Desmond J Bohn, Peter B Dirks, Steve Doucette, Dean Fergusson, Ronald Gottesman, et al. Hypothermia therapy after traumatic brain injury in children. *New England Journal of Medicine*, 358(23):2447–2456, 2008.

[120] Donald B Estreich and Robert W Dutton. Modeling latch-up in cmos integrated circuits. *IEEE Transactions on computer-aided design of integrated circuits and systems*, 1(4):157–162, 1982.

[121] Simon M Sze and Kwok K Ng. *Physics of semiconductor devices*. John wiley & sons, 2006.

[122] L Géroux, M Limousin, and S Cazeau. Clinical performances of a new mode switch function based on a statistical analysis of the atrial rhythm. *Herzschrittmachertherapie und Elektrophysiologie*, 10(1):S15–S21, 1999.

[123] H. Elmqvist. Stimulateur cardiaques intelligents et consommation d'energie. *CARDIOSTIM80*, pages 206–213, 1980.

[124] Anantha P Chandrakasan, Samuel Sheng, and Robert W Brodersen. Low-power cmos digital design. *IEICE Transactions on Electronics*, 75(4):371–382, 1992.

[125] American Heart Association et al. All about heart rate (pulse). *Retrieved from*, 2012.

[126] Anthony C Pearson, Denise L Janosik, Robert M Redd, Thomas A Buckingham, Arthur J Labovitz, and Denise Mrosek. Hemodynamic benefit of atrioventricular synchrony: prediction from baseline doppler-echocardiographic variables. *Journal of the American College of Cardiology*, 13(7):1613–1621, 1989.

[127] S. Maity et al. Characterization of human body forward path loss and variability effects in voltage-mode hbc. *IEEE Microwave and Wireless Components Letters*, 28(3):266–268, 2018.

[128] Mirko Maldari. Système pour réaliser une mesure d'impédance cardiographie, PA126089FR., 2019.

[129] Mirko Maldari. Système médical implantable pour mesurer un paramètre physiologique, PA122168FR., 2019.

[130] Mirko Maldari, Karima Amara, Ismael Rattalino, Chadi Jabbour, and Patricia Desgreys. Human body communication channel characterization for leadless cardiac pacemakers. In *2018 25th IEEE International Conference on Electronics, Circuits and Systems (ICECS)*, pages 185–188. IEEE, 2018.

[131] M. Maldari, M. Albatat, Bergsland, J., Y. Haddab, C. Jabbour, and P. Desgreys. Wide frequency characterization of intra-body communication for leadless pacemakers. *IEEE Transactions on Biomedical Engineering*, 2020.

[132] Roger Grimshaw. *Nonlinear ordinary differential equations*. Routledge, 2017.

[133] Martin Braun and Martin Golubitsky. *Differential equations and their applications*, volume 4. Springer, 1983.

Appendices

A

Analytical study of the SRR

A.1 Time domain analysis

For the sake of simplicity, let us consider the block diagram depicted in Figure 4.4 with an LNTA of unitary gain. Without loss of generality, the band pass filter can be modeled as a second order passive filter whose transfer function in Laplace domain is represented by (A.1)

$$G(s) = K_0 \frac{2\zeta_0\omega_0 s}{s^2 + 2\zeta_0\omega_0 s + \omega_0^2}, \tag{A.1}$$

where K_0 is the minimum attenuation of the filter, ζ_0 is the quiescent damping factor, and ω_0 is the resonance frequency [105]. Recalling that the transfer function is defined as the ratio between the output and the input of a system, it is straightforward to retrieve the following differential equation that characterizes the system,

$$\ddot{v}_o(t) + 2\zeta_0\omega_0\dot{v}_o(t) + \omega^2 v_o(t) = K_0 2\zeta_0\omega_0\dot{v}_f(t). \tag{A.2}$$

Knowing that the feedback must be positive to satisfy the second Barkhausen criterion to let the system oscillate, the feedback signal can be rewritten as $v_f(t) = v_{in}(t) + A(t)v_o(t)$ and the general form of (A.2) can be described as

$$\ddot{v}_o(t) + 2\zeta(t)\omega_0\dot{v}_o(t) + \omega^2 v_o(t) = K_0 2\zeta_0\omega_0\dot{v}_{in}(t), \tag{A.3}$$

where $\zeta(t)$ is the instantaneous damping factor that includes the time variable gain of the feedback amplifier,

$$\zeta(t) = \zeta_0(1 - K_0 A(t)). \tag{A.4}$$

The time evolution of the output signal of a SRR system is plotted in Figure A.1. The instantaneous damping factor $\zeta(t)$ depends on the feedback amplifier gain that is controlled by the quench signal. When $\zeta(t) = 0$ the amplifier counterbalances the dispersion of the band pass filter. The negative area under the curve determines the super-regenerative period, where the amplifier is able to drive the system into instability.

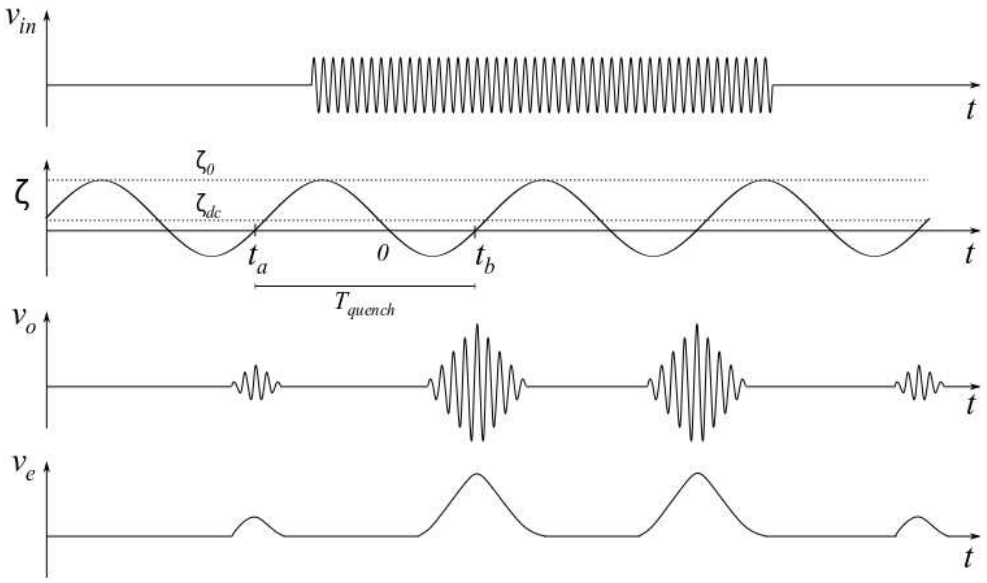

Figure A.1: Evolution of the input signal through super-regenerative receivers according to the damping function ζ

At $t = 0$, $\zeta(t) = 0$ meaning that the system satisfies the condition to oscillate. At this point, the injected signal significantly changes the initial condition of the oscillating system; thus, the contribution of the input signal reaches its maximum at $t = 0$. Then, the oscillation amplitude increases reaching its maximum value at $t = t_b$, where $\zeta(t)$ becomes positive and the oscillation is damped. The quenching period T_{quench} must ensure that the oscillation expires to avoid that previous cycles interferes with the real-time demodulation. The equation characterizing the system, (A.3), is a second order linear differential equation and as such its general solution is the sum of the solutions of the homogeneous and the particular equations,

$$v_o(t) = v_{o,h}(t) + v_{o,p}(t). \tag{A.5}$$

Here, we briefly comment the intuitive meaning of the two solutions and sketch how Moncunill found them [105]. The solution of the homogeneous equation $v_{o,h}(t)$ can be though as the free response of the system that does not depend on the input signal $v_{in}(t)$. The solution of the particular equation $v_{o,p}(t)$ represents the response to the input signal excitation. To solve the homogeneous equation (A.6)

$$\ddot{v}_o(t) + 2\zeta(t)\omega_0\dot{v}_o(t) + \omega^2 v_o(t) = 0, \tag{A.6}$$

we can apply an appropriate change of variable [132]

$$v_{o,h}(t) = u(t)e^{-\omega_0 \int_{t_a}^{t} \zeta(\lambda)d\lambda}. \tag{A.7}$$

In this way, the first derivative of the homogeneous solution can be written as

$$\dot{v}_{o,h}(t) = (\dot{u}(t) - \omega_0\zeta(t)u(t))e^{-\omega_0\int_{t_a}^{t}\zeta(\lambda)d\lambda}. \tag{A.8}$$

Iterating the derivative we can find also the second order term of (A.3)

$$\ddot{v}_{o,h}(t) = (\ddot{u}(t) - 2\omega_0\zeta(t)\dot{u}(t) + [(\omega_0\zeta(t))^2 - \omega_0\dot{\zeta}(t)]u)e^{-\omega_0\int_{t_a}^{t}\zeta(\lambda)d\lambda}. \tag{A.9}$$

Substituting the variable and its derivatives in (A.3) we find a easiest representation known as Hill equation

$$\ddot{u}(t) + \omega_0^2\left(1 - \zeta^2(t) - \frac{\dot{\zeta}(t)}{\omega_0}\right)u(t) = 0. \tag{A.10}$$

It is possible to decrease the complexity of the solution on top of two reasonable assumptions:

- The system is underdamped, hence it is able to give an oscillatory response at any time during the period T_{quench}.
- The damping factor changes slowly, that is usually respected in super-regenerative systems to improve sensitivity [100].

Mathematically speaking, we are assuming that

$$\zeta^2(t) << 1 \tag{A.11}$$

$$\dot{\zeta}(t) << \omega_0 \tag{A.12}$$

It is worth pointing out that the assumption A.11 implies that the modulus of the instantaneous quality factor must be kept high enough over the whole T_{quench}. Thanks to those assumptions, we can reformulate (A.10) as

$$\ddot{u}(t) + \omega_0^2 u(t) = 0, \tag{A.13}$$

whose solution is

$$u(t) = 2\Re\{V_1 e^{j\omega_0 t}\} = V_1 e^{j\omega_0 t} + V_1^* e^{-j\omega_0 t}. \tag{A.14}$$

Substituting A.14 in A.7 we can find the general solution of the homogeneous differential equation

$$v_{o,h}(t) = e^{-\omega_0\int_{t_a}^{t}\zeta(\lambda)d\lambda}2\Re\{V_1 e^{j\omega_0 t}\}. \tag{A.15}$$

The solution of the particular equation can be found using the method of variation of parameters. The basic principle of this method is to use convenient solutions of the homogeneous equation to find a solution of the particular equation [133]. In particular, this method uses the principle that linear combinations of solutions of a differential equation are themselves solution of differential equations. In this way, we can write the particular solution as

$$v_{o,p}(t) = 2\Re[V_2(t)b(t)] = V_2(t)b(t) + V_2^*(t)b^*(t), \tag{A.16}$$

where b(t) is the base of the solution of the homogeneous equation

$$b(t) = e^{-\omega_0 \int_{t_a}^{t} \zeta(\lambda) d\lambda} e^{j\omega_0 t}. \tag{A.17}$$

Assuming that $V_2(t)$ respects the following conditions

$$\dot{V}_2(t)b(t) + \dot{V}_2^*(t)b^*(t) = 0 \tag{A.18}$$

$$\dot{V}_2(t)\dot{b}(t) + \dot{V}_2^*(t)\dot{b}^*(t) = 2K_0\zeta_0\omega_0\dot{v}(t) \tag{A.19}$$

the solution of the particular equation is provided by integrating

$$\dot{V}_2(t) = -jK_0\zeta_0\frac{\dot{v}(t)}{b(t)} \tag{A.20}$$

and it is equal to

$$V_2(t) = -jK_0\zeta_0\int_{t_a}^{t}\frac{\dot{v}(\tau)}{b(\tau)}d\tau = -jK_0\zeta_0\int_{t_a}^{t}\dot{v}(\tau)e^{\omega_0\int_{t_a}^{\tau}\zeta(\lambda)d\lambda}e^{-j\omega_0\tau}d\tau. \tag{A.21}$$

Now we can substitute the equation of $V_2(t)$ and $b(t)$ in A.16 and get the solution of the particular equation,

$$v_{o,p}(t) = e^{-\omega_0\int_{t_a}^{t}\zeta(\lambda)d\lambda}2\Re\left\{-jK_0\zeta_0\int_{t_a}^{t}\dot{v}(\tau)e^{\omega_0\int_{t_a}^{\tau}\zeta(\lambda)d\lambda}e^{-j\omega_0(\tau-t)}d\tau\right\}. \tag{A.22}$$

The particular solution $v_{o,p}(t)$ can be used to interpret the system reaction to the input signal $v(t)$. It is shown that the output response depends on the derivative of the input signal amplitude rather than the signal amplitude itself. The first exponential term defines the behavior of the quenched oscillator of the SRR. Depending on the sign of the instantaneous damping factor $\zeta(\lambda)$, the system output may be either attenuated (for $\zeta > 0$) or amplified (for $\zeta < 0$). For the sake of clarity, Let us consider the distribution of ζ depicted in Figure A.1. In the time range $[0; t_b] \subseteq T_{quench}$, ζ has negative values, and becomes positive right after t_b. Thus, we can define the *Super-Regenerative gain* K_s and the *Normalized envelope of the SRO* $p(t)$ as

$$K_s = e^{-\omega_0\int_0^{t_b}\zeta(\lambda)d\lambda} \tag{A.23}$$

$$p(t) = e^{-\omega_0\int_{t_b}^{t}\zeta(\lambda)d\lambda}. \tag{A.24}$$

For low input signals $v(t)$, we can consider that the first exponential in (A.16) dominates over the second term of the equation. Hence, the *Sensitivity curve* is defined as

$$s(t) = e^{\omega_0\int_0^t\zeta(\lambda)d\lambda} \tag{A.25}$$

Using (A.25), (A.23), and (A.24), it is possible to rewrite the homogenous and the particular solution of the differential equation as

$$v_{o,h}(t) = |V_1|p(t)cos(\omega_0 t + \angle V_1) \tag{A.26}$$

$$v_{o,p}(t) = 2\zeta_0 K_0 K_s p(t)\int \dot{v}(\tau)s(\tau)sin[\omega_0(t-\tau)]d\tau. \tag{A.27}$$

Focusing the attention on a single quenching period T_{quench}, we can note that the maximum value of both $s(t)$ and $p(t)$ is 1 and respectively occur for $t = 0$ and $t = t_b$. The sensitivity curve depends on the evolution of the damping function and exponentially decays with respect to time. This suggests that $\zeta(t)$ with slow transitions from positive to negative values must be preferred to increase the area under the sensitivity curve improving the responsiveness of the SRR to the input signal.
Let us consider having a sinusoidal input signal with modulus V and phase ϕ that is delimited by the so-called *Normalized pulse envelope* $p_c(t)$

$$v(t) = Vp_c(t)cos(\omega + \phi). \tag{A.28}$$

It is shown in [105] that the output response due to $v(t)$ is approximately equal to

$$v_o(t) \approx VK_0K_s\zeta_0\omega p(t) \int_{t_a}^{t} p_c(\tau)s(\tau)cos[(\omega - \omega_0)\tau + \omega_0 t + \phi], \tag{A.29}$$

under the assumption that the frequency of the incoming signal ω is much higher than the variation of the normalized envelopes. When the carrier frequency of the input signal is equal to the resonance frequency ($\omega = \omega_0$), (A.29) can be written as

$$v_o(t) = VK_0K_s\zeta_0\omega_0 p(t) \left[\int_{t_a}^{t_b} p_c(\tau)s(\tau)d\tau\right] cos(\omega_0 t + \phi). \tag{A.30}$$

It is convenient to define the *Regenerative gain* as

$$K_r = \zeta_0\omega_0 \int_{t_a}^{t_b} p_c(\tau)s(\tau)d\tau \tag{A.31}$$

Using (A.31), (A.30) can be rearranged as

$$v_o(t) = VK_0K_rK_s p(t)cos(\omega_0 t + \phi). \tag{A.32}$$

The overall gain of the receiver K is given by the product of each single gain

$$K = K_0K_rK_s. \tag{A.33}$$

A.2 Frequency domain analysis

Let us consider the response to an input with arbitrary frequency

$$v_o(t) = VKp(t)\frac{\omega}{\omega_0}\frac{\int_{t_a}^{t_b} p_c(\tau)s(\tau)cos[(\omega - \omega_0)\tau + \omega_0 t + \phi]d\tau}{\int_{t_a}^{t_b} p_c(\tau)s(\tau)d\tau} \tag{A.34}$$

Using the Euler's form of the cosine we can rewrite (A.34) as

$$v_o(t) = VKp(t)\frac{\omega}{\omega_0}\frac{\int_{t_a}^{t_b} p_c(\tau)s(\tau)e^{j(w-\omega_0)\tau}d\tau e^{j(\omega_0 t+\phi)}}{\int_{t_a}^{t_b} p_c(\tau)s(\tau)d\tau} \tag{A.35}$$

Assuming that $p_c(t)$ and $s(t)$ are equal to zero out of the considered interval $[t_a; t_b]$, we can define the complex function

$$\psi(\omega) = \int_{-\infty}^{\infty} p_c(t)s(t)e^{j\omega t}dt = \left[\int_{-\infty}^{\infty} p_c(t)s(t)e^{-j\omega t}dt\right]^* = \mathscr{F}^* \{p_c(t)s(t)\} \tag{A.36}$$

Using A.36, we can rewrite the output response as

$$v_o(t) = VKp(t)\frac{\omega}{\omega_0}\frac{\psi(\omega-\omega_0)}{\psi(0)}cos[\omega_0 t + \phi + \angle\psi(\omega-\omega_0)] \tag{A.37}$$

and define the frequency response of Super-Regenerative systems as

$$H(\omega) = \frac{\omega}{\omega_0}\frac{\psi(\omega-\omega_0)}{\psi(0)} \tag{A.38}$$

Thus, we can write the SRR output as

$$v_o(t) = VKp(t)|H(\omega)|cos[\omega_0 t + \phi + \angle H(\omega)] \tag{A.39}$$

Note that the frequency response of the Super-Regenerative output is a band-pass filter centered at the resonance frequency ω_0 whose output linearly depends on the amplitude of the input signal. This analysis is valid as far as the oscillations are small enough to keep the feedback amplifier in linear region. When oscillation increases over an amplitude threshold depending on the characheristics of the feedback amplifier, the gain $A(t)$ reduces changing the instantaneous damping function. In this condition, the oscillation can reach saturation before $t = t_b$ when the oscillator is quenched and the output signal is damped out [105].

A.3 Noise analysis

The input noise degrades the performance of the receiver. As already stated in Section 4.1, the IBC signals propagates through an AWGN channel. Thus the input signal with additive white gaussian noise can be written as

$$v_{in} = Vp_c(t)cos(\omega + \phi) + n(t). \tag{A.40}$$

Thanks to the superposition principle we can separately study the effect of the noise and the useful signal

$$v_o(t) = v_{o,signal}(t) + v_{o,noise}(t). \tag{A.41}$$

Recalling the (A.27) it is possible to write the noise contribution to the output response of the SRR as

$$v_{o,noise}(t) = 2\zeta_0 K_0 K_s p(t) \int \dot{n}(\tau)s(\tau)sin[\omega_0(t-\tau)]d\tau. \tag{A.42}$$

Since we are interested in noise contribution around the resonance frequency ω_0, we can approximate the derivative of the noise as [106]

$$\dot{n}(t) \approx \omega_0 n(t) \tag{A.43}$$

Substituting (A.43) in (A.42) we find

$$v_{o,noise}(t) = 2\zeta_0 K_0 K_s p(t)\omega_0 \int n(\tau)s(\tau)sin[\omega_0(t-\tau)]d\tau. \tag{A.44}$$

Recalling signal theory, we can express the energy of a signal as its auto-correlation in the origin. Thus, we can use (A.44) to calculate the energy of the output noise as

$$\mathscr{E}\{v_{o,noise}(t)\} = (2\zeta_0 K_0 K_s p(t)\omega_0)^2 \int_{-\infty}^{\infty}\int_{-\infty}^{\infty} \mathscr{E}\{n(t)\}s(\tau)s^*(\tau')sin[\omega_0(t-\tau)]sin[\omega_0(t-\tau')]d\tau d\tau'. \tag{A.45}$$

Knowing that AWGN signals have a pointwise distribution of their spectral energy, we can rewrite (A.45) as

$$\begin{aligned}\mathscr{E}\{v_{o,noise}(t)\} &= (2\zeta_0 K_0 K_s p(t)\omega_0)^2 \int_{-\infty}^{\infty}\int_{-\infty}^{\infty} \frac{N_0}{2}\delta_0(\tau-\tau')s(\tau)s^*(\tau')sin[\omega_0(t-\tau)]sin[\omega_0(t-\tau')]d\tau d\tau' \\ &= (2\zeta_0 K_0 K_s p(t)\omega_0)^2 N_0 \int_{-\infty}^{\infty} s^2(\tau)sin(\omega_0 t-\tau)d\tau \approx (\zeta_0 K_0 K_s p(t)\omega_0)^2 N_0 \int_{-\infty}^{\infty} s^2(\tau)d\tau.\end{aligned} \tag{A.46}$$

Then, we can express the output signal power over a unitary resistance as the mean square value described in (A.47)

$$V^2_{o,signalRMS}(t) = \frac{1}{2}\left(V\zeta_0 K_0 K_s p(t)\int_{-\infty}^{\infty} p_c(\tau)s(\tau)d\tau\right)^2. \tag{A.47}$$

We can finally express the SNR over a unitary resistance [106]

$$SNR = \frac{V^2_{o,signalRMS}(t)}{\mathscr{E}\{v_{o,noise}(t)\}} = \frac{V^2\left(\int_{-\infty}^{\infty} p_c(\tau)s(\tau)d\tau\right)^2}{2N_0\int_{-\infty}^{\infty} s^2(\tau)d\tau}. \tag{A.48}$$

It is convenient to represent the SNR with respect to the ratio of between the energy per bit E_b and the doubled sided noise power spectral density N_0. Knowing that

$$E_b = V^2_{in,RMS}(t) = \frac{1}{2}V^2\int_{-\infty}^{\infty} p_c^2(\tau)d\tau \tag{A.49}$$

yields to

$$SNR = \frac{E_b\left(\int_{-\infty}^{\infty} p_c(\tau)s(\tau)d\tau\right)^2}{N_0\int_{-\infty}^{\infty} p_c^2(\tau)d\tau\int_{-\infty}^{\infty} s^2(\tau)d\tau}. \tag{A.50}$$

Recalling the Cauchy-Schwartz inequality [85], we can see that the maximum value of (A.50) is $\frac{E_b}{N_0}$ that occurs when the envelope of the input signal $p(t)$ equals the sensitivity curve $s(t)$ [106]. For a practical point of view, we can apply an OOK modulated input with pulse duration that completely covers the sensitivity curve. In such a condition, we can neglect the contribution of the input envelope achieving the maximum value of the SNR. It is worth noting that the maximum value of the SNR for the SRR equals the SNR of standard OOK architectures $\frac{E_b}{N_0}$